INVESTIGATIONS OF MOLECULAR CLUSTERS AND OTHER SPECIES EMPLOYING A CLUSTER BEAM APPARATUS

A Thesis

Submitted for the Degree of

Doctor of Philosophy

By

Gargi Raina

Chemistry and Physics of Materials Unit

JAWAHARLAL NEHRU CENTRE FOR

ADVANCED SCIENTIFIC RESEARCH

(A Deemed University)

BANGALORE 560 064, INDIA

SEPTEMBER 2003

Dedicated to my parents…

Declaration

I hereby declare that the thesis **"Investigations of molecular clusters and other species employing a cluster beam apparatus"** is an authentic record of research work carried out by me under the supervision of Prof. C. N. R. Rao, FRS and Prof. G. U. Kulkarni at the Chemistry and Physics of Materials Unit, Jawaharlal Nehru for Advanced Scientific Research, Bangalore, India.

In keeping with the general practice of reporting scientific observations, due acknowledgement has been made whenever work described here has been based on the findings of other investigators. Any oversight due to error of judgement is regretted.
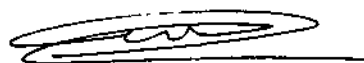
Gargi Raina

Gargi Raina

Certificate

Certified that the work described in this thesis titled "Investigations of molecular clusters and other species employing a cluster beam apparatus" has been carried out under our supervision at the Chemistry and Physics of Materials Unit, Jawaharlal Nehru Centre for Advanced Scientific Research, Bangalore, India.

Professor C. N. R. Rao

Professor G. U. Kulkarni

Acknowledgements

Preface

This thesis presents the results of the investigations of molecular clusters and other species employing a cluster beam apparatus that was indigenously built here. Chapter 1 contains a brief overview of gas-phase clusters of atoms and molecules as well as their generation and mass analysis techniques. The scope of the present investigations is presented in chapter 2.

The design and fabrication of the cluster beam apparatus attached with a time-of-flight (TOF) mass spectrometer is described in chapter 3. The mass spectrometer operates with mass resolution of ~ 800 in linear geometry (L-TOF) and ~ 2500 in the reflectron geometry (R-TOF) and is capable of detecting masses upto ~ 1000 Daltons. The cluster beam source is based on pulsed laser vaporization in conjunction with pulsed supersonic expansion method. We have been able to successfully produce carbon clusters with nuclearity of about 100. Using the liquid cell, we have been able to produce methanol clusters up to a nuclearity of 20.

Chapter 4 describes investigations of molecular clusters from alcohol-water mixtures using the cluster beam apparatus. Primary alcohols such as methanol, ethanol, n-propanol and n-butanol were chosen for this study. We explored the surface-enrichment phenomenon in the binary alcohol-water mixtures as well as ternary alcohol-alcohol-water mixtures. The effect of the alcohol chain length on surface enrichment has also been studied. We established, for the first time, that the mass spectrometric method of looking at the surface of these alcohol-water liquid mixtures provides a very accurate way of determining the surface concentration profiles. The special case of methanol is discussed in the light of its poor enriching ability. Competitive surface-enrichment in ternary alcohol-alcohol-water mixtures was also studied.

Reactivity experiments with clusters produced from solid targets using pulsed supersonic laser vaporization method were performed. Chapter 5 presents the results of reactive laser ablation of graphite in a varying atmosphere of ammonia seeded in helium. The formation of $(HCN)_m(NH_3)_nH^+$ type of clusters is reported. Molecular-orbital calculations using GAUSSIAN 98W were performed to optimize structural geometries and to determine complexation energies of these species. Chapter 6 describes the results from the reactive laser ablation experiments carried out with oxides of group 13 and 14 elements in nitrogen/ammonia seeded in helium. The oxides chosen for the study were B_2O_3, Al_2O_3, Ga_2O_3, SiO_2 and GeO_2. All oxides form nitridic or oxynitridic species in the vapor phase. The role of carbon present during the ablation was also studied.

A preliminary study of the laser ablation of metal dichalcogenides (MoS_2 and WS_2) in gas-phase in an atmosphere of jet-cooled helium as well as in solvent media such as carbon disulphide and t-butyl disulphide has been carried out. Laser ablation in a solvent medium is found to be favourable for the formation of inorganic fullerene-like structures.

***

CONTENTS

DECLARATION
CERTIFICATE
ACKNOWLEDGEMENTS
PREFACE
TABLE OF CONTENTS
LIST OF ABBREVIATIONS

List of abbreviations

Abs. Spectr.	Absorption Spectroscopy
CI	Chemical Ionization
CNMR	Carbon- Nuclear Magnetic Resonance
2C-R2PI	Two-Color Resonant Two-Photon Ionization
Dissn. & Frag.	Dissociation and fragmentation
ESI	Electrospray Ionization
EI	Electron Ionization
EXAFS	Extended X-ray Absorption Fine Structure
ESR	Electron Spin Resonance
EA	Electron Affinity
EDP	Electric Dipole Polarizability
ED	Electric Dipole
FAB-MS	Fast Atom Bombardment Mass Spectrometry
FT-ICR	Fourier Transform- Ion Cyclotron Resonance
FI	Field Ionization
GC-MS	Gas Chromotography- Mass Spectrometry
ICR-MS	Ion Cyclotron Resonance- Mass Spectrometry
IP	Ionization Potential
LDMS	Laser Desorption Mass Spectrometry
LECBD	Low-Energy Cluster Beam Deposition
Laser Spectr.	Laser Spectroscopy
MS	Mass Spectrometry
MS-MS	Tandem Mass Spectrometry
MALDI	Matrix Assisted Laser Desorption Ionization
Magn.	Magnetic measurement
NMR	Nuclear Magnetic Resonance
PI	Photoionization
PES	Photoelectron Spectroscopy
PMT	Photomultiplier Tube
QMS	Quadrupole Mass Spectrometry

REMPI	Resonance Enhanced Multiphoton Ionization
Ram. Spectr.	Raman Spectroscopy
Reactv.	Reactivity
R-TOF	Reflectron Time-of-Flight
SIMS	Secondary Ion Mass Spectrometry
STM	Scanning Tunneling Microscopy
TOF-MS	Time-of-Flight Mass Spectrometry
TEM	Transmission Electron Microscopy
u	u $\equiv$ AMU $\equiv$ Dalton
UPS	Ultraviolet Photoelectron Spectroscopy

1. Clusters of molecules, metals and other species: An overview

SUMMARY

An overview of different types of gas-phase clusters, their generation and mass detection is presented. Important design aspects of a typical molecular beam apparatus are discussed along with a historical background. Experimental studies performed on molecular clusters and elemental clusters, in particular carbon and metals are briefly reviewed. A short account on the theoretical treatment applied to clusters is presented along with some applications of cluster studies.

1.1 Historical Account

· The study of how matter behaves can be divided into two main branches. One is the reductionist approach - properties of individual atoms and molecules, namely, the field of nuclear physics and particle physics and the other being the collective approach- properties of assemblies of atoms or molecules, namely the field of condensed matter [1]. Cluster science deals with the study of matter in the intermediate regime between the bulk matter and individual atoms or molecules. The main interest of researchers in this field is to understand the evolution from atomic/molecular to bulk properties with increasing cluster size. Cluster science had its early roots in the study of colloids, aerosols and clouds. In 1949, N. F. Ramsey was the first to conduct experiments to study the magnetic properties of atoms and molecules using a molecular beam apparatus [2]. In 1956, Bentley [3] and Henkes [4] independently detected jet-generated clusters of carbon dioxide using mass spectrometers. However, the real impetus in cluster science came about in the 1970s, with the advent of lasers, modern flow reactors joined with molecular beam sources and improved mass spectrometers. In the past 20 years, lasers have taken over the place of the more conventional electron beam ionization sources. The advancement in technology i.e. pico-second and femto-second lasers in conjunction with molecular beams and time-of-flight mass spectrometry have made it possible to study molecular photoionisation and dissociation processes in greater details. A. Zewail received the Nobel Prize in 1999, for his pioneering work of combining ultra-fast laser technology with molecular beam studies to study chemical reactions at the most fundamental level, leading to the birth of a new field called, "femto-chemistry" [5]. Clusters, being isolated theoretically tractable systems, offer an opportunity to test and extend our microscopic understanding related to a variety of

fields such as amorphous solids, surface interactions, catalysis, liquid structure and solvation effects [6].

1.2 What are clusters?

Clusters are aggregates of atoms or molecules, occupying the regime between atoms/molecules— monomers and condensed phase. They differ from conventional molecules that have fixed number of atoms, specific composition and possess unique structures. Clusters, in contrast, may be composed of any number of component particles with a number of available structures that increase rapidly with the cluster size. Clusters may be classified according to their size and variation in properties, composition, charge and forces that bind them.

Table 1.1

	N	d(N) nm	$F_s(N)$
Small	$< 10^2$	≤ 1.9	≥ 0.86
Medium	$10^2 - 10^4$	1.9 – 8.6	0.86 – 0.19
Large	$> 10^6$	≥ 8.6	≤ 0.19

Cluster sizes can be classified into three different regimes. Table 1.1 above gives the approximate diameters (d) and fractions of surface atoms (F_s) for N-atom spherical sodium clusters in the different size regimes.

The property of a cluster is related to the volume and / or surface area of the cluster. For metals for instance, it is known since few decades that the atomic ionization potential (IP) is typically about twice the value of the bulk work function. In the large cluster regime, many generic cluster properties like ionization energy,

3

electron affinity, melting temperature and cohesive energy show a regular variation with cluster size (see Fig. 1.1).
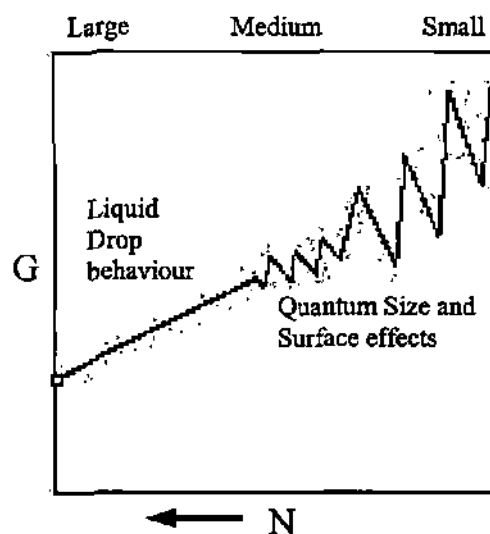
Fig. 1.1 Variation of the cluster property 'G' with cluster nuclearity, N. Large oscillations in the properties arise due to quantum size effects caused by electronic shell closings and surface effects due to geometric shell closings for small N. For large N, there is a smooth trend in cluster size effects [7].

The ionization potential shows a decreasing trend while the electron affinity shows an increasing trend as the cluster size increases [8]. The melting point of the clusters also increases as the cluster size increases. Other properties such as chemical reactivity, magnetic moment [9], polarizability [10], and geometric structure are also found to exhibit a strong dependence on N. However, for small clusters there are large oscillations about this smooth trend. These deviations arise due to the quantum size effects and the surface effects caused by filling up of electronic and geometric shells, respectively. Filled electronic shells arise due to bunching of jellium electronic energy levels while as the filled geometric shells impart stability to the cluster by maximizing the average co-ordination number Z, and thereby reducing the cluster surface energy. The size at which the transition from electronic to geometric shell structure occurs depends on many factors such as

the density of states (DOS), atomic electron configuration, melting temperature of cluster and temperature of the cluster. A cluster property is described as bulk-like when its value is within 1% of the bulk value as given by the Jortner's criterion [11].

Clusters can be classified according to the nature of the component elements or molecules and the type of binding forces holding them. The nature of the binding forces holding the clusters of elements or molecules together may be varied. They may be bound by forces that are strongly attractive as in $(NaCl)_n$, covalent– Si_n, C_n, van der Waals– Ar_n, Xe_n and hydrogen bonded as in $(H_2O)_n$, $(HF)_n$ and $(CH_3OH)_n$ [12].

In the case of metal clusters, as one reduces the size, going from bulk metal to a collection of few atoms, one would expect a dramatic change in the electronic structure leading to a metal to non-metal transition in small particles.
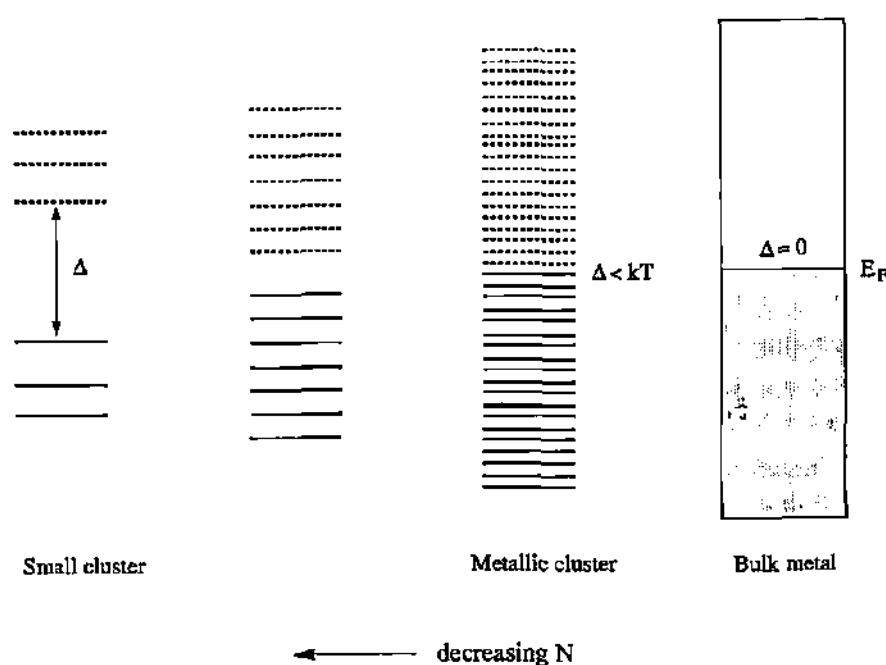
Fig. 1.2 Discretization of electronic energy levels with decreasing metallic particle size (N). Filled levels (at 0 K) are indicated by full lines and empty levels by dashed lines [7].

As the size of the metallic particle is reduced, the electronic energy levels become discrete and the spacing between the levels becomes larger (see Fig. 1.2). The condition for a finite metallic particle to exhibit metallic conduction is given by the *Kubo's criterion*

$$\Delta \approx E_F / N \leq kT \qquad (1.1)$$

where Δ is the band gap, E_F is the Fermi energy of the bulk metal. It can be seen from this equation that as cluster size decreases, the band gap increases and thus a higher temperature T will be required for metallic conduction.

1.3 Cluster beam experiments

Gas-phase clusters offer an advantage for studying the inherent properties in contrast to clusters deposited on substrates or suspended as in colloids, which may have altered properties due to substrate or solvent interactions. The basic steps involved in a cluster beam experiment are cluster generation, mass detection and spectroscopic investigations. Thus, a simple study with gas-phase clusters may deal with mass analysis extended to reactivity experiments. One can also size-select the clusters and perform spectroscopic investigations. A commonly used size-selection method involves scattering of a given cluster beam using a secondary beam of neutral rare gas atoms impinging at right angles to it [12]. It is based on the principle that the heavier the cluster, the smaller are the scattering angles and the velocity. Another method to get size-selected neutral clusters is the re-neutralization of ions i.e. the negatively charged or positively charged clusters are deflected using a magnetic or an electric field and further re-neutralized by photo-detachment (for anionic clusters) or resonant charge exchange (for cationic clusters) [13]. Yet, another possibility with gas-phase clusters is to deposit the size-selected clusters

6

onto substrates to carry out reactivity and catalysis studies on supported clusters. A critical parameter is the impact energy of the deposited clusters on the substrate, which can be adjusted by varying the acceleration voltage between the cluster source and the substrate.

1.3.1 Production of clusters

Clusters, in general, can be made by a variety of methods i.e. by vaporizing elementary component particles and letting them aggregate; by knocking them directly out of a solid and in solution as colloidal particles formed during precipitation or in submerged electric arcs. The method of production of clusters depends on the average bond energy per monomer in the cluster.

Simple methods

The Knudsen effusive cell has been one of the earliest and simplest cluster beam source to be used to produce metal dimers and in some cases larger metal clusters [14]. It is employed, primarily, to generate clusters of materials with high to medium cohesive energies, such as refractory (2-4 eV/atom) and co-valent and ionic materials (0.5-2 eV/atom). On the other hand, gas aggregation cells are used to generate clusters from intermediate to low binding energies [15]. Cluster beams generated from effusive cells generally possess low intensities and produce mostly dimers in contrast to those from gas aggregation cells, which have higher intensities of larger clusters. However, in both cases, the emerging cluster beams are not highly reproducible in nature. In this respect, supersonic expansion methods help generate reproducible cluster beams.

7

Supersonic expansion method

It is based on the principle of Joule-Thompson effect where the vapor of a material at high pressure is made to emerge through a small orifice into a low-pressure region at constant enthalpy or constant entropy (see Fig. 1.3). Since the enthalpy and entropy are conserved along each streamline, the expansion is also often referred to as "isenthalpic" or "isentropic".

Distance.		10	20	30	40	50	60
Temperature (K)	T=	4.0	1.6	0.9	0.6	0.5	0.4
Pressure (Pa)	P=	20	2	0.47	0.2	0.09	0.05
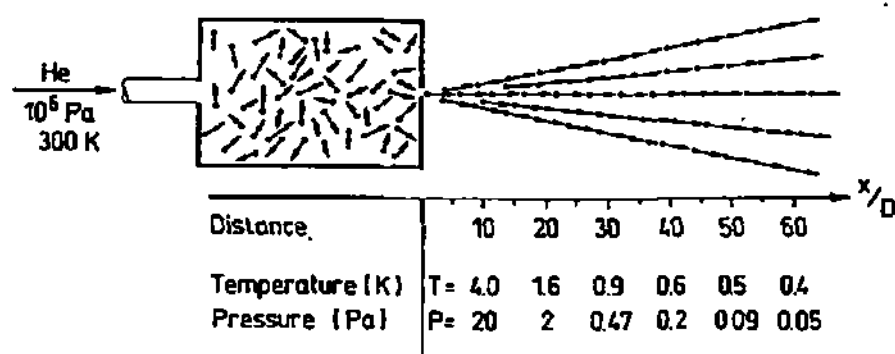
Fig. 1.3 Gas expansion through a small orifice of diameter D into vacuum. Arrows indicate velocities of atoms and molecules. Temperature and pressure at the centerline of the beam are given [12].

There are three main factors that determine the cluster content in free jets:

- Stagnation pressure

- Aperture cross-section

- Initial gas temperature

With increase in the stagnation pressure and aperture cross-section, the cluster content and average cluster size increases. Keeping stagnation pressure and initial gas temperature constant, smaller nozzle diameter produces smaller clusters with high cooling. Cluster size profile is also sensitive to the shape of the nozzles. For conical nozzles, the expansion zone is quite constrained because of which more collisions are possible and therefore larger clusters are produced. On the other hand,

sonic nozzles are not as good for cluster generation as the conical nozzles. For an axially symmetric (circular) nozzle, there is more time for clustering and therefore larger clusters are obtained in comparison to that for slit nozzle, and also the gas density and temperature fall off much less rapidly. Figure 1.4 shows the cross-section of different type of the nozzle geometries.

Sonic   Cylindrical   Conical   Laval
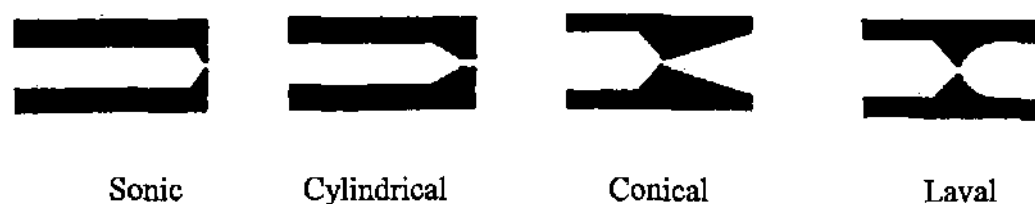
Fig 1.4 Cross sections of nozzle geometries. Conical nozzles are most effective at producing pulsed and continuous beams of large clusters [6].

Since stagnation pressure cannot be increased beyond the capacity of the vacuum pumps, the idea of pulsed expansion has emerged. Pulsed beams have higher instantaneous intensities by an order of magnitude as compared to continuous beams and also possess large cluster content. The typical opening times of pulsed nozzles are 50 µs to 1 ms. However, there are a couple of disadvantages of pulsed *system. The beam velocity, temperature and cluster distribution is not uniform* throughout the pulse. In addition, pulsed beams have low duty cycles and accordingly pulsed lasers and pulsed detection systems have to be used. Usually, a less condensable and inert gas is added to the main species, which aids in the removal of condensation energy by means of collisions with the carrier gas. Adding excess of the gas only leads to the dilution effect and does not improve the cooling any further. Depending on the type of interaction involved, in some cases the heavier the carrier gas (Ne, Ar), the larger the clusters obtained (e.g., Na_n) and in some cases the lighter the carrier gas (He), the larger the clusters, e.g., $(SF_6)_n$ [16].

1.3.2 Detection of clusters

Mass spectrometry (MS) had its beginnings about a century ago and has since become a virtually ubiquitous research tool in the study of elementary ions and cluster ions. The various scientific breakthroughs made possible by MS include the discovery of isotopes, exact determination of atomic weights, the characterization of new elements, quantitative gas analysis, stable isotope labeling, fast identification of trace pollutants and drugs, and the characterization of molecular structure. Mass spectrometry, now-a-days is providing tools that allow researchers to attempt problems previously thought invincible across a broad range of sciences, from nuclear physics to biology.

The history of MS began with Sir J. J. Thomson at the Cavendish Laboratory, University of Cambridge [17]. His studies on electrical discharges in gases led to the discovery of the electron in 1897. He constructed the first mass spectrometer then called "parabola spectrograph" for the determination of mass-to-charge ratios of ions. In this instrument, the ions were generated in discharge tubes, made to pass through electric and magnetic fields and finally detected on a fluorescent screen or photographic plate. In 1920's, Francis W. Aston, designed a mass spectrometer in which ions were dispersed by mass and focused by velocity–which improved the resolving power of the mass spectrometer by an order of magnitude. A. J. Dempster was the first to develop the magnetic deflection instrument with directional focussing in the early twentieth century. Magnetic deflection instruments, both single-focussing and double-focussing dominated high performance mass spectrometry well into the 1990's. With the improvement in ion sources and detection analyzers, a whole range of other MS techniques have evolved in parallel, such as ICR-MS, GC-MS, Quadrupole, Tandem MS (MS-MS),

SIMS, LDMS and FAB-MS etc [18]. A chronology of improvements in mass spectrometry is shown in the figure below (Fig. 1.5).
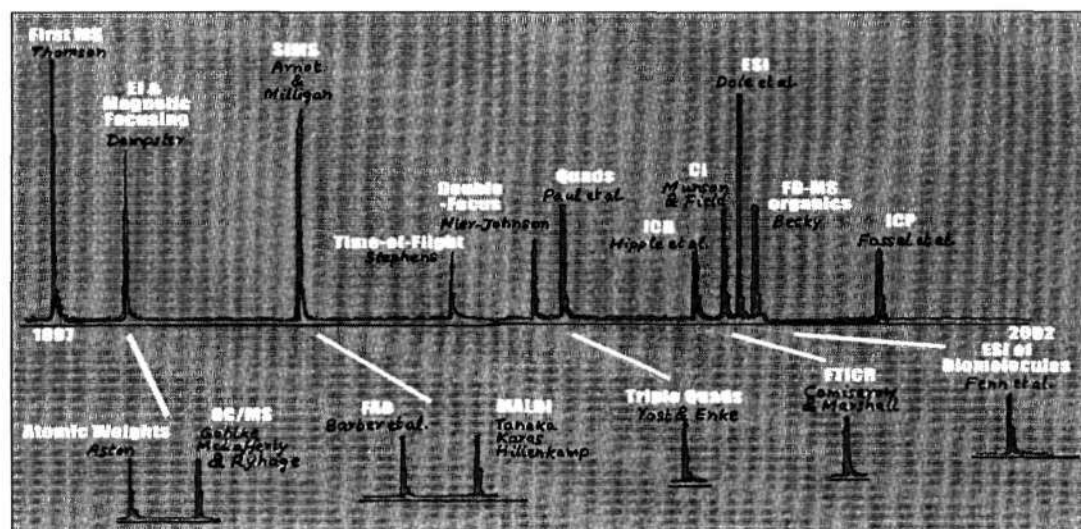
Fig. 1.5 Chronology of improvements in mass spectrometry 'A tandem view of Mass Spectrometry' [19].

Ionization techniques

The type of ionization technique employed also classifies mass spectrometry into its various kinds [19]. One of the main criteria in choosing the type of ionization technique employed is the thermolability of the sample. For samples that are not thermolabile and relatively volatile, ionization such as electron impact (EI) and/or chemical ionization (CI) can be effectively used. In electron impact ionization, which is one of the earliest ionization techniques used, ions are formed when a beam of electrons (70 eV) hits the sample molecules in the gas phase. However, this technique causes substantial fragmentation owing to the excess energy from the ionization process. Chemical ionization, which is a rather soft ionization technique, came about in the mid-1960's, employs a reagent gas to gently transfer protons to the sample. Field ionization (FI) technique is used for volatile compounds in which a high electric field gradient is applied at the tips of carbon whiskers on a tungsten emitter wire to ionize the species by tunneling of electrons.

11

Thus, FI technique produces less fragmentation. Fast ion bombardment technique utilizes a high energy (8kV) beam of neutral Xe atoms impinging on metal target holding a liquid matrix of the sample. It is best suited for polar and high molecular weight compounds such as peptides and other biomolecules. Field desorption is yet another ionization technique where the samples are loaded directly on the wire by dipping into a solution of the sample. MALDI (Matrix assisted laser desorption ionization) is one of the more popular techniques of recent times (since 1988) used for peptides, proteins and polymers. It involves embedding analytes in a matrix, which absorb energy at the wavelength of the laser. Electrospray ionization (ESI) is useful when the sample amounts are small as in biological studies. In the ESI technique, the sample solution is sprayed from a small tube into a strong electric field in the presence of a flow of warm nitrogen. The droplets formed evaporate in a region maintained at a vacuum of several torrs causing the charge to increase on the droplets. J. B. Fenn, K. Tanaka and K. Wüthrich received the Nobel prize in Chemistry in 2002 for their contributions in field of mass spectrometry techniques by combining ESI and soft laser desorption to embrace the biological macromolecules.

Time-of-flight Mass Spectrometry (TOF-MS)

Some of the commonly employed mass spectrometric techniques are QMS and FT-ICR mass spectrometry having mass ranges of ~ 4000 u and $\sim 60 \times 10^3$ u, respectively. Over the past decade, however, the upper mass limit has been pushed to more than $1,000 \times 10^3$ u and the resolving power to $\sim 1,000,000$ with the highest mass sensitivity of 10^{-22} mol. In this context, time-of-flight mass spectrometry has become a popular choice.

TOF-MS is widely used in the mass analysis of clusters produced in molecular beam experiments. It is based on the principle of segregating cluster ions that are simultaneously accelerated out of an ion source, based on their velocities as they travel through a field-free region towards a detector. Ideally, all the cluster ions should start from the same point and have the same kinetic energy. However in reality, they possess a spread in their initial positions as well as in their velocities. The best known and most often used design of the time-of-flight mass spectrometer is due to Wiley-McLaren [20], which consists of a two-stage ionization-acceleration volume that focuses the ionized particles on to a detector at the end of a field-free drift region and has a mass resolution of several hundreds. The mass resolution of the TOF mass spectrometer can be enhanced by reducing effects of spread in velocities of the ions by introducing a retarding electrostatic mirror (reflectron scheme), as was first proposed by Mamyrin [21]. This improved the mass resolution by one or two orders of magnitude. Figure 1.6 shows a typical time-of-flight mass spectrometer attached with a cluster condensation cell used by T. P. Martin's group [22].
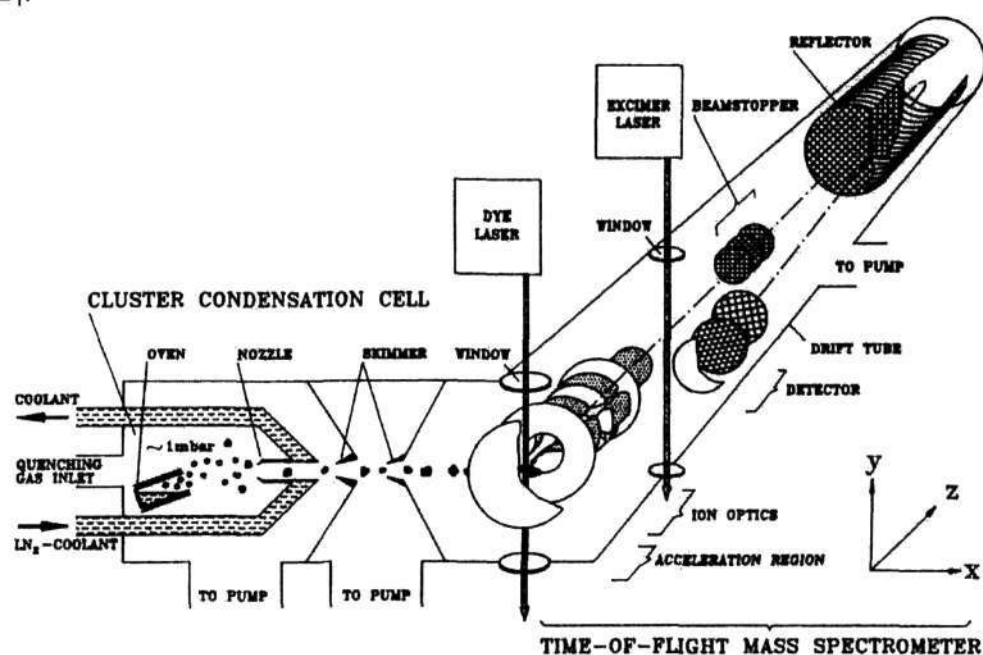
Fig. 1.6 Typical apparatus for the production, photoionization and time-of-flight mass analysis of clusters [22].

There are several advantages with time-of-flight mass spectrometers. The design of the TOF-MS is rather straight-forward and mechanically easy to construct. Theoretically speaking, TOF-MS has no upper limit for mass range, as the acceleration of the ions is purely dependent on the applied voltages. Other advantages include high ion transmission and data collection in a few microseconds. Such features make TOF-MS just suitable for laser photoionization experiments, where low repetition rate lasers are employed. They are also ideal detection systems in experiments related to reaction dynamics of jet-cooled molecules and clusters [23].

A number of other techniques complementing the TOF-MS are employed in the investigation of molecular clusters, which exhibit extensive fragmentation. Reflectron-TOF MS is often used to discern between fragmented cluster ions and unfragmented cluster ions having identical masses. Infrared spectroscopy experiments are used to get high-resolution rotationally resolved spectrum for molecular clusters. Two-color resonant two-photon ionization (2C-R2PI) is a technique in which a tunable laser is used to first electronically excite the molecular cluster resonantly and then another laser for the ionization of the cluster. This gives size-specific information for clusters containing aromatic molecules. In yet another technique known as 'Molecular beam depletion spectroscopy', the size-selected clusters are scanned as a function of the frequency of an IR laser and the decrease in the mass spectrum intensity is monitored. This provides sensitive measurement of the dissociation of the weakly bound species. Resonance enhanced multiphoton ionization (REMPI) is also often used to study the effect of clustering on the ionization of molecular clusters attached to an aromatic molecule.

1.4 Classification of Clusters

Clusters are formed by virtually all elements in the periodic table, including the rare gases. They can be classified according to the nature of the constituent atoms or molecules and the type of bonding forces that hold them together. Although, there is considerable research being conducted world-wide on a variety of clusters, the emphasis in this laboratory is mainly on the molecular clusters and carbon containing clusters.

1.4.1 Molecular clusters

Molecular clusters are clusters of neutral molecules held by weak interactions, either H-bonded or van der Waals in nature. Typical examples of van der Waals type clusters are $(CO_2)_n$, $(SF_6)_n$ and $(C_6H_6)_n$ having binding energies of ~ 100 meV or less [24]. Other examples are Aniline-$(Ar)_n$, Tetracene-$(Ar)_n$, Anthracene-$(Ar)_n$, (Pyrozole-Ar), (Thiophene-Ar), which have general form (M-Rg_n) where 'M' is an aromatic molecule and 'Rg' the rare–gas atoms. The characteristic feature of these complexes is the existence of several isomers for a given 'n', where each of them can be identified by their slightly different absorption frequency. Such studies reveal the anisotropy of the intermolecular potential of the complex.

The other important class of molecular clusters is the H-bonded clusters. Typically, H-bonded clusters such as $(HF)_n$, $(H_2O)_n$ and $(CH_3OH)_n$ have binding energies smaller than 300 meV [25]. Water being one of the most important and common solvents is of particular interest towards the understanding of solute-solvent interactions. Many studies have also been carried out on hydrogen-bonded ammonia and alcohol clusters. REMPI is used to study the influence of clustering

15

on the ionization of these H-bonded clusters. Few representative systems studied under this category are anthracene$(H_2O)_n$, perylene$(H_2O)_n$ and benzene$(H_2O)_n$. The aromatic molecule acts like a chromophore, allowing the spectroscopic investigations of the electronic ground and excited state of the neutral molecules and the ion. The shift in the peaks gives information about the structure while the broadening of the peaks is related to the decay dynamics.

The investigation of structural and dynamical properties of molecular clusters has attracted a great deal of interest in recent years [26,27]. Molecular clusters are interesting to study as model systems for solvation, where the solvent effects on the electronically and vibrationally excited states of a particular solute can be investigated as a function of the nature and number of solvent molecules in the cluster. Due to the finite size of these clusters, theory is also able to contribute quantitative results that can often be compared directly with those from experiment. Thus, considerable progress is being made in understanding the nature of the intermolecular interactions, the structural motifs and the dynamics of many complexes.

Alcohol and water clusters, in particular, have been studied extensively in terms of their structural properties and vibrational spectra. Infrared spectroscopic measurements revealed that protonated water clusters consist of a number of water molecules surrounding a hydronium ion, H_3O^+. The well-known $(H_2O)_{21}H^+$ cluster produced in free jet expansion is a magic nuclearity cluster, having a clathrate-like pentagonal dodecahedron structure of 20 water molecules with the hydronium ion at the center (see Fig. 1.7).
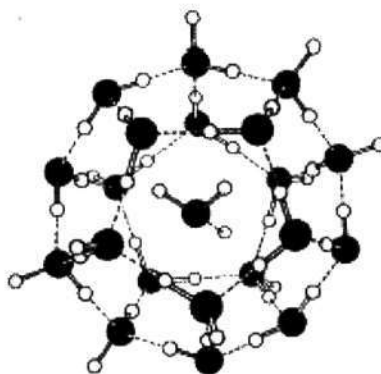
Fig. 1.7 Structure of $(H_2O)_{21}H^+$ cluster showing encagement of H_3O^+ within the pentagonal dodecahedral hydrogen-bonded structure of $(H_2O)_{20}$ [28].

There have been many vibrational studies devoted to the investigation of the intramolecular modes in water clusters. For instance, water monomer has three fundamental vibrations: the bending mode (v_2) near 1595 cm^{-1}, the symmetric OH stretch (v_1) at 3657.05 cm^{-1}, and the asymmetric OH stretch (v_3) at 3755.97 cm^{-1}. The O-H stretching bands of the charged H_3O^+ core have slightly lower frequencies than the neutral water molecule. Upon solvation, some of the stretching bands are strongly red-shifted in the case of small clusters and blue-shifted in the case of large clusters. Electron diffraction measurements performed on neutral water clusters $(H_2O)_n$ in the range, n = 1500-2000 have shown that these clusters possess a low-pressure cubic phase of bulk ice, while smaller clusters, n $\leq$ 300, have a disordered amorphous structure.

In contrast to water, which forms tetrahedral networks, methanol can only interact via a linear hydrogen bond besides the hydrophobic forces around the methyl group. Consequently, it forms only extended chains or rings. Size-selected methanol clusters have been investigated in detail by the scattering method for their OH and CO stretching modes. Structural information on water and methanol clusters has been obtained from molecular beam electric deflection studies [29].

Molecular beam deflection experiments revealed that both the monomers and dimers of water and methanol are polar in nature, which is consistent with the presence of a linear hydrogen bond [30]. In both cases, higher nuclearity clusters with n=3 to 6 are nonpolar in character suggesting that the larger complexes have cyclic structures. Larger clusters of water, n=7 to 10, exhibit 3-dimensional cage structures while those of methanol form rings (see Figure 1.8).
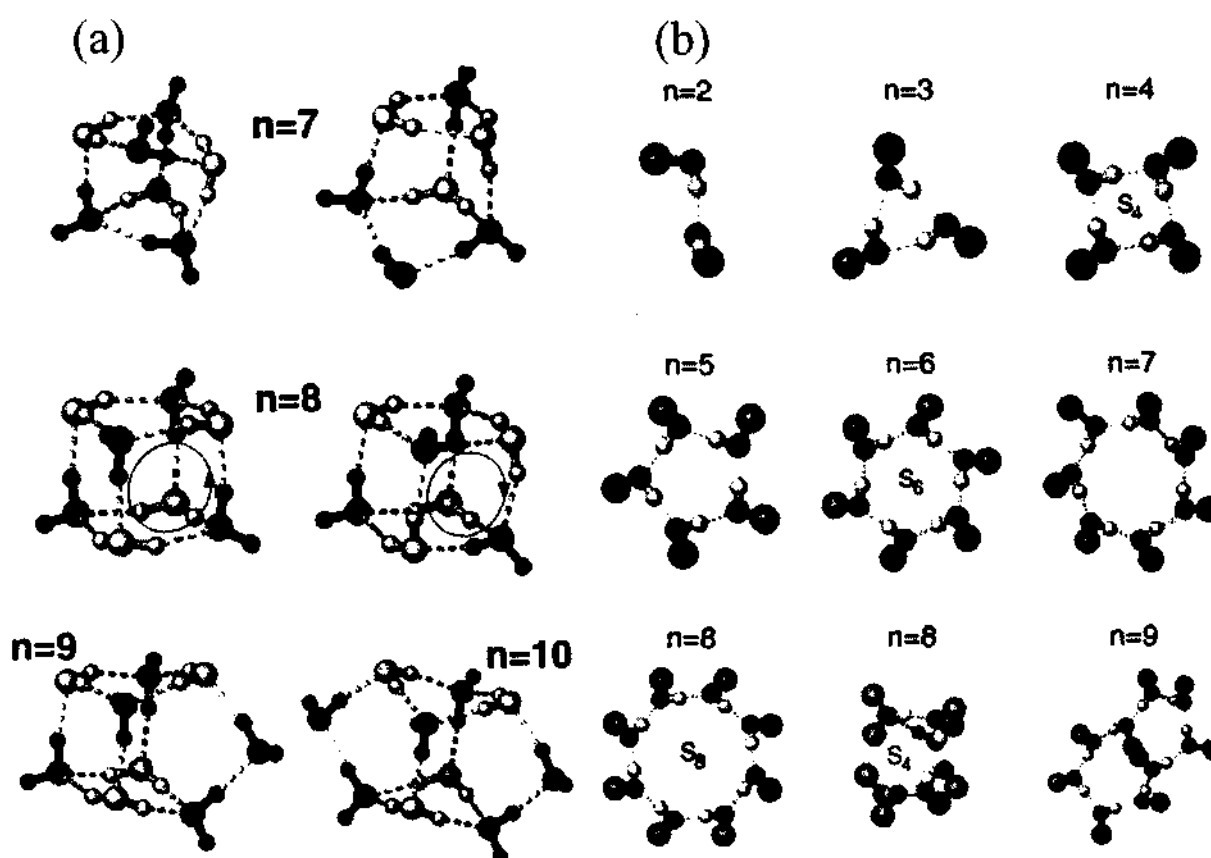
Fig. 1.8 Calculated minimum energy configurations (a) Water clusters (heptamer to decamer), (b) Methanol Clusters (dimer to nonamer) [31].

Mixed gas-phase clusters of the type $(ROH)_n(H_2O)_mH^+$ have been investigated from the point of view of preferential solvation of the hydrogen ion by either water or alcohol molecules [32]. Thermochemistry studies performed on mixed water-methanol cationic species indicated that the favored topology places the methanol molecules near the charged centers and water molecules at the

periphery [33]. The influence of solvation on dehydration reaction for alcohol clusters has been investigated using the reflectron technique by Castleman et al., who proposed that protonated methanol peaks arise from a rapid intracluster proton-transfer reaction following ionization of neutral clusters [34].

$$(CH_3OH)_n^+ \rightarrow H^+(CH_3OH)_{n-1} + CH_3O$$
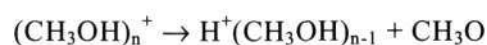
Infrared spectroscopy studies performed on mixed clusters of methanol and water have shown that the methanol molecule is engaged as a proton donor and an acceptor in a ring structure containing two, three, or perhaps four water molecules [30]. A number of solvated ions of the type $M^+(H_2O)_n$ (M= alkali metal) and X^- $(H_2O)_n$ (X= halide) have also been studied and the solvation energies of the cations and the anions in the solvent molecule clusters have been measured [35].

1.4.2 Elemental Clusters

Carbon clusters, Endohedral fullerenes and Met-cars

Carbon nucleates to form clusters much more readily than any other element in the periodic table. Technological and astrophysical applications make their study interesting and an exciting field of cluster research. The work on carbon clusters led to the discovery of fullerenes (C_n with $n \geq 24$), by Kroto and Smalley [36], which has become a vast field by itself. C_{60}, the third allotropic form of carbon with the famous truncated icosahedron structure (Figure 1.9), has gathered interest because it can be easily produced in macroscopic quantities.

Fig. 1.9 C_{60} molecule is polygon with 60 vertices and 32 faces, 12 of which are pentagonal and 20 hexagonal, having a truncated icosahedron structure [36].

A number of characterization studies such as ionization potential, electron affinity, electronic structure, NMR and photofragmentation have been performed on fullerenes [37]. Small carbon clusters have also been studied extensively. Investigations of photofragmentation studies of small carbon clusters revealed that loss of a C_3 unit is the dominant fragmentation pathway [38]. Electron affinity measurements have been performed using UV photoelectron spectroscopy of negative carbon cluster ions to throw light on the relative stabilities and transformation from chain to ring structures [39]. Some reactivity studies of mass selected C_n^+ clusters (n<20) with diatomic molecules, small hydrocarbons and HCN have also been carried out [40].

Endohedral fullerenes

Possibilities of endohedral chemistry with the cage of C_{60} have been explored extensively. Metallofullerenes are a set of compounds in which a metal is encaged inside a fullerene. Few metallofullerenes have C_{60} as the cage because of its small size although, higher fullerenes such as C_{82} and C_{84} are more frequently used. Metal atoms that successfully form the endohedral metallofullerenes are those that do not form strong metal-carbide bonds under the synthesis conditions (1000 to 5000 °C). Only a handful of rare-earth elements such as La, Y, Sc, Ce and Pr form stable endohedral compounds and also some of the noble gases. An example of the time-of-flight mass spectrum of rare-earth element inside fullerenes (La@C_{60}, La@C_{82}) is shown in Figure 1.10.

Various spectroscopic and structural analyses including UPS, TEM, EXAFS, STM, ESR, CNMR and X-ray diffraction have been performed to elucidate novel molecular and solid-state properties of these endohedral fullerenes.
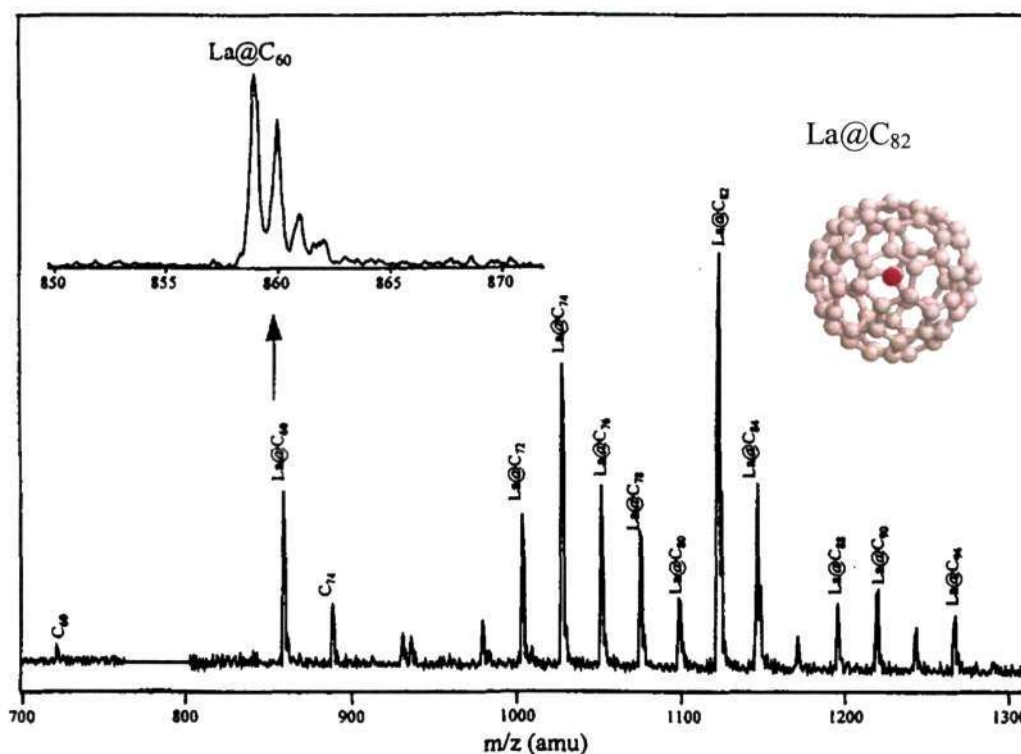
Fig. 1.10 Positive ion TOF mass spectrum of lanthanum/graphite target. Inset shows the structure of La@C_{82} with lanthanum inside the cage [41].

Rare gas atoms can also be inserted inside the fullerene cages. Such endohedral fullerenes form during the arc vaporization of graphite in presence of the noble gas. Thus, rare gas atoms He, Ne and Ar as well as D and D_2 [42] have been inserted inside fullerene cages.

Met-Cars

The discovery of new class of molecular clusters called "met-cars" containing metal and carbon atoms was made in 1992 by Castleman et al. [43]. They were discovered during the dehydrogenation reactions of small hydrocarbons with transition metal ions, atoms, and clusters. The first met-car to be discovered was $Ti_8C_{12}^+$ with a pentagonal dodecahedron structure and T_h symmetry. The structure consists of eight Ti atoms in a cubic arrangement with six C_2 units capping each square face (Figure 1.11).

21
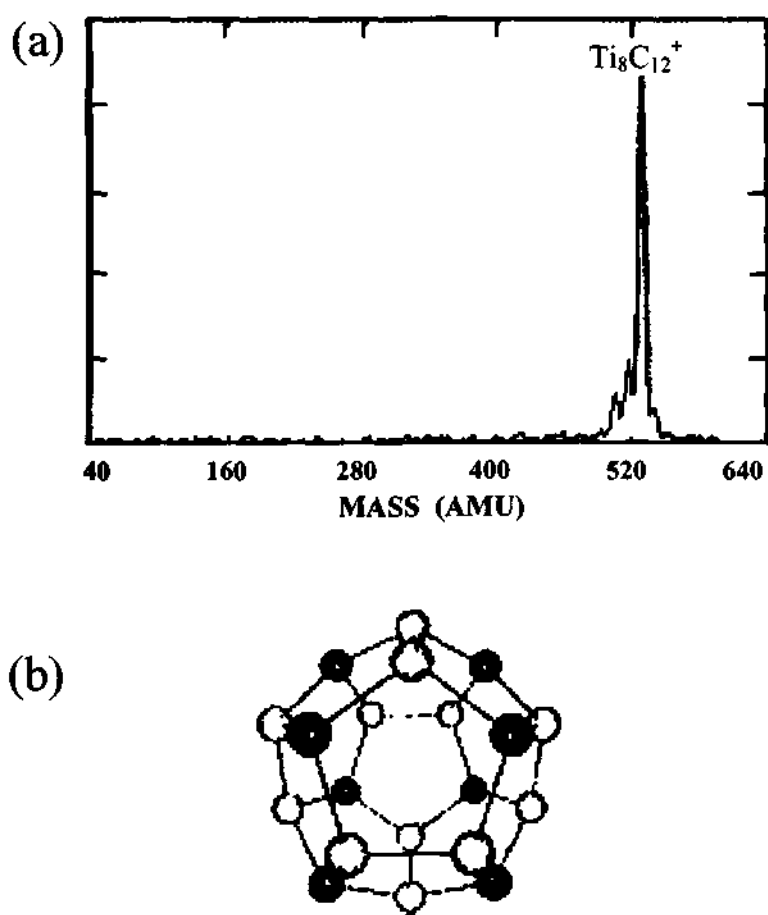
Fig. 1.11 (a) Mass distribution of $Ti_mC_n^+$ clusters generated from the reactions of titanium with CH_4. A 'super magic' peak corresponding to $Ti_8C_{12}^+$ (b) $Ti_8C_{12}^+$ has the observed stability on account of its idealized pentagonal dodecahedron structure, T_h point group. The eight titanium atoms (dark spheres) appear at the edge of a cube-like arrangement and are similarly co-ordinated to three carbon atoms (light spheres) at all equivalent positions [43].

22

Other M_8C_{12} cluster compounds including those with V, Cr, Fe, Nb, Zr, Mo and Hf have also been reported [44,45]. In contrast to the typical structure of Ti_8C_{12} met-car, the Zr-C and Nb-C complexes develop into multicage network such as double, triple and quadruple cages.

Other elemental clusters

Elements are easily classified as metallic, nonmetallic or semiconducting purely in terms of their atomic ionization potentials [46]. For instance, the ionization potentials for rare gas atoms are quite large and those for the alkali atoms are low. Clusters of alkali metals show magic nuclearity for clusters containing 2, 8, 20, 40, ... atoms, corresponding to closed electronic shells. These clusters are also characterized by large ionization potentials and the addition of one more atom marks a drop in their ionization potential, thus showing a similar trend as seen in the electronic ionization potential of an individual atom. Hence, one could expect that atomic clusters should mimic the chemistry of the atoms. Alkali metals are considered as prototypes of metals because of the freely mobile electrons. Similarly, alkali clusters (s^1 clusters) are considered to be prototypes of metal clusters. Among them, much attention has been devoted to Na, K [47,48] and Li [49]. Few experiments have been done with mixed Na_xK_y clusters as well [50].

The shell structure is more pronounced for silver, than for sodium and potassium due to deeper potential well for silver than for sodium and potassium. Metal clusters from group IIIB (B, Al, Ga, In) have also been studied and particularly Al clusters which have been widely studied in terms of photoionisation, polarizabilities and magnetic properties [51,52]. Transition elements containing partly filled d or f shells find important application from the point of view of

catalysts and hence there is great motivation to study the chemical properties of these clusters. Mass spectra of transition metal clusters do not show magic numbers that can be accounted by the electronic shell model. A characteristic of transition metal chemistry is that they can adopt several oxidation states. Only Cu, Ag and Au which have $(n+1)s^1nd^{10}$ electronic configuration, show mass spectra of clusters which follow the shell closings. Chemical reactivity also reflects the relative cluster stability. Ionization energies of Ni_n, Fe_n, Co_n and Nb_n were measured by Knickelbein [53] and all of them have the same general trend for the ionization energies. There are large variations in ionization energies for smaller clusters and the variations diminish with increasing size. Knudsen cell mass spectrometry has been used to measure dissociation energies for nearly all transition metals [54]. Magnetic clusters provide a link between magnetism on the microscopic atomic level and the macroscopic state, thereby allowing us to observe magnetic order as it develops from individual magnetic atoms to large crystals. These clusters can contribute to our understanding of magnetism in both regimes. The periodic table shown in Fig. 1.12, provides a bird's eye view of the various elemental clusters that have already been reported and the method employed to make them as well as the properties studied.

1.4.3 Other novel clusters

Current research into semiconductor clusters is focused on the properties of "quantum dots"—fragments of semiconductors consisting of hundreds to thousands of atoms. Quantum dots exhibit strongly size-dependent optical and electrical properties. A number of studies have been performed on the properties of III-V clusters as well as Ga and In clusters [102,103].

24

Fig. 1.12 Periodic table showing clusters formed by various elements employing different methods. Properties measured for them are denoted alongside with the references. (For full names, see index).

Semiconductor-based

Developing new nanocrystal materials based on III-V compounds is important because based on bulk material characteristics, these materials exhibit more pronounced quantum confinement effects compared to II-VI compounds or other more ionic systems. The primary reason behind this is on account of effective mass approximation that describes the extent to which carriers are delocalized over a lattice and the effect of confining those carriers to an unusually small volume. For example, for InAs an exciton delocalizes over 680 Å, while in InP the bulk exciton diameter is 150 Å and in CdSe it is only 70 Å. Also, the development of III-V nanocrystals will allow many interesting comparisons with other types of quantum confined structures such as quantum wells, wires, and larger dots as these systems are most highly developed in III-V materials [104]. Using laser vaporization in conjunction with supersonic beams, there have been a few studies carried out on GaAs clusters like spectroscopy to measure bond-length [105], photodissociation of GaAs clusters containing upto 30 atoms to look at their fragmentation pattern (appear to dissociate by sequential loss of atoms rather than by loss of magic fragments) [106]. Similarly photodissociation studies have also been carried out on small InP clusters [107, 108]. However, solution-phase colloidal syntheses have been more popular in the preparation of the above III-V semiconductor nanocrystals. Many of the quantum confinement effects of nanocrystals are evidenced in the optical properties of the system as the electronic energy levels of the clusters become a function of size. Towards this end, absorption spectroscopy and transient hole burning spectroscopy is employed to study the absorption and emission properties.

Nanoassembled model catalysts

Nanoassembled model catalyst is a term employed for ultra-small, size-selected clusters deposited on well-characterized oxide surfaces. The experiments involving such catalysts show dramatic changes in the size-dependent evolution of the efficiency and selectivity of catalytic processes, for example, the polymerization of acetylene on small Pd_n clusters [109] or the oxidation of CO on small Au_n, Pt_n, Pd_n and Rh_n clusters [110]. There are several major differences in the studies performed using such "model catalysts" in comparison with the conventional catalysis studies carried out so far.

In the case of conventional catalysis, the active metal particles are composed of 100's or 1000's of atoms and the electronic states are well described by electronic bands. Accordingly, the intrinsic bulk properties of a given 'catalyst' element do not change as a function of the precise particle size. Thus, the observed structure sensitivities arise mainly due to surface morphologies such as densities of kinks, steps as well as the types of crystal facets of the surface on which the particles are deposited.
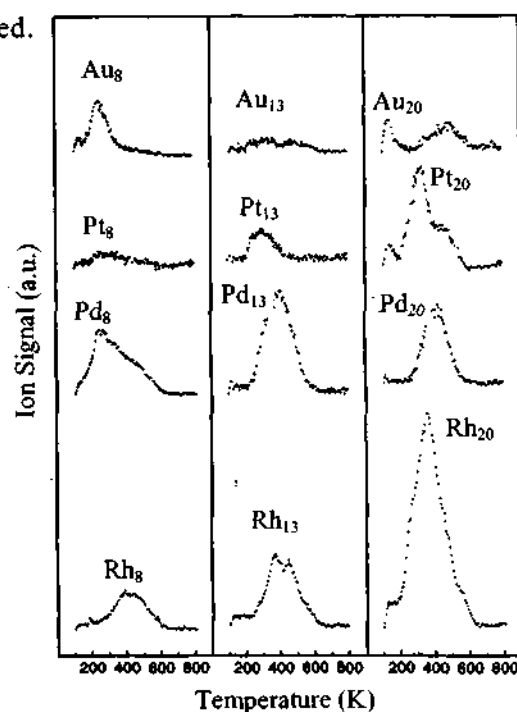
Fig. 1.13 CO combustion on Au_n, Pt_n, Pd_n and Rh_n (n= 8, 13, 20) clusters. Each cluster shows a different reactivity and reaction temperature [110].

27

However for small clusters (nano-scale clusters), these simple concepts do not hold. For the nano-scale clusters, the valence electrons are highly confined and therefore, the quantum size effects dominate. Hence, new concepts are developed to classify the size- dependent catalytic properties of nano-scale clusters. Examples of studies performed in the above light are experiments carried out to a) study size-dependency for the CO-oxidation within an element (for e.g. Au_8, Au_{13} and Au_{20}) b) different reactivities of a single cluster size (for e.g. Au_{13}, Pt_{13}, Pd_{13} and Rh_{13}) (see Fig. 1.13).

1.5 Reactivity experiments with gas-phase clusters

Different types of reactivity experiments have been carried out with gas-phase clusters. They can be broadly classified into three types (see Fig. 1.14)

* Co-expansion of metal plume and reactant gas

* Fast-flow reactors

* Pick-up source

In a typical co-expansion type of experiment, the metal vapor emerging from the laser irradiated surface of the metal rod is mixed in the reaction zone with the supersonic expansion of a reactant gas seeded in a carrier gas. This method has been employed in the formation of metal-carbides, metal-nitrides, metal-silicide, metal-sulphide or metal-oxide clusters. Various transition metal carbides "M_nC_m" (M= Ti, V, Sc, Y, La) have been made employing this route. Pure elemental clusters such as C_n and Si_n have been made, similarly, by dehydrogenation of gaseous hydrogen containing molecules (C_2H_4 and SiH_4) over a transition metal rod subjected to intense radiation of a pulsed laser [111]. The selected reactant gas is often mixed in
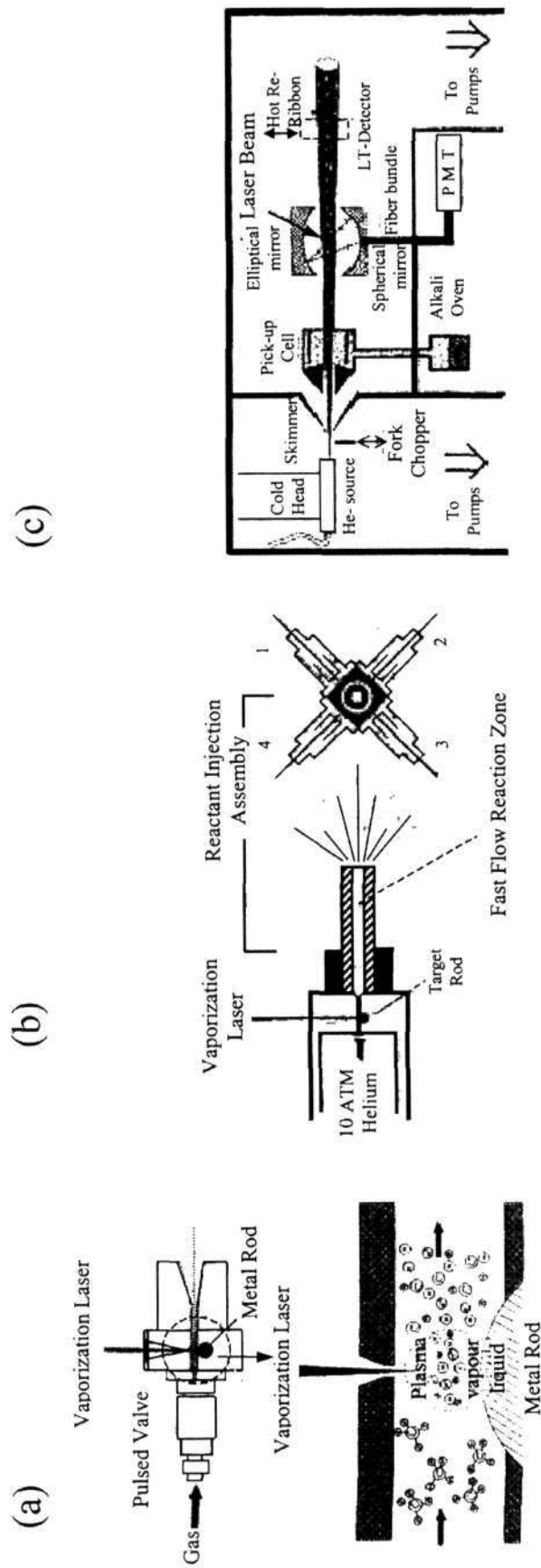
Fig. 1.14 Schematic of different experimental set-ups used for reactivity experiments with gas-phase clusters: (a) Laser induced plasma source involving co-expansion of reactant gas with carrier gas and the metal plume [111] (b) Fast-flow metal reactor comprising of metal cluster source and reaction tube assembly [112] (c) Pick-up cell for doping inert gas clusters with alkali metals [114]

29

a gas handling system with mass flow controllers. Figure 1.14a shows the schematic of the co-expansion set-up.

Another set-up for reactivity of gas-phase clusters is achieved using "flow reactors". In this method, the metal target is mounted in the throat of supersonic nozzle. A reaction tube is placed further down from the expansion cell into which *the reactants are injected. The reactants can be injected via hypodermic needles* placed around the periphery of the reaction tube, which in turn are each connected to independent pulsed reactant nozzles that can be triggered separately, as shown in the Fig. 1.14b [112]. Several parameters can be controlled here viz. the reaction time (defined by the channel length), time of firing and pulse width of reactant gas pulse. Another variation of flow reactor set-up is one in which the metal ions are produced by thermionic emission and the reactant molecules are introduced via a reactant inlet placed at different locations in the flow tube [113].

The third type of experimental set-up to perform reactivity experiments with free gas-phase clusters is called the 'pick-up' source. In this method, inert gas such as He is expanded from a very high stagnation pressure 10^4 kPa, through a tiny nozzle diameter to low temperature (12 K). In this process very large helium clusters are formed (droplets ~ 10^4 atoms/clusters). These He droplets are doped by alkali vapor using a heated pick-up cell, which is in turn connected to an alkali reservoir [114]. The schematic of such a set-up is shown in Fig. 1.14c.

1.6 Theoretical treatments of clusters

Metal clusters especially alkali clusters have been subject of extensive theoretical work. Their electronic and optical properties have been understood in terms of their quantal arrangement of delocalized electrons (one per atom for alkali-

metal clusters) moving in a mean field [115]. The simplest and most widely used model to describe the delocalised electrons in metallic clusters is that of a free electron gas, otherwise known as a jellium model. In this model, the positive charge is regarded as being "smeared out" over the entire volume of the cluster while the valence electrons are free to move within this homogeneously distributed positively charged background. The jellium model works very effectively for monovalent metallic clusters like sodium and potassium. The calculated potential for the electrons in a spherical jellium approximation typically looks like the example given below (see Fig. 1.15). The electronic energy levels are grouped together to form shells.
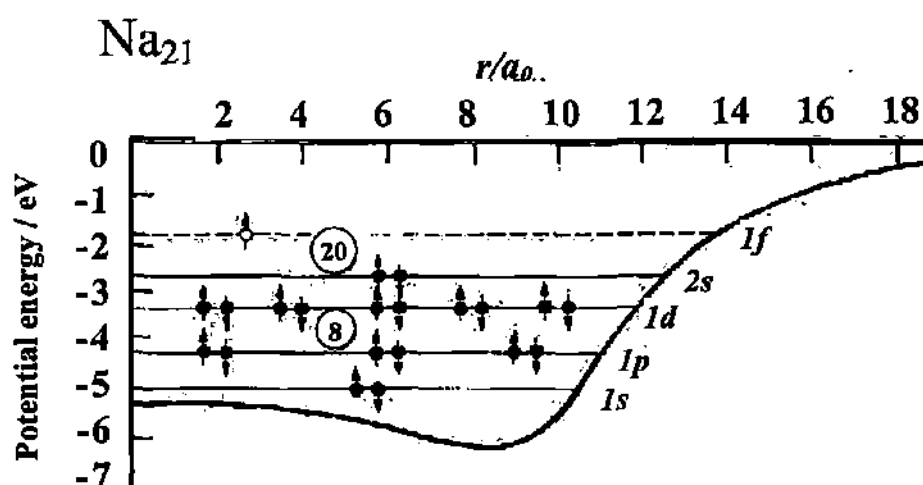
Fig. 1.15 The picture shows the electronic energy levels for a spherical cluster of 21 sodium atoms calculated using Ekardt's self-consistent electron potential. The calculated single-electron energy levels are also shown. The filled circles indicate the filled electronic shells, the empty circle shows where the 21st electron would have to go [118].

While the spherical jellium model has been able to explain general features of enhanced abundances of valence electrons in spherical clusters [116], the finer structure in the mass spectra between magic numbers has been explained via symmetry breaking mechanisms [117] similar to the situation in nuclear

structures. Despite the simplicity of the above theoretical treatment, these approaches were successful in explaining many experimental findings in cluster physics such as the ionization potentials, electron affinities and polarizabilities, besides mass-spectrometry abundance distributions.

For the weakly bound clusters (i.e., molecular clusters), force-field and molecular dynamics approaches are undertaken. The classical force field methods use empirical potentials to describe atomic interactions and predict stable structures and heats of formation from molecular dynamics calculations [119]. As these are not quantum mechanical methods, they do not yield much information about electronic structure.

As the cluster size increases and the energy states get closer, thermal fluctuations play a dynamic role to allow various structures to be seen at the time scale of experimental studies [120]. Hence, real time dynamics takes on great importance for weakly interacting molecular cluster systems where bond breaking and making are viewed on the same time scale as the electronic structure change [121]. Two commonly used methods for classical simulations are Monte Carlo and · Molecular dynamics [122]. These methods were first applied to small argon clusters to obtain structure and thermodynamics of such systems [123]. Monte carlo method has also been used to interpret vibrational spectra of large clusters of H_2O [124] and N_2O [125]. The Monte Carlo method begins by assuming a suitable potential energy surface, which generally includes both intramolecular and intermolecular interactions. A large number of cluster configurations are generated and used to estimate the equilibrium properties of the cluster. Ab initio molecular dynamics simulation was pioneered by Car and Parrinello [126]. In the molecular dynamics method, the random sampling technique is replaced by performing a numerical · solution of Newton's equation of motion. Molecular dynamics simulations sample

the configuration space by collectively moving the particles in contrast to Monte Carlo simulations. These methods offer information on the thermodynamic, structural and spectral properties of clusters.

Simulated annealing methods utilizing quantum forces are used to predict the ground state structures of clusters with upto a dozen atoms or so [127]. In this method, the cluster is heated to high temperatures typically ~ 2800 K and gradually cooled (~ 300 K). This method is often used for semiconductor clusters to describe their structural and electronic properties [128].

Along with advances in the experimental measurement techniques, there is also a constant growth on the theoretical fronts to address a wide variety of questions related to structure, dynamics and reactivity of clusters.

1.7 Applications of cluster studies

The nanoscale revolution in high surface area materials has come about for several reasons. First, in the past thirty years, there has been enormous progress in the synthesis, characterization, and basic theoretical and experimental understanding of materials with nanoscale dimensions, i.e., small particles and clusters and their very high surface-to-volume ratios. Secondly, the properties of such materials have opened a third dimension to the periodic table, that is, the number of atoms, N, which is an important parameter influencing the properties for "small" systems. Expectations for new materials with properties different from the atom or the bulk material have been realized. It is now possible to precisely tailor new materials through atom-by-atom control of the composition, controlling the types as well as the numbers of atoms, to generate clusters or particles of precision

design. The clusters, themselves, can be used as building blocks of larger-scale materials or as devices—that is, nanotechnology and fabrication at its ultimate.

Few areas where the nanostructure approach to high surface area materials has had significant impact are:

- Microporous materials for energy storage and separations technologies, including nanostructured materials for highly selective adsorption/separation processes such as H_2O, H_2S, or CO_2 removal and high capacity, low volume gas storage of H_2 and CH_4 for fuel cell applications

- Thermal barrier materials for use in high temperature engines

- Incorporation into construction industry materials for improved strength or for fault diagnostics

- Biochemical and pharmaceutical separations

- Product-specific catalysts for petrochemical processes

Recently, cluster-assembled nano-structured carbon films have been grown via low-energy cluster beam deposition (LECBD) [129] with high deposition rates. The resulting material has a low density and the characteristic length scales are determined by the cluster dimensions and their degree of fragmentation and coalescence after deposition. Such a method does not favor the formation of a hard material but leads to large porosity and surface corrugation which is beneficial for electrochemical and field-emission applications [130,131]. Endohedral fullerenes with metal atoms inside the fullerene cages find possible application to shield radioactive "tracer" atoms inside cages and then inject them into people's blood in order to watch blood flow. Doped C_{60}, for example, A_3C_{60} type compounds where A is an alkali metal such as K, Rb, Cs, Na, can be regarded as a three-dimensional organic superconductor [132]. These materials have the second-highest

superconducting transition temperatures ever observed (after the cuprates), ranging from 19 to 40 K.

Research on molecular gas-phase solvated ions finds important motivation for studying ion-molecule complexes that are governed by many of the same interactions that are at work in ion solvation in solution and thus offer a unique opportunity to gain insight into ion solvation at the microscopic level. Such cluster ions have a core ion that interacts with one or more molecules and may be of either polarity. Understanding the nature of the intermolecular interactions in these finite size clusters is the major driving force for the development of new theoretical methods to link the experimental observables with the relevant intermolecular potential surfaces. The future of this field promises such major contributions to science as a detailed molecular level description of complex fluids, including water. A continued systematic study of a diverse range of systems also holds considerable promise in the development of a more rational approach to the development of molecular force fields, thus providing a more fundamental approach to the whole field of biomolecular modeling [27].

References

[1] *'Clusters of atoms and Molecules I, Theory, Experiment, and Clusters of Atoms'* Edited by H. Haberland, Springer-Verlag: Berlin (1994).

[2] N. F. Ramsey, *Phys. Rev.* 76, 996 (1949).

[3] P. G. Bentley, *Nature* 190,432 (1961).

[4] W. Henkes, *Z. Naturforsch A* 16, 842 (1961).

[5] F. C. DeSchryver, S. D. Feyter, and G. Schweitzer, In *'Femtochemistry'* Wiley-VCH: Weinheim, Chap 1 (2001).

[6] *'Atomic and Molecular Beam methods'* *Vol I*, Edited by G. Scoles Oxford University Press: New York, 380 (1988).

[7] R. L. Johnston, *Phil. Trans. R. Soc. Lond. A* 356, 211 (1998).

[8] M. M. Kappes, *Chem. Rev.* 88, 369 (1988).

[9] D. M. Cox, D. J. Trevor, R. L. Whetten, E. A. Rohling and A. Kaldor, *Phys. Rev. B* 32, 7290 (1985).

[10] P. B. Armentrout, *Proc. SPIE* 620, 38 (1986).

[11] J. Jortner, *Z. Phys. D.* 24, 247 (1992).

[12] U. Buck, In *'Clusters of atoms and Molecules I, Theory, Experiment, and Clusters of Atoms'* Edited by H. Haberland, Springer-Verlag: Berlin, 209 (1994).

[13] U. Buck, *J. Phys. Chem.* 92, 1023 (1988).

[14] K. Hilpert *'Chemistry of inorganic vapors. Structure and Bonding'* 73, 99 (1990).

[15] K. Sattler, J. Muhibach and E. Recknagel, *Phys. Rev. Lett.* 45, 821 (1980).

[16] M. Kappes, R. Kunz, and E. Schumacher, *Chem. Phys. Lett.* 91, 413 (1982).

[17] I. Falconer, In *'Historical studies in the physical and biological sciences'* 18, 265 (1988).

[18] H. J. Svec, *Intl. J. of Mass Spectrom. and Ion Processes* 66, 3 (1985).

[19] C. M. Judson, In 'Early history of mass spectrometer ionization methods, http://masspec.scripps.edu/information/history/perspectives/judson.html.

[20] W. C. Wiley and I. H. McLaren, *Rev. Sci. Instrum.* 26, 1150 (1955).

[21] B. A. Mamyrin, V. I. Karatev, D. V. Shmikk, and V. A. Zagulin, *Sov. Phys. JETP* 37, 45 (1973).

[22] T. P. Martin, *Physics Reports* 273, 199 (1996).

[23] O. Echt, P. D. Dao, S. Morgan, and A. W. Castleman, Jr., *J. Chem. Phys.* 82, 4076 (1985).

[24] J. Jortner, In Ber Bunsenges. *Phys. Chem.* 88, 188 (1984).

[25] J. Jortner, D. Scharf and U. Landmann, In '*Elemental and Molecular Clusters*' Edited by G. Benedek, T. P. Martin and G. Pacchioni, Springer: Berlin, 148 (1988).

[26] '*The Chemical Physics of Atomic and Molecular Clusters*' Edited by G. Scoles North-Holland: Amsterdam (1990).

[27] *Chem. Phys.* 239, (complete issue) (1998).

[28] A. W. Castleman, Jr. and K. H. Bowen, Jr., *J. Phys. Chem.* 100, 12911 (1996).

[29] B. D. Kay and A. W. Castleman, Jr., *J. Phys. Chem.* 89, 4867 (1985).

[30] T. Dyke and J. Muenter, *J. Chem. Phys.* 57, 5011 (1972).

[31] U. Buck and F. Huisken, *Chem. Reviews* 100, 3863 (2000).

[32] A. J. Stace and A. K. Shukla, *J. Am. Chem. Soc.* 104, 5514 (1982).

[33] M. Meot-Ner, *J. Am. Chem. Soc.* 108, 6189 (1986).

[34] S. Wei and A. W. Castleman, Jr. *Int. J. Mass Spectrom. Ion. Processes* 131, 233 (1994).

[35] A. W. Castleman In "*Solvated Cluster ions In Clusters of atoms and molecules*' Vol. II, Edited by H.Haberland, Springer-Verlag: New York, 77 (1994).

[36] H. W. Kroto, J. R. Heath, S. C. O'Brien, R. F. Curl and R. E. Smalley, *Nature* 318, 162 (1985).

[37] E. E. B. Campbell In '*Clusters of Atoms and Molecules I, Theory, Experiment, and Clusters of Atoms*' Edited by H. Haberland, Springer-Verlag: Berlin 331 (1994).

[38] M. E. Geusic, M. F. Jarrorld, T. J. McIlrath, R. R. Freeman and W. L. Brown, *J. Chem. Phys.* 86, 3862 (1987).

[39] S. Yang, K. J. Taylor, M. J. Craycraft, J. Conceicao, C. L. Pettiette, O. Cheshnovsky and R. E. Smalley, *Chem. Phys. Lett.* 144, 431 (1988).

[40] S. W. McElvany, B. I. Dunlap and A. O'Keefe, *J. Chem. Phys.* 86, 715 (1986).

[41] A. Lahamer, Z. C. Ying, R. E. Haufler, R. L. Hettich and R. N. Compton, In '*Advances in metal and semiconductor clusters*', Vol. 4, Edited by M. A. Duncan, Jai Press Ltd. : London, 179 (1998).

[42] K. A. Caldwell, D. E. Giblin, C. S. Hsu, D. Cox and M. L. Gross *J. Am. Chem. Soc.* 113, 8519 (1991).

[43] B. C. Guo, K. P. Kerns and A. W. Castleman, *Science* 255, 1411 (1992).

[44] B. C. Guo, S. Wei, J. Purnell, S. Buzza and A. W. Castleman, *Science* 256, 515 (1992).

[45] J. S. Pilgrim and M. A. Duncan *J. Am. Chem. Soc.* 115, 6958 (1993).

[46] Adapted from A. Holden, *The Nature of Solids*, copyright Columbia U.P.: New York (1965).

[47] W. A. Saunders, K. Clemenger, W. de Heer and W. Knight, *Phys. Rev. B* 32, 1366 (1985).

[48] C. Brechignac, Ph. Cahuzac and J. Ph. Roux, *Chem Phys. Lett.* 127, 445 (1986).

[49] Ph. Dugourd, D. Rayane, P. Labastie, B. Pintar, J. Chevaleyre, M. Broyer, L. Wöste and J. P. Wolf, *J. de Phys. IV* 1, C7 509 (1991).

[50] A. Hermann, S. Leutweyler and E. Schumacher, L. Woste, *Helv. Chem. Acta* 61, 453 (1978).

[51] K. E. Schriver, J.L. Persson, E.C. Honea and R. L. Whetten, *Phys. Rev. Lett.* 64, 2539 (1990).

[52] W. A. de Heer, P. Milani and A. Chatelain, *Phys. Rev. Lett* 63, 2834 (1989).

[53] M. B. Knickelbein, S. Yang and S. J. Riley, *J. Chem. Phys.* 93, 94 (1990).

[54] M. D. Morse, *Chem Rev.* 86, 1049 (1986).

[55] M. Kappes, R. W. Kunz and E. Schumacher, *Chem. Phys. Lett.* 91, 413 (1982).

[56] F. R. Brühl, R. A. Miron and W. E. Ernst, *J. Chem. Phys.* 115, 10275 (2001).

[57] H. Gohlich, T. Lange, T. Bergmann and T. P. Martin, *Mod. Phys. Lett. B*, 5, 101 (1991).

[58] B. H. Lengsfield III, A. D. McLean, M. Yoshimine, and B. Liu, *J. Chem. Phys.* 79, 1891 (1983).

[59] T. P. Martin, T. Bergmann, H. Gohlich and T. Lange, *Chem. Phys. Lett.* 176, 343 (1991).

[60] T.P. Martin, T. Bergmann and N. Malinowski, *J. Chem. Soc.- Faraday Trans.* 86, 2489 (1990).

[61] P. Dugourd, J. Chevaleyre, C. Bordas and M. Broyer, *Chem. Phys. Lett.* 193, 539 (1992).

[62] T. P. Martin, T. Bergmann and N. Malinowski, *J. Chem. Soc.- Faraday Trans.* 86, 2489 (1990).

[63] D.-S. Yang and P. A. Hackett, *J. Electron Spectrosc. Relat. Phenom.* 106, 153 (2000).

[64] H. Sakurai and A. W. Castleman, Jr., *J. Phys. Chem. A* 102, 10486 (1998).

[65] R. Lombardi and D. M. Lindsay, *J. Chem. Phys.* 106, 8339 (1997).

[66] A. Kaldor, D. M. Cox, D. J. Trevor and M. R. Zakin, In *'Metal Clusters'*, Edited by F. Trager, G. zu Putlitz, Springer–Verlag, (1986).

[67] E. A. Rohling, D. M. Cox and A. Kaldor, *J. Phys. Chem.* 88, 4497 (1984).

[68] Z. Hu, A. Vivoni, J. R.Lombardi and D. M. Lindsay, *J. Chem. Phys.* 103, 3289 (1995).

[69] C.-X. Su and P. B. Armentrout, *J. Chem. Phys.* 99, 6506 (1993).

[70] J. B. Hopkins, P. R. R. Langridge-Smith, M. D. Morse and R. E. Smalley, *J. Chem. Phys.* 78, 1627 (1983).

[71] K. M. Ervin, S. K. Loh, N. Aristov, and P. B. Armentrout, *J. Phys. Chem.* 87, 3593 (1983).

[72] A. Pramann and K. Rademann, *Chem. Phys. Lett.* 347, 46 (2001).

[73] D. M. Cox, D. J. Trevor, R. L. Whetten, E. A. Rohling and A. Kaldor, *Phys. Rev. B* 32, 7290 (1985).

[74] L. S. Wang, J. Conceicao, C. Jin, and R. E. Smalley, *Chem. Phys. Lett.* 182, 5 (1991).

[75] A. J. Cox, J. G. Louderback, and L. A. Bloomfield, *Phys. Rev. Lett.* 71, 923 (1993).

[76] M. D. Morse, G. P. Hansen, P. R. R. Langridgesmith, L. S. Zheng, M. E. Geusic, D. L. Michalopoulos and R. E. Smalley, *J. Chem. Phys.* 80, 5400 (1984).

[77] K. M. Ervin, J. Ho, and W. C. Lineberger, *J. Chem. Phys.* 89, 4514 (1988).

[78] W. Eberhardt, P. Fayet, D. Cox, Z. Fu, A. Kaldor, R. Sherwood and D. Sondericker *Phys. Rev. Lett.* 64, 780 (1990).

[79] D. E. Powers, S. G. Hansen, M. E. Geusic, A. C. Puiu, J. B. Hopkins, T. G. Dietz, M. A. Duncan, P. R. R. Langridge-Smith, and R. E. Smalley, *J. Phys. Chem.* 86, 2556 (1982).

[80] R. E. Haufler, L. S. Wang, L. P. F. Chibante, C. Jin, J. Conceicao, Y. Chai, and R. E. Smalley, *Chem. Phys. Lett.* 179, 449 (1991).

[81] M. Ruppel and K. Rademann, *Chem. Phys. Lett.* 197, 280 (1992).

[82] B. Kaiser and K. Rademann, Z. Phys. D. Atoms, Molecules and Clusters 19, 227 (1990).

[83] L. Hanley and S. L.Anderson, J. Phys. Chem. 91, 5161 (1987).

[84] M. F. Jarrold, J. E. Bower and J. S. Kraus, J. Chem. Phys. 86, 3876 (1987).

[85] D. L. Barr, J.Vac. Sci. Technol. B, 5, 184 (1987).

[86] F. G. Rudenauer, W. Steiger, H. Studnicka and P. Pollinger, Int. J. Mass Spectrom. Ion Processes 77, 63 (1987).

[87] D. S. Ginter, M. L. Ginter and K. K. Innes, J. Chem. Phys. 69, 480 (1965).

[88] G. Gantefor, M. Gaussa, K. H. Meiwes-Broer and H. O. Lutz, J. Chem. Soc. Faraday Trans. 86, 2483 (1990).

[89] J. R. Heath, Y. Liu, S. C. O'Brien, Q.-L. Zhang, R. F. Curl, F. K. Tittel, and R. E. Smalley, J. Chem. Phys. 83, 5520 (1985).

[90] K. LaiHing, R. G. Wheeler, W. L. Wilson, and M. A. Duncan, J. Chem. Phys. 87, 3401 (1987).

[91] R. D. Beck, M. Hineman and J. W. Nibler, J. Chem. Phys., 92, 7069 (1990).

[92] J. A. Zimmerman, S. B. H. Bach, C. H. Watson, and J. R. Eyler, J. Phys. Chem. 95, 98 (1991).

[93] K. Sattler, J. Mühlbach, and E. Recknagel, Phys. Rev. Lett. 45, 821 (1980).

[94] M. Treilleux, G. Fuchs, F. S. Aires, P. Melinon, A. Hoareau and B. Cabaoud, Z. Phys. D 20, 263 (1991).

[95] S. Metejcik, P. Stampfi, A. Stamatovic, P. Scheier and T. D. Mark, J. Chem. Phys. 111, 3548 (1999).

[96] J. T. Snodgrass, J. V. Coe, K. M. McHugh, C. B. Freidhoff, and K. H. Bowen, J. Phys. Chem. 93, 1249 (1989).

[97] F. Steinkemeier, J. Higgins, W. E. Ernst, and G. Scoles, Phys. Rev. Lett. 74, 3592 (1995).

[98] H. Heinze, P. Borrmann, H. Stamerjohanns and E. R. Hilf, Z. für Physik D Atoms, Molecules and Clusters 40, 190 (1997).

[99] U. Buck and H. Meyer, Phys. Rev. Lett. 52, 109 (1984).

[100] J. Stapelfeldt, J. Wörmer and T. Möller, Phys. Rev. Lett.. 62, 98 (1989).

[101] Y. L. Shao, T. Ditmire, J. W. G. Tisch, E. Springate, J. P. Marangos and M. H. R. Hutchinson, Phys. Rev. Lett. 77, 3343 (1996).

[102] Y. Liu, Q.-L. Zhang, F. K. Tittel, R. F. Curl and R. E. Smalley, *J. Chem. Phys.* 85, 7434 (1986).

[103] Q.-L. Zhang, Y.Liu, R. F. Curl, F.K. Tittel and R. E. Smalley, *J. Chem. Phys.* 88,1670 (1988).

[104] A. A. Guzelian, U. Banin, J. C. Lee and A. P. Alivisatos, In *'Advances in Metal and Semiconductor Clusters'* Vol. 4,Edited by M. A. Duncan, Jai Press Ltd.: London (1998).

[105] G. W. Lemire, G. A. Bishea, S. A. Heidecke and M. D. Morse, *J. Chem. Phys.* 92, 121 (1990).

[106] Q.-L. Zhang, Y. Liu, R. F. Curl, F. K. Tittel and R. E. Smalley, *J. Chem. Phys.* 90, 4258 (1989).

[107] K. D. Kolenbrander and M. L. Mandich, *J. Chem. Phys.* 90, 5884 (1989).

[108] K. D. Kolenbrander and M. L. Mandich, *J. Chem. Phys.* 92, 4759 (1990).

[109] W. T. Tysoe, G. L. Nyberg and R. M. Lambert, *J. Chem. Soc. Chem. Commun* 623 (1983).

[110] U. Heiz, A. Sanchez, S. Abbet and W.-D. Schneider, *Chem. Phys.* 262, 189 (2000).

[111] Z. Y. Chen, G. J. Walder, and A. W. Castleman, Jr. *Phys. Rev B* 49, 2739 (1994).

[112] M. E. Geusic, M. D. Morse, S. C. O'Brien, and R. E. Smalley, *Rev. Sci. Instrum.* 56, 2123 (1985).

[113] D. E. Bergeon and A.W. Castleman, Jr., *J. Chem. Phys.* 117, 3219 (2002).

[114] F. Steinkemeier, J. Higgins, W. E. Ernst and G. Scoles, *Phys. Rev. Lett.* 74, 3592 (1995).

[115] C. Guet and L. Plagne, In *'Theory of Atomic and Molecular Clusters'* Edited by J. Jellinek, Springer-Verlag: Berlin, Heidelberg, 209 (1999).

[116] T. P. Martin, S. Bjornholm, J. Borggreen, C. Brechignac, Ph. Cahuzac, K. Hansen and J. Pederson, *Chem. Phys. Lett.* 186, 53 (1991)

[117] S. M. Riemann, M. Brack and K. Hansen, *Z.Phys. D.* 28 235 (1993).

[118] S. Bjornholm, *Contemporary Physics* 31, 309 (1990).

[119] D. A. Jelski, T. F. George, and J. M. Vienneau, In *'Clusters of atoms and molecules I'* Edited by. H. Haberland, Springer-Verlag: Berlin, Heidelberg, 50 (1994).

[120] D. A. Salahub, A. Martinez and D. Wei, In *'Theory of atomic and molecular clusters'* Edited by J. Jellinek, Springer-Verlag: Berlin Heidelberg, 157 (1999).

[121] D. Q. Wei, and D. R. Salahub, *J. Chem. Phys.* 106, 6086 (1997).

[122] R. O. Watts and I. J. McGee, *'Liquid state chemical physics'*, Wiley-Interscience: New York (1976).

[123] J. M. Soler, J. J. Saenz, N. Garcia and D. Echt, *Chem. Phys. Lett.* 109, 71 (1984).

[124] J. R. Reimers and R. O. Watts, *Chem. Phys.* 85, 83 (1984).

[125] R. E. Miller, R. O. Watts and A. Ding, *Chem. Phys.* 83, 155 (1984).

[126] R. Car and M. Parrinello, *Phys. Rev. Lett.* 50, 55 (1985).

[127] N. Binggeli and J. R. Chelikowsky, *Phys. Rev. B* 50, 11764 (1994).

[128] J. R. Chelikowsky, S. Öğüt, I. Vasiliev, A. Stathopoulos and Y. Saad In *'Theory of Atomic and Molecular Clusters'* Edited by J. Jellinek, Springer-Verlag: Berlin, Heidelberg, 136 (1999).

[129] P. Milani, A. Podesta, P. Piseri, E. Barborini, C. Lenardi and C. Castelnovo, *Diamond and Related Materials* 10, 240 (2001).

[130] L. Diederich, E. Barborini and P. Piseri, *Appl. Phys.Lett.* 75, 2662 (1999)

[131] A. C. Ferrari, B. S. Satyanarayana and J. Robertson *Europhys. Lett.* 46, 245 (1999).

[132] A. F. Hebard, M. J. Rosseinsky, R. C. Haddon, D. W. Murphy, S. H. Glarum, T. T. M. Palstra, A. P. Ramirez and A. R. Kortan, *Nature* (London), 350, 600 (1991).

2. Scope of the present investigations

2.1 Design and Fabrication of the cluster beam apparatus

A variety of cluster sources have been designed to generate free or gas-phase clusters whose study provides information on the structural, binding and reactive properties of clusters in the absence of any interaction from a supporting matrix or a substrate. The earliest cluster sources known are the Knudsen cell [1] and the gas aggregation cell [2]. Knudsen cell was employed for generating clusters of materials with high to medium cohesive energies- refractory and ionic materials, respectively. The gas aggregation cells were employed for intermediate to low binding energy materials (0.3- 0.5 eV/atom). The cluster beams from the above sources, however, are not really reproducible in nature. Supersonic beam techniques on the other hand, can generate reproducible cluster beams. This method is based on the principle of expanding the vapor of a material at high pressure through a small orifice into a low-pressure zone. This causes cooling of the atoms or molecules due to the several collisions among themselves. The cooling can be further enhanced by the use of a seed or carrier gas, typically an inert gas that helps further condensation of the species by removing excess heat energy. "Pulsed cluster beams" have become popular owing to their high instantaneous intensities and large cluster content. Pulsed laser vaporization method in conjunction with supersonic expansion was pioneered by Smalley and co-workers [3] who discovered the C_{60} molecule by this method.

For mass detection, usually a time–of–flight mass spectrometer (TOF-MS) is used in the characterization of clusters for the past several decades and has become popular in cluster science primarily owing to their large mass range. Wiley and

McLaren's design [4] was the first to be commercialized. TOF-MS is based on the principle of segregating ions on the basis of velocity distribution. The mass resolution of the instrument was further improved by the invention of Reflectron-TOF-MS by Mamyrin [5] by correcting the effects due to the initial spread in the kinetic energy of the ions. Commercially available time-of-flight mass spectrometers have typical resolution of 1000-1500 and are not tailored for specific requirements of most research-oriented work.

We undertook the design and fabrication of a cluster source attached with a Time-of-Flight mass spectrometer (TOF-MS) since commercial ones are not readily available suiting specific objectives and even if, some parts are available, they are rather expensive. Our cluster source is based on the principle of pulsed laser vaporization in conjunction with pulsed supersonic expansion [3]. Important components in the TOF-MS design are the ion source, mass analyzer, ion optics and detector. We use a pulsed laser (Nd-YAG, GCR-100 series, 10 Hz) in the ion source. A high voltage source (3000 Volts) is used to supply the electric field to the mesh grids placed at the location of ion-generation, which acts as the mass analyzer. A reflectron-grid arrangement was also introduced to improve the resolution of the mass spectrometer. The ion optics involves pair of deflector plates to steer the cluster beam along with electrostatic lenses- "Einzel Lenses" used for focussing the beam. A micro-channel plate detector in Chevron geometry is employed for detecting the incoming cluster ions. They are ideally suited for detecting charged particles with high detection efficiency of about 55-65% and having a linear response by maintaining a constant gain when exposed to varying input levels. Our studies mainly dealt with the formation of molecular clusters and the reactivity of elemental carbon clusters and compound clusters of oxides.

2.2 Alcohol-water clusters: Surface-enrichment in alcohol-water liquid mixtures

Alcohol and water clusters belong to the class of molecular clusters that have been studied extensively. A major focus of research on such gas phase clusters is based on probing the vibrational and rotational states in order to throw some light on the excited state dynamics of such complexes. Structural information on water and methanol clusters has been obtained from molecular beam electric deflection experiments (see section 1.4 for more details). It has been found that water and methanol clusters of small nuclearity are very similar in their geometry.

Mixed clusters of water and alcohols $(ROH)_n(H_2O)_mH^+$ where ROH is CH_3OH and C_2H_5OH, are produced by co-expansion of the vapor through a nozzle. Several workers have investigated the preferential solvation of the hydrogen ions in mixed clusters of water, methanol and ethanol [6,7]. They report that for smaller cluster sizes, alcohol molecules are preferentially attached to the proton while for larger clusters, the water molecules are more strongly bound to the proton. The structure of clusters in methanol-water binary solutions (via adiabatic expansion in vacuum) has also been studied by mass spectrometry and X-ray diffraction [8]. They proposed that chain-like clusters present in methanol-rich mixtures give way to tetrahedral species as the water content increases.

It is known that when alcohol molecules are added to an aqueous solution, they have the tendency to segregate to the surface. Our objective was to see if molecular clusters of the type $(ROH)_n(H_2O)_mH^+$ (ROH = CH_3OH, C_2H_5OH, C_3H_7OH, C_4H_9OH) sampled from the liquid surface can provide information on the structure of the liquid surface itself. In this context, we specifically looked at the surface enrichment by alcohol molecules in the water-alcohol mixtures. For this

purpose, we generated a cluster beam of the binary vapor swept off the surface of the alcohol-water liquid mixture and analyzed the clusters thus formed using the TOF-MS. The vapor mole fractions of the alcohols and water as a function of the liquid mole fraction were estimated.

There has been some study in the past [9] to understand the compositional dependence of surface tension in alcohol-water mixtures. There have been few efforts to explore the phenomenon of surface-enrichment by alcohol molecules using techniques such as neutron diffraction [10]. Our results not only compare well with those from neutron diffraction and surface tension but also allow a direct determination of surface-enrichment over the entire molar composition of the alcohol-water mixture.

As a step further, we investigated the phenomenon of competitive surface-enrichment when two alcohols are present in equal proportions in ternary water-alcohol-alcohol liquid mixtures.

2.3 Studies of a few cluster species and their reactivities

There have been many studies on the reactivity of gas-phase elemental clusters produced in pulsed cluster sources from number of materials, including transition-metals, semiconductors and carbon. Thus, many metal-carbide, -nitride and -silicide clusters have been produced by co-expansion of the metal plume, produced by laser ablation, and the desired reactant gas seeded in an inert carrier gas atmosphere [11]. Other methods involve the use of fast flow reactors with the reaction taking place in a flow tube in which the various reactant gases are introduced independently at different times. Carbon clusters, being one of the most easy to nucleate have been studied extensively for reactivity [12].

We were interested in exploring the formation of C-N clusters by carrying out laser ablation of graphite in the presence of nitrogen containing molecules. There have been a few prior attempts in this regard to insert nitrogen atoms into carbon clusters [13,14], a well-known case being a single nitrogen atom being inserted into C_n cluster anions (n ≤ 7). Smalley and co-workers [15] studied the vaporization of graphite in the presence of small amounts of reactant gas like NH_3 and CH_3CN entrained in a He carrier gas pulse and proposed the formation of polar cyanopolyynes species of the type HC_7N and HC_9N. However, they reported formation of only limited number of species and the study was brief. Hence, we carried out the laser ablation of graphite in the presence of a varying NH_3/He ratio. *Contrary to their findings, new adducts of the type $(HCN)_m(NH_3)_nH^+$ are formed* under the experimental condition employed by us. We have carried out molecular-orbital calculations to substantiate the stability pattern of the observed clusters.

The second part of the reactivity work was to do with the reactive laser ablation of compounds, specifically oxides of group 13 and 14 elements, in the presence of N_2 or NH_3 in a supersonic He jet. Nitrides of group 13 elements such as B, Al and Ga are all technologically important materials. Nanotubes and nanowires of group 13 and 14 elements have also been synthesized recently by several workers [16-18]. Our interest was to find out the mechanism of formation of nitrides or oxynitrides by the reaction of the above oxides with N_2 or NH_3. Towards this, we thought it important to investigate whether the nitridic or oxynitridic species are formed in the vapor phase. The role of carbon in the formation of nitrides or oxynitrides has also been examined.

2.4 Preliminary investigations of the laser ablation of MoS_2 and MoS_3.

There are a number of different types of experiments that can be conducted with gas phase clusters, as mentioned before, such as study mass abundance and spectroscopy in vacuum or deposit them on substrates to carry out topographic studies using various microscopy techniques. There has been, of late, some efforts in depositing nanocrystalline assembled films on substrates using molecular beam cluster sources [19-21]. This way of depositing films offers the advantage of selecting the mass distribution of nanoparticles deposited. For a given kinetic energy of the cluster beam, the impact of the clusters deposited may be controlled by appropriately selecting the substrate potential, its temperature and placement.

Our aim in this study was to investigate the formation inorganic fullerene-like structures starting from MoS_2, MoS_3 and WS_2. There has been some work reporting the formation inorganic fullerenes of MoS_2, MoS_3 and WS_2 by heating thin films of the metal (Mo and W) in an atmosphere of hydrogen sulphide [22,23]. They have been also produced by heating the oxides of molybdenum (MoO_3) and tungsten (WO_3) in H_2S atmosphere [24]. Recently, MoS_2 and WS_2 inorganic fullerene-like structures have also been produced by laser ablation of MoS_2 and WS_2 in an argon atmosphere in electric furnace heated to different temperatures [25]. We have employed laser ablation of these materials in an atmosphere of pulsed jet-cooled helium as well as laser ablation in a solvent medium providing excess sulphur. Our preliminary study indicates that the laser ablation in solvent medium is more favorable in the formation of the concentric layers of MoS_2 around the core of the nanoparticles.

References

[1] K. Hilpert *'Chemistry of inorganic vapors. Structure and Bonding'* 73, 99 (1990).

[2] K. Sattler, J. Muhibach and E. Recknagel, *Phys. Rev. Lett.* 45, 821 (1980).

[3] H. W. Kroto, J. R. Heath, S. C. O'Brien, R. F. Curl and R. E. Smalley, *Nature* 318, 162 (1985).

[4] W. C. Wiley and I. H. McLaren, *Rev. Sci. Instrum* 26, 1150 (1955).

[5] B. A. Mamyrin, V. I. Karatev, D. V. Shmikk and V. A. Zagulin, *Sov. Phys. JETP* 37, 45 (1973).

[6] P. Kebarle, R. N. Haynes and J. G. Collins, *J. Am. Chem. Soc.* 89, 5753 (1967).

[7] A. J. Stace and A. K. Shukla, *J. Am. Chem. Soc.* 104, 5314 (1982).

[8] T. Takamuku, T. Yamaguchi, M. Asato, M. Matsumoto and N. Nishi, *Z. Naturforsch* 55a, 513 (2000).

[9] D. Myers, *'Surfaces, Interfaces, and Colloids, Principles and Applications'* VCH: New York (1991).

[10] Z. X. Li, J. R. Lu, D. A. Styrkas, R. K. Thomas, A. R. Rennie and J. Penfold, *J. Mol. Phys.* 80, 925 (1993).

[11] Z. Y. Chen, G. J. Walder and A. W. Castleman, Jr., *Phys. Rev. B* 49, 2739 (1994).

[12] C. Lifshitz, *Int. J. of Mass Spectrom.* 200, 423 (2000).

[13] J. C. Hummelen, B. Knight, J. Pavlovich, R. Gonzalez and F. Wudl, *Science* 269, 1554 (1995).

[14] Z. C. Tang, R. B. Huang, L. Shi and L. S. Zheng, *Int. J. Mass Spectrom. Ion Processes* 151, 55 (1995).

[15] J. R. Heath, Q. Zhang, S. C. O'Brien, R. F. Curl, H. W. Kroto and R. E. Smalley, *J. Am. Chem. Soc.* 109, 359 (1987).

[16] F. L. Deepak, C. P. Vinod, K. Mukopadhyay, A. Govindaraj and C. N. R. Rao, *Chem. Phys. Lett.* 353, 345 (2002).

[17] Y. Zhang, J. Liu, R. He, Q. Zhang, X. Zhang and J. Zhu, *Chem. Mater.* 13, 3899 (2001).

[18] F. L. Deepak, A. Govindaraj and C. N. R. Rao, *J. Nanosci. and Nanotech.* 1, 303 (2001).

[19] P. Milani, A. Podesta, P. Piseri, E. Barborini, C. Lenardi and C. Castelnovo, *Diamond and Related Materials* 10, 240 (2001).

[20] E. F. Garvey, M. P. Joshi, R. L. Deleon, P. N. Prasad and J. F. Garvey, Rev. Sci. Instrum. 69, 3028 (1998).

[21] D. A. Easthum, J. Phys. D: Appl. Phys. 28, 2176 (1995).

[22] L. Margulis, G. Salitra, R. Tenne and M. Talianker, *Nature* 365, 113 (1993).

[23] R. Tenne, L. Margulis, M. Genut and G. Hodes, *Nature* 360, 444 (1992).

[24] Y. Feldman, E. Wasserman, D. J. Srolovitz and R. Tenne, *Science* 267, 222 (1995).

[25] R. Sen, A. Govindaraj, K. Suenaga, S. Suzuki, H. Kataura, S. Iijima and Y. Achiba, *Chem. Phys. Lett.* 340, 242 (2001).

3. Design and fabrication of the cluster beam apparatus*

SUMMARY

The design and fabrication of a Smalley-type cluster source in combination with a reflectron based time-of-flight mass spectrometer are reported. The generation of clusters is based on supersonic jet expansion of the sampling plume. Sample cells, for both liquids and solid targets, developed for this purpose are described. Two pulsed Nd-YAG lasers are used in tandem, one (532 nm) for target vaporization and the other (355nm) for cluster ionization. Methanol clusters of nuclearity up to 20 (mass, 640 u) were produced using the liquid sample cell. The clusters were detected with a mass resolution of ~ 2500 in the R-TOF geometry. Carbon clusters up to a nuclearity of ~ 100 were obtained by pulsed laser ablation of graphite using the solid sample cell.

3.1 Introduction

Clusters of metals and semiconductors have been studied in the form of colloids [1], as adsorbed species on substrates in vacuum [2] as well as in molecular beams [3,4]. Cluster generation in the vapor phase is particularly advantageous in that clusters of any substance may be obtained devoid of surfactants or capping agents. A number of groups worldwide, to name a few- Smalley et al. [5], Castleman et al. [6], Milani et al [7], have developed cluster sources attached with time-of-flight mass spectrometers of high mass range and resolution. In India, the first reflectron type TOF-MS was built at IGCAR, Kalpakkam [8] and used for thermodynamic studies such as vaporization behavior of refractory materials. We decided to take up the fabrication of a cluster generation source attached with time-of-flight mass spectrometer, to study the formation and reactivity of gas-phase clusters of a variety of materials.

Essentials of a cluster beam apparatus

The main components of a cluster beam apparatus are a cluster source and a mass spectrometer along with appropriate vacuum attachments. Simple cluster sources such as Knudsen cell [9] or inert gas condensation source [10] have been used extensively in the past. More recently, inert gas pulsed valves operating in the range of few microseconds are being used to realize supersonic jet beams. Such beams are known for good cluster yields and lower internal energies of clusters (~few kelvins) [11]. The clusters produced in a molecular beam are mostly neutral and need to be ionized in the mass spectrometer. Ions of different mass-to-charge ratio can be separated by electrostatic deflection, magnetic deflection or using a combination of the two. Quadrupole mass spectrometers on the other hand are based

on selective response of ions to rf and dc electric fields. Time-of-flight mass spectrometers segregate ions according to their velocities and are ideally suited for cluster studies owing to their high resolution, selectivity and mass range.

Principle of time-of-flight mass spectrometry

The Time-of-flight (TOF) mass spectrometer is based on the principle of sorting clusters according to their difference in velocities in a mono-energetic beam. A schematic of the linear TOF-MS is shown in Figure 3.1 below.
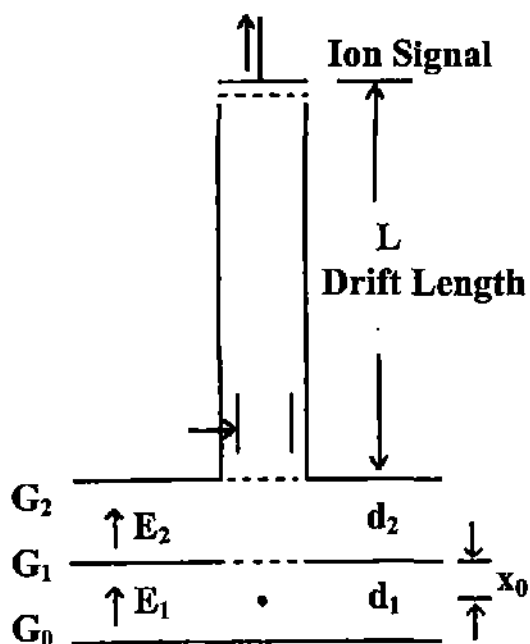
Fig. 3.1 Schematic of Linear-TOF mass spectrometer. G_0, G_1 and G_2 are the repeller, extraction and acceleration grids, respectively with spacings of d_1 and d_2 between them. Ionization of the clusters takes place at x_0, the midpoint between G_0 and G_1 and L is length of the field-free region between G_2 and the detector.

The ionization takes place between the grids G_0 and G_1, which is also referred to as the extraction zone and the acceleration takes place between G_1 and G_2 (the acceleration zone). The distance between the ionization center and G_1 is 'x_0' and L is the length of the field free region between G_2 and the detector.

Consider that singly charged ions are produced in a small volume of a gas. When these ions are accelerated through a potential V, they acquire a kinetic energy eV where 'e' is the charge of the ion.

Since, $eV = 1/2\ mv^2 \Rightarrow v = [2eV/m]^{1/2}$ (3.1)

If this ion packet is allowed to travel a distance 'L', then the time taken for the travel 'T' is given by

$$T = L/v = L\ m^{1/2}/[2eV]^{1/2}$$ (3.2)

The electric fields between the first pair of grids 'E_1' and the second pair of grids 'E_2' are given by:

$$E_1 = (V_1 - V_0)/d_1 \qquad E_2 = (V_2 - V_1)/d_2$$ (3.3)

where V_0, V_1 and V_2 are the potentials applied to the grids G_0, G_1 and G_2.

Velocity 'v_1' acquired by the ion at G_1

Following equations (3.2) and (3.3), if the mass and charge of the ion is 'm' and 'z' respectively, then

$$v_1 = \{2(z/m)E_1x_0\}^{1/2}$$ (3.4)

v_1 depends on where the ion is produced, hence causing the spread in the initial velocities.

Velocity 'v_2' acquired by ion at G_2

There is no further spread in the velocity as all ions travel the same distance. Keeping the $E_1 < E_2$ ensures minimum overall energy spread for a given velocity in the drift region.

After G_2

The ion travels with velocity v_2 in a field free region.

Therefore, the time of flight 'T' of a given mass is given by:

$$T = (v_1 - v_0)/a_1 + (v_2 - v_1)/a_2 + L/v_2$$ (3.5)

54·

where 'v_0' is the component of the initial velocity of ion due to the thermal motion and 'a_1' and 'a_2' are the accelerations in the extraction and acceleration zone, respectively.

Focussing conditions

In reality, the ions in the extraction region (between grids G_0 and G_1) do not have the same energy (see Fig. 3.1). This is because there is a distribution in the magnitude as well as direction of the ion velocities on account of thermal motion. Also, the ions are not produced at the same point in space and time and hence get accelerated to different velocities in the accelerating field. These factors cause a spread in the initial velocities of the ions at the start of their trajectory, through the field free zone. Consequently, one obtains broad peaks at different mass numbers. Hence, we need to apply certain focussing conditions in order to compensate for these effects.

First order focussing condition → $(dT/dx_0) = 0$ (3.6)

(Space focussing)

For a given d_1, d_2 and L, this is achieved for a particular ratio of E_1 and E_2. The best possible resolution achievable at room temperature is about 200. This can be improved to around 4000 by cooling the sample using a supersonic jet.

Second order focusing condition → $(d^2T/dx_o^2) = 0$ or $dT/dv_0 = 0$ (3.7)

(Velocity focusing)

To achieve velocity focusing we must make E_1 tend to ∞ or v_0 tend to zero. Mamyrin et al. [12] added an electrostatic mirror, to the linear TOF geometry, that could reflect the ions and thereby greatly improve the resolution via double-focussing. This modified TOF is called the reflectron time-of-flight mass

spectrometers (R-TOF MS). The resolution 'R' of the TOF is given by T/2ΔT, where 'T' is the time of flight and 'ΔT' is the peak width at FWHM. Resolution of above 30,000 have been reported for these R-TOF mass spectrometers, by Bergmann et al. [13]. In recent years, this technique has become a powerful tool in a variety of fields ranging from biological sciences- study of large macromolecules (using MALDI - Matrix assisted laser desorption / Ionization [14]), atomic and molecular clusters to material characterization. The schematic of a typical cluster system with R-TOF built in our group is shown in Fig. 3.2.

3.2 Design and fabrication

Vacuum system

Figure 3.2 shows the system with two vacuum chambers separated by a gate valve and a flight-tube attached to the second chamber. The two chambers were designed for cluster generation and mass detection, respectively. Engineering drawings of the system were prepared using the AutoCAD software (see Fig. 3.3). The vacuum chambers were locally fabricated (New Poona Industries, Poona). The chambers are connected through knife-edge flanges using copper gaskets. The first chamber is pumped by an oil diffusion pump (Varian Vacuum Products, USA) with a pumping speed of 1200 lit/sec, attached with a liquid nitrogen trap while the second chamber along with the flight-tube is connected to a turbomolecular pump (Alcatel, France) with pumping speed of 900 lit/sec. The diffusion and the turbomolecular pumps are backed by separate rotary pumps. A magnetron and an ion-gauge (Edwards, UK) are employed to read vacuum in the first and the second chamber, respectively. The vacuum system was first assembled on a metal frame. Fittings such as the ion gauge head and the gate valve were tested for vacuum leak

Fig. 3.2 A schematic drawing of the cluster source attached to the time-of-flight mass spectrometer: PSV; pulsed supersonic valve, MCP; microchannel plate detector, sc; sample cell, sm; stepper motor, sk; skimmer, sl; slit, dl; deflection plates, el; einzel lens, x_0; point of ionization, VL; vapourization laser, IL; ionization laser, G_0, G_1 & G_2; the repeller, extractor and accelerator grids, R_0-R_5; reflectron grids, D. P.; diffusion pump, TMP; turbomolecular pump and GV; gate valve.

AUTOCAD DRAWINGS OF VACUUM CHAMBERS

(a)

PLAN

SECTION — EE
FROM PLAN VIEW

(b)

LEFT SIDE VIEW

SECTIONAL ELEVATION — BB

FROM PLAN VIEW

59

(c)
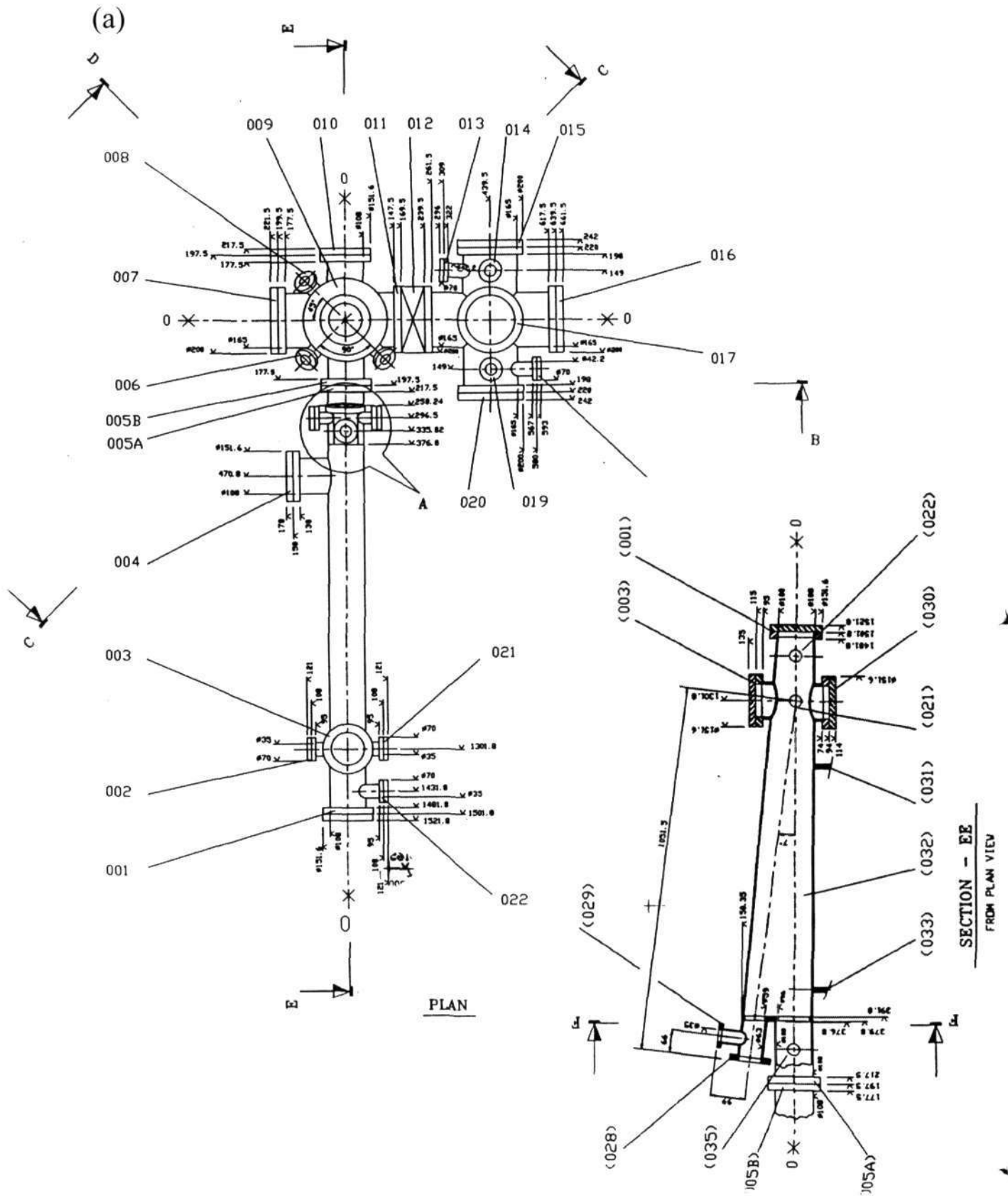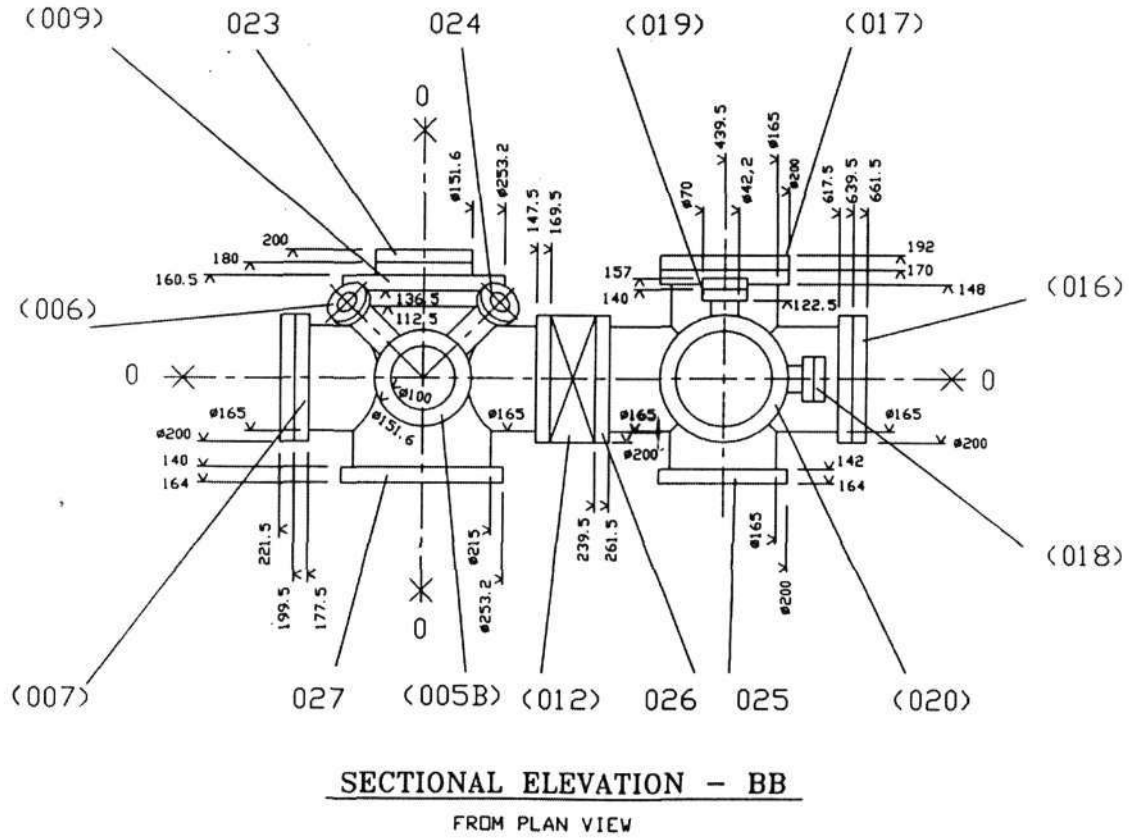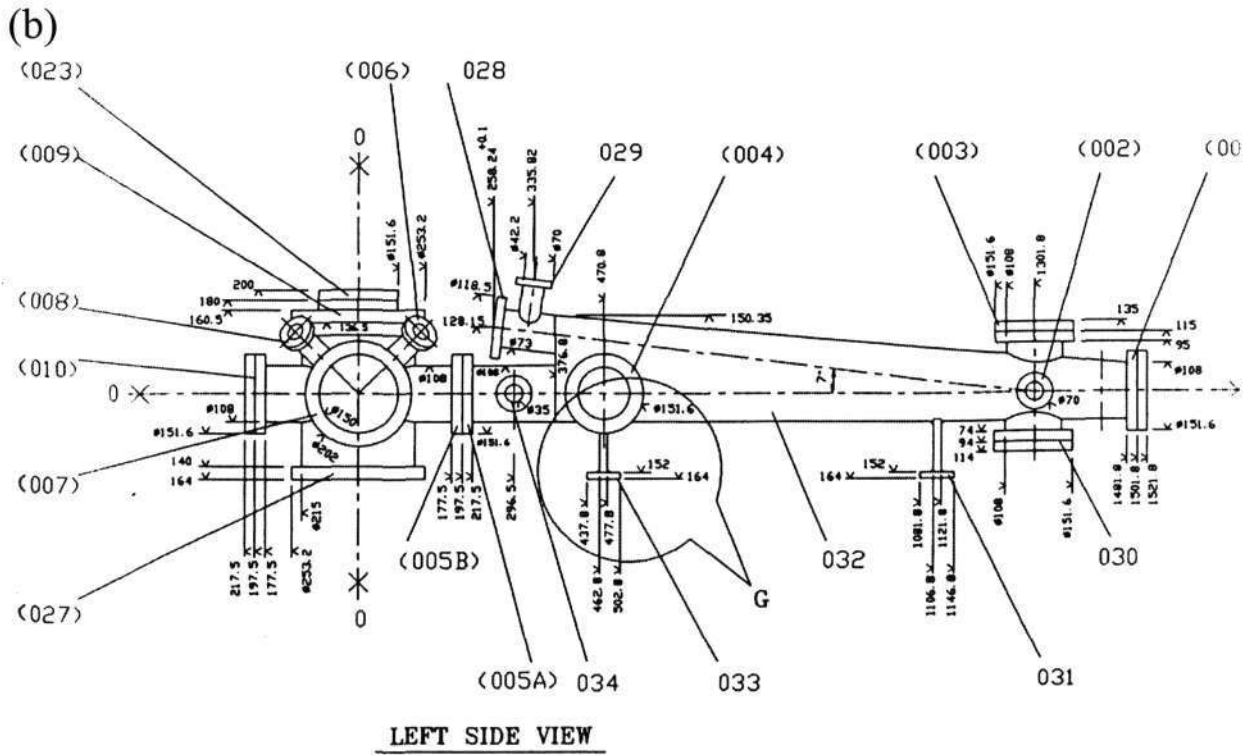
NOTE,

DUMMY FLANGE IS TO BE PROVIDED TO ALL PORTS.

FIXED FLANGE HOLES ORIENTATION SHOULD MATCH
WITH ITS COUPLING FLANGE IN ASSEMBLY.

NO.	DESCRIPTION	TYPE	SIZE
35	CONFLAT FLANGE PORT	FIXED	CF35
34	CONFLAT FLANGE PORT	FIXED	CF35
33	SUPPORT LEG		
32	OVAL CHAMBER		
31	SUPPORT LEG		
30	CONFLAT FLANGE PORT	FIXED	CF100
29	CONFLAT FLANGE PORT	FIXED	CF35
28	CONFLAT FLANGE PORT	FIXED	CF63
27	CONFLAT FLANGE PORT FOR TURBO PUMP	ROTATE	CF200
26	CONFLAT FLANGE PORT CONNECTING GATE VALVE	ROTATE	CF150
25	CONFLAT FLANGE PORT FOR DIFFUSION PUMP	ROTATE	CF150
24	CONFLAT FLANGE PORT	FIXED	CF35
23	CONFLAT FLANGE PORT	FIXED	CF100
22	CONFLAT FLANGE PORT	FIXED	CF35
21	CONFLAT FLANGE PORT	FIXED	CF35
20	CONFLAT FLANGE PORT	FIXED	CF150
19	CONFLAT FLANGE PORT	FIXED	CF35
18	CONFLAT FLANGE PORT	FIXED	CF35
17	CONFLAT FLANGE PORT	FIXED	CF150
16	CONFLAT FLANGE PORT	FIXED	CF150
15	CONFLAT FLANGE PORT	FIXED	CF150
14	CONFLAT FLANGE PORT	FIXED	CF35
13	CONFLAT FLANGE PORT	FIXED	CF35
12	GATE VALVE		
11	CONFLAT FLANGE PORT CONNECTING GATE VALVE	ROTATE	CF150
10	CONFLAT FLANGE PORT	FIXED	CF100
9	CONFLAT FLANGE PORT	FIXED	CF200
8	CONFLAT FLANGE PORT	FIXED	CF35
7	CONFLAT FLANGE PORT	ROTATE	CF150
6	CONFLAT FLANGE PORT	FIXED	CF35
5B	CONFLAT FLANGE PORT	ROTATE	CF100
5A	CONFLAT FLANGE PORT	FIXED	CF100
4	CONFLAT FLANGE PORT	ROTATE	CF100
3	CONFLAT FLANGE PORT	FIXED	CF100
2	CONFLAT FLANGE PORT	FIXED	CF35
1	CONFLAT FLANGE PORT	FIXED	CF100

Fig. 3.3 (a) & (b) Engineering drawings of vacuum chambers of the cluster beam apparatus drawn using AUTOCAD version 13.0 (c) Legend for the various parts of chambers.

using a residual gas analyzer. After baking, a vacuum of $\sim 10^{-9}$ torr is obtained routinely in both the chambers.

Cell Design

A number of source designs are now available for clusters of main group elements and alloys. However, a cluster source producing high intensities of size selected, cooled clusters for a wide range of sizes and materials is yet to be perfected [15]. Usually, some compromises are made in the choice of the cluster source keeping in mind a particular experimentation. The important criteria for a good cluster source are cluster size tunability, intensity profiles, instantaneous output and internal temperature of the clusters. A combination of laser evaporation along with inert gas condensation has proved to be a good technique to generate large clusters from refractory materials such as transition metals as well as carbon and silicon. For such sources, it is important to have a uniform ablation of the target material, which is achieved by continuously moving the target in a predetermined fashion. This ensures reproducible cluster beams. The shape of the thermalization room inside the cluster source- where the plume of the target material and the inert carrier gas atoms mix intimately- as well as the time provided for such an interaction, play important roles in the determination of the cluster size distribution obtained. Finally, shape and the dimension of the expansion nozzle also affect the cooling of the clusters. Mostly, pulsed lasers are used for such sources and the higher the repetition rate, higher is the instantaneous output. Pulsed lasers with repetition rates of about a few kHz produce near continuous beams of clusters.

The clusters, in the molecular beam attain supersonic velocities due to the expansion of the gaseous mixture from a high-pressure region into the vacuum
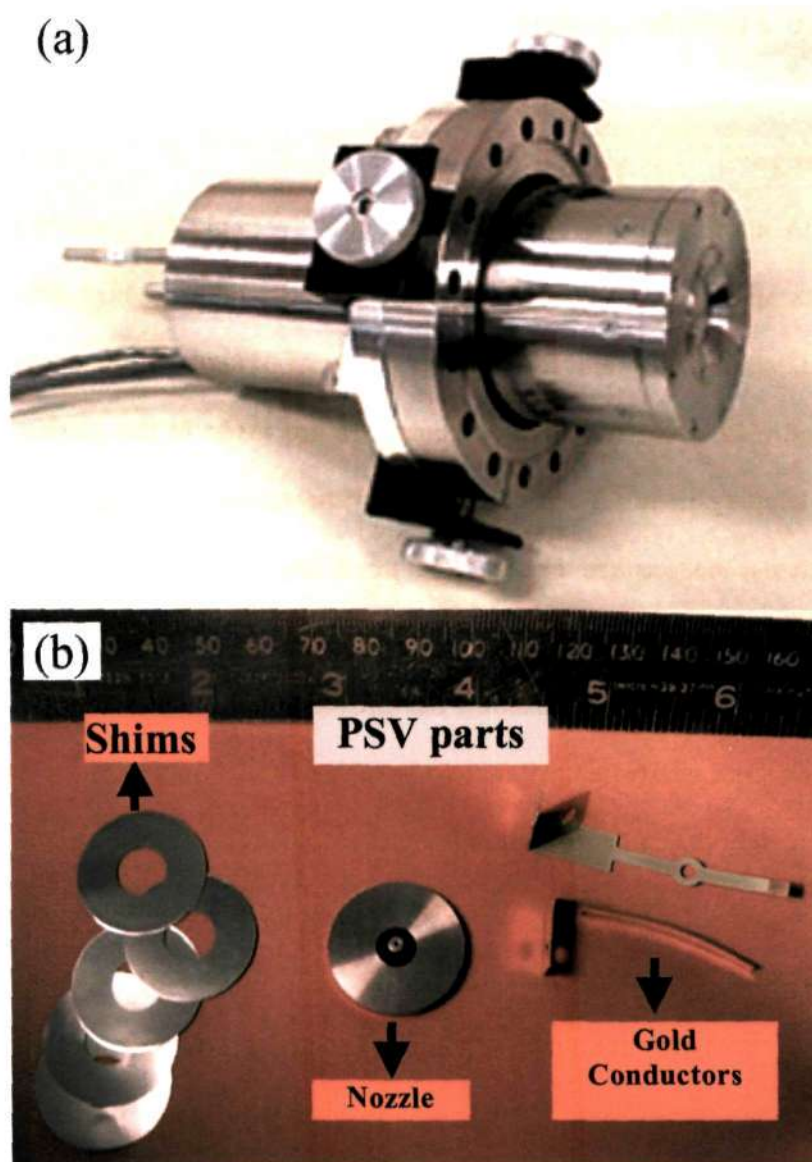
Fig. 3.4 (a) Photograph of the pulsed supersonic valve PSV (R. M. Jordan Company, CA, USA) (b) Some internal parts of PSV: Shims, nozzle and gold conductors. The PSV operates by the application of a high current pulse (~ kAmps) for µs to two parallel gold conductors which lift against each other so as to admit the carrier gas for a short duration into the vacuum chamber.

region, through a small orifice. In order to extract the central beam, a skimmer is placed at an appropriate distance from the nozzle and it serves the purpose of separating regions of different pressures. The design of the skimmer is based on aerodynamic considerations and its edge should be very sharp and polished so as to avoid any interference with the oncoming supersonic cluster pulse.

Several variations in the cell design have been tried out in the laboratory. In one standard design [16], a sample cell in combination with a pulsed supersonic valve (R.M. Jordan, USA) is placed in the first chamber behind a slit-skimmer assembly. A photograph of the pulsed supersonic valve along with various internal components is shown in Fig. 3.4. A threaded arrangement was made to fix the designed sample cell in front of the pulsed supersonic valve such that the mouth of the cell mates with the mouth of the pulsed valve, both carrying orifices of similar dimension (0.5 mm). The opening in the cell further leads to an inner cavity of 1.5 mm diameter, which runs for a length of 12 mm before widening to a 3 mm bore of 25 mm length. The cavity is intercepted perpendicularly at the junction by a semi-cylindrical slot of 3 mm diameter for the target rod. The target is made to rotate and translate simultaneously using a mechanism driven by a stepper motor through a vacuum feed-through (see Fig. 3.5a and b). There is also an opening (1mm) opposite the slot, which allows the vaporization laser to be focussed on the target (see Fig 3.6a and b). All the openings on the cell have been lined with Teflon for better sealing.

The skimmer is made of nickel with a 1.5 mm orifice (Beam Dynamics, USA). The slit-skimmer assembly (see Fig 3.7) consists of an adjustable slit mounted on a stainless steel circular plate carrying an O-ring in order to facilitate differential pumping of the two chambers. The slit, skimmer and the sample cell are all mounted on a tripod stand as shown in the Fig. 3.7. This arrangement of the

nozzle-slit-skimmer assembly facilitates independent co-axial alignment of each of

the components in the assembly.

(a) (b)
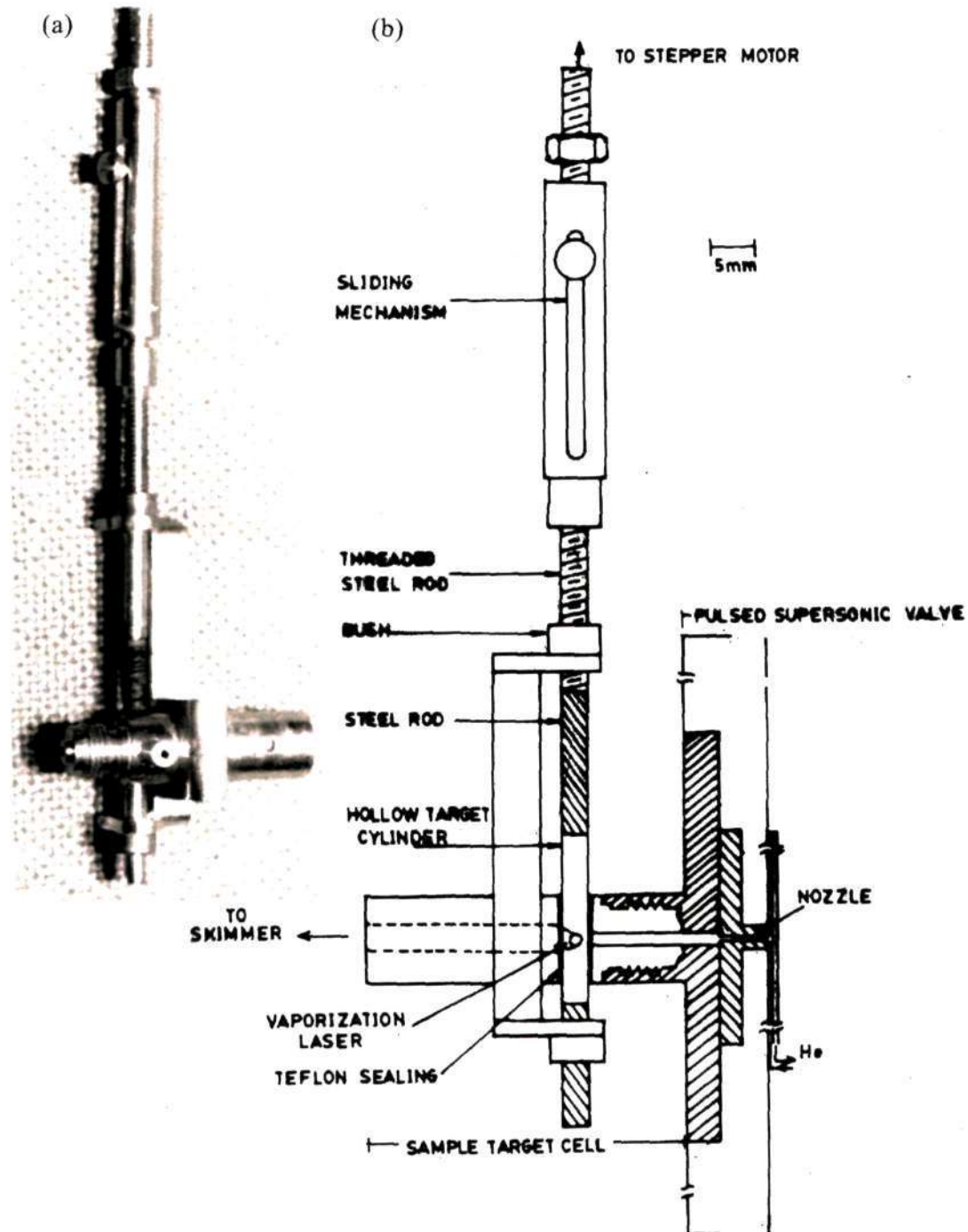
Fig. 3.5 (a) Photograph of the target mounting arrangement and the sample cell for solid targets (b) Schematic drawing of the solid cluster source. The sample target cut in the form of a cylinder is held pressed against the cell using a clamp. The vaporization laser produces a spiral groove by ablating the sample material as the target rotates and translates.

64

Fig. 3.6 (a) Photograph of the sample cell (b) The internal design of the sample cell.

Liquid samples were either fed directly into the pulsed valve, mixed with pressurized helium, or dropped in tiny amounts in front of the valve in vacuum under additional pumping. Routinely, a stainless steel vessel containing the

Fig. 3.7 Photograph of nozzle-slit-skimmer assembly mounted on a tripod stand.

desired liquid sample, was connected to the inlet of the pulsed valve at one end and to the helium cylinder at the other (see Fig. 3.2).

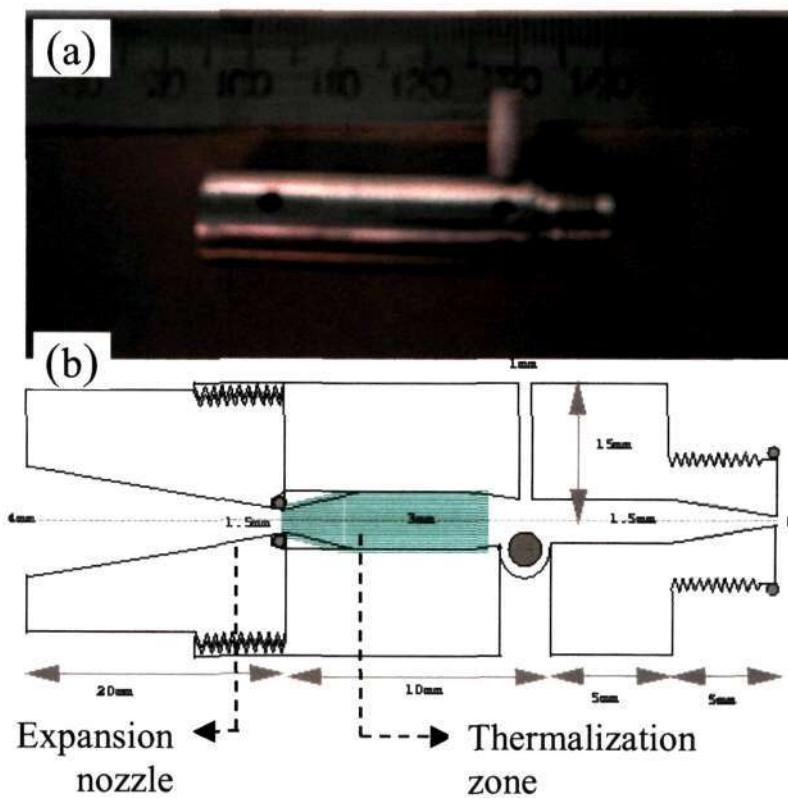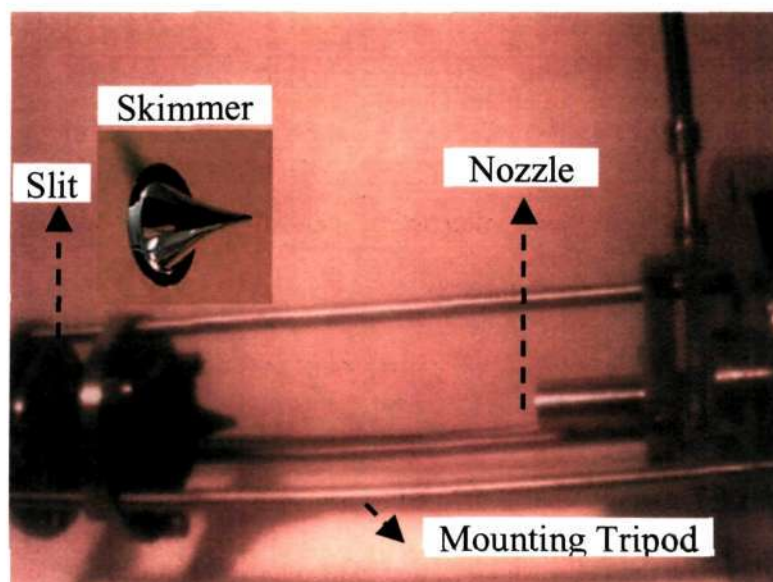Pulsed Nd-YAG lasers from Spectra Physics, USA (pulse width, 5-7 ns; frequency, 10 Hz) were used in the Q-switch mode for ablation and ionization. The 532 nm output of the vaporization laser operating at ~ 40 mJ/pulse is focussed onto a 1 mm spot on the target rod using a lens of 50 cm focus mounted on a x-y-z manipulator.

Time-of-flight mass spectrometer

The various internal components were fabricated with optimal geometry so as to fit into the different parts of the vacuum chambers. An extraction-acceleration grid assembly, a focussing assembly, a reflectron set-up and a detector form the essential components of the mass spectrometer. Ion optics simulation software (SIMION 3D, Version 6.0, D. A. Dahl) [17] was used to optimize on the location of the different components like the deflection-focussing assembly, grids in the ion-source region and the reflectron as well as the voltages on the above components. The extraction-acceleration grids, G_1 and G_2, are made up of Ni mesh (mesh-grid, 40 wires/cm; transmission, ~85%) laser-welded, in a local workshop, to circular steel rings of 9.2 cm outer diameter (inner diameter ~ 6.4 cm) (see Fig. 3.8).

Fig. 3.8 Photograph of typical grid consisting of fine Ni mesh laser welded on a circular steel rim.

The grids along with the repeller plate, G_0, are mounted parallel on a steel frame at desired spacing [18] using macor bushes. A spacing of 1.44 cm between the grids was chosen so that the ratio of the diameter and the spacing was ~ 4. The grid assembly is then mounted horizontally in the second chamber with the mid-point of G_0 and G_1 coinciding with the center of the chamber, which is also the focal point of the ionization laser (Fig. 3.2). Electrical connections are provided using vacuum feedthroughs.

The extraction-acceleration grid voltages were calculated using the first order focusing condition (equation (3.6)):

$$\partial T/\partial x_0 \rightarrow 0$$

where, T is the time of flight of the ion and x_0 is the point of ionization between G_0 and G_1 (Fig. 3.1). For $d_1 = d_2 = 1.44$ cm and L = 1.54 m and $x_0 = d_1/2 = 0.72$ cm, voltage values of 3000 and 1200 V were obtained for G_0 and G_1 respectively. G_2 was maintained at ground potential. Mass of a cluster ion was calculated using the equation, $T = c\sqrt{m}$, where T is the time of flight of the ion, m is the mass of the ion and c is a constant given by the equation,

$$c = (1/z)^{1/2}[\sqrt{(2*x_0/E_1)} + \sqrt{2}/E_2(\{E_1*x_0+E_2*d_2\}^{1/2} - (E_1*x_0)^{1/2}) + L/(\sqrt{2}(E_1*x_0 + E_2*d_2)^{1/2}]$$

$$..(3.8)$$

In equation (3.8), z is the charge on the ion and E_1 and E_2 are the electric fields in the extraction and acceleration region, respectively. A value of $c = 2.667$ $\mu s.u^{-1/2}$ was obtained from the experiment with 3000 and 1200 V applied on G_0 and G_1, respectively.

The focussing assembly consists of two pairs of rectangular deflection plates (3.77×7.99 cm^2) and an einzel lens (diameter, 4 cm), all made of stainless steel. These are rigidly fixed to a steel frame using macor spacers (see Fig. 3.9). The
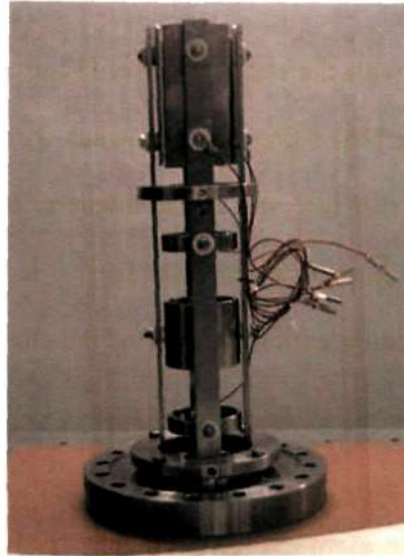
Fig. 3.9 Photograph of ion optics showing the four rectangular deflection plates and three circular rings acting as electrostatic lenses for focussing.

assembly is placed at the entrance of the flight tube. The einzel lens in the focussing assembly was given 1275 V with the deflection plates being held at small voltages of ~ 50 V.

The reflectron consists of a set of parallel grids, R_0 to R_5 (see Fig. 3.10), similar to the ones used in the ionization region. The grids are mounted at the end of the flight tube such that the normal at the center of the grids subtends an angle of 3.5° to the II axis of the flight-tube (see Fig. 3.2). A parabolic voltage pattern was applied to the reflectron grid assembly with R_0 held at ground potential, $V = ax^2$ where $a = 148.5$ V/cm^2 and x is the distance of a grid from R_0. Accordingly, voltages of 131, 524, 1181, 2100 and 3280 V were given to the grids R_1 to R_5, respectively. The retarding field, in the reflectron, narrows down the velocity distribution in an ion packet and deflects it towards the detector.

A microchannel plate detector (see Fig. 3.11) of 1.8 cm diameter (R. M. Jordan, USA) is placed symmetrically at the other end of the flight tube. The microchannel plate (MCP) detector consists of millions of tiny holes called microchannels where each acts like a channel electron multiplier.
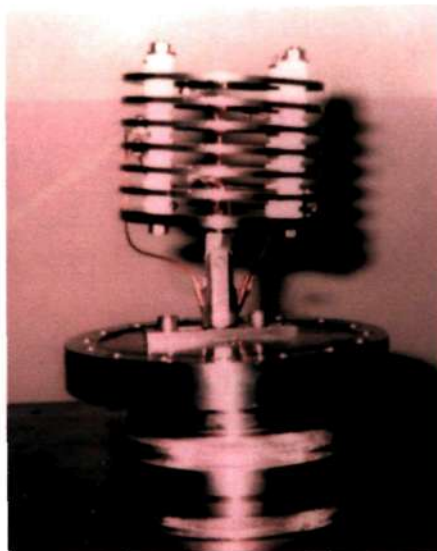
Fig. 3.10 Reflectron grid assembly consisting of six grids (R_0-R_5, R_0 is the topmost grid).

When a charged particle or photon is incident at the input of the channel, secondary electrons are generated and accelerated down the channel toward the output end. When these electrons strike the channel wall, additional secondary electrons are generated and this process continuously gets multiplied and the output signals are collected on an anode or phosphor screen. The microchannel plate detector was initially mounted at the end of the flight tube and the spectrometer was operated in the linear mode. The gain of the MCP detector is 1000. A voltage divider is used so as to maintain a constant ratio between the voltages applied to the three plates inside the detector.

In Fig. 3.12, a photograph of the fully assembled cluster apparatus with the R-TOF mass spectrometer is shown.

Fig. 3.11 Microchannel plate detector –18 mm (R. M. Jordan Company, CA, USA).

Fig. 3.12 A photograph of the fully assembled cluster apparatus with the R-TOF mass spectrometer.

3.3 System integration

The slit-skimmer assembly in the first chamber was aligned along the I-axis of the system (Fig. 3.2) using a He-Ne laser p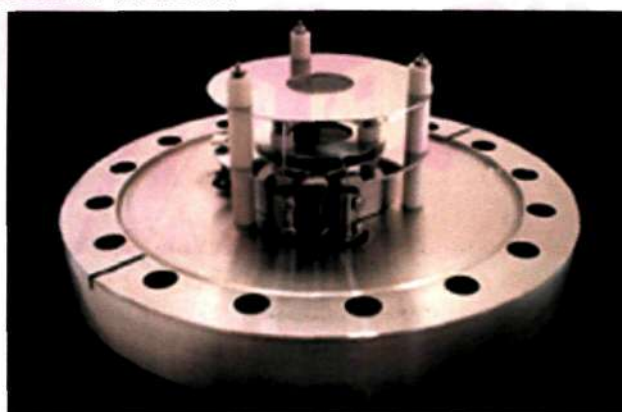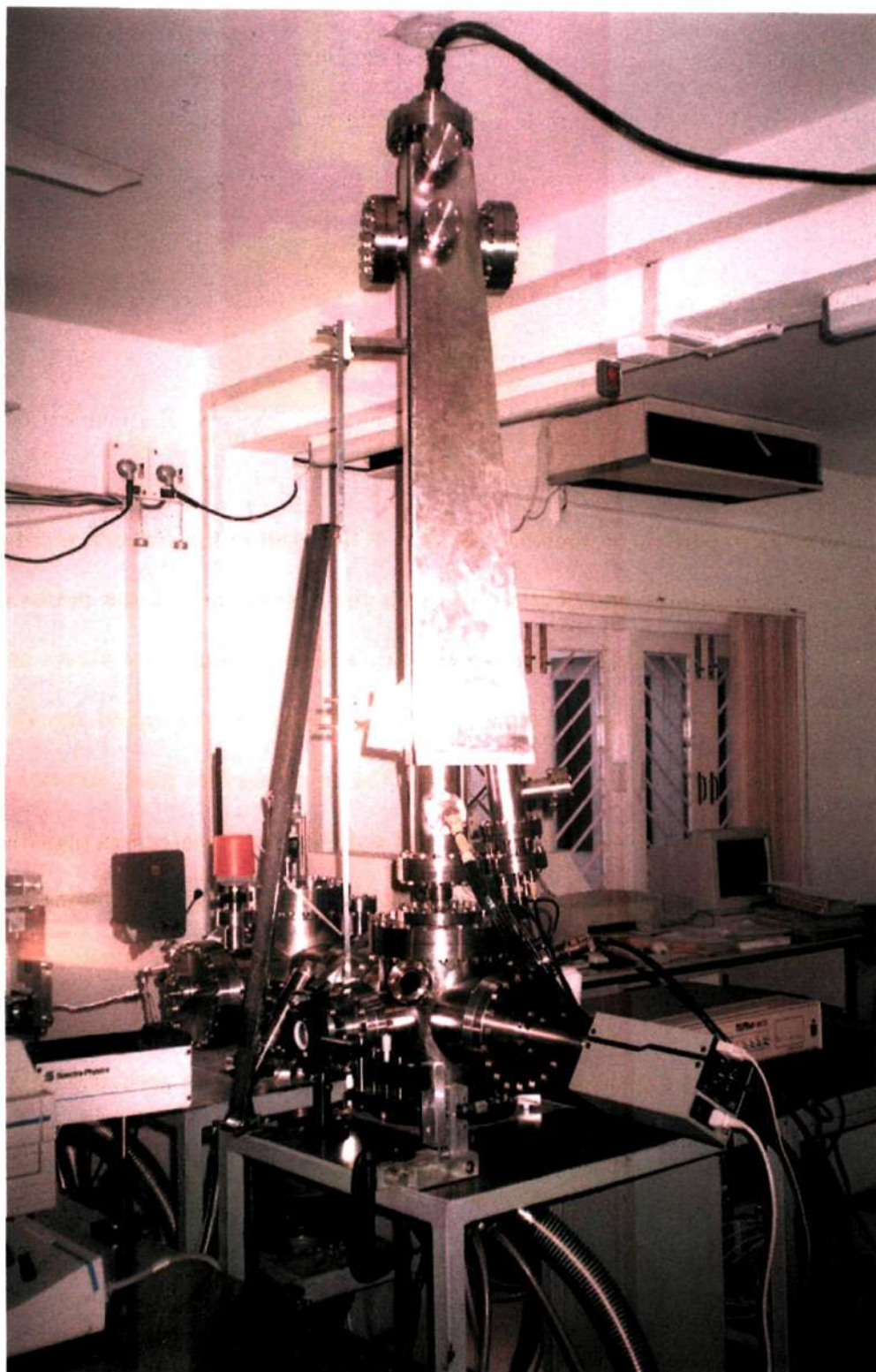ointer. The pulsed valve placed along the axis was operated at 10 Hz backed with 10 atmospheres pressure of a methanol-helium mixture. The mixture was produced by passing helium (99.999% pure) through a sample cell containing methanol (HPLC grade, Aldrich). The methanol species could be detected using the residual gas analyzer (RGA300, SRS, USA) placed in the ionization chamber along the same axis. The spatial alignment of the molecular beam with the ionization laser was done by introducing a steel rod in vacuum, which carried a perpendicular bore of 1 mm close to its tip. The rod was held perpendicular to the molecular beam such that the beam could pass through the bore. In this position, the laser was focussed at the tip of the rod.

3.4 Control electronics and signal recording

The pulsed valve and the ionization Q-switch were triggered externally at 10 Hz using a digital delay generator (EG&G, USA) having five output delay channels. Temporal synchronization of the ionization laser pulse with the molecular beam pulse (width ~ 100 μs) was achieved for a delay of ~ 400 μs. The beam velocity was indeed supersonic (~ 1.2×10^3 m/s). The vaporization, ionization laser and the multi-channel scalar (EG&G, USA) are appropriately triggered at different instances as shown in the schematic in Fig. 3.13. The multi-channel scaler (MCS) is a device that records the counting rate of events as a function of time. The smallest dwell time selectable per channel is 5 ns, scan length variable from 4 to 16, 384 channels and time scans ranging from 20 ns to 10^9 second can be selected. The output from the detector was fed to a fast timing preamplifier and then to the multi-

CONTROL ELECTRONICS
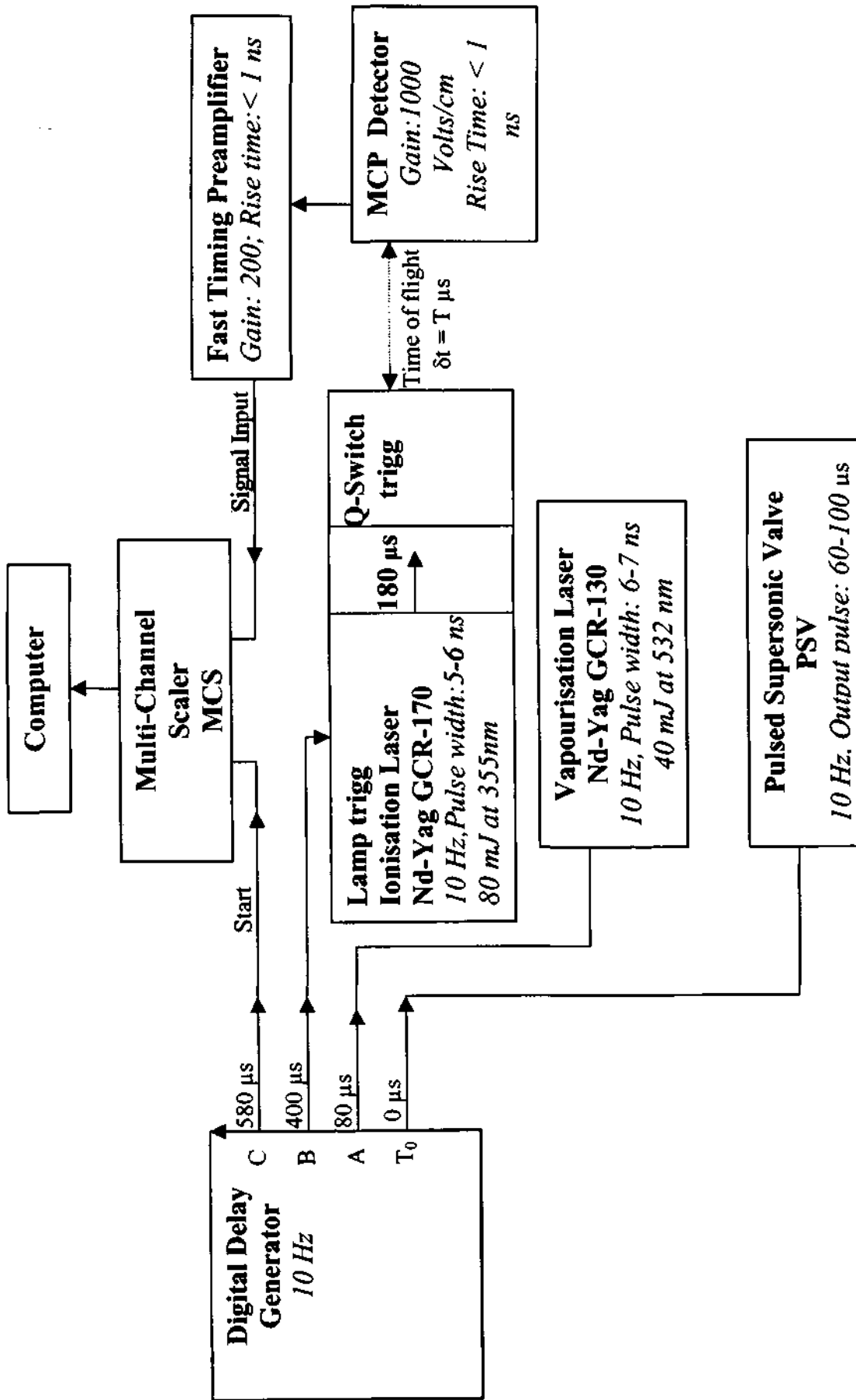
Fig. 3.13 Schematic drawing of the control electronics. Digital delay generator operating at 10 Hz triggers the pulsed supersonic valve with T_0 output. The flash-lamps of the vapourization and the ionization lasers and the start of the multichannel scaler are all triggered by the delay generator with delay pulses with respect to T_0, of A= 80, B= 400 and C= 580 μs, respectively. The microchannel plate detector output is amplified by a fast timing preamplifier, which is fed to the discriminator of the scalar. The data is stored and analyzed using a pentium computer

channel scaler connected to a personal computer for storage of data. The data can be displayed in the form of a spectrum using the TURBO-MCS software (EG&G ORTEC, USA). The time difference between the start signal to the MCS and the signal input from the detector gives the time-of-flight of the ion.

3.5 Performance and calibration

The TOF mass spectrometer operating in the linear mode was able to detect methanol clusters with a resolution of $R = T/2\Delta T \sim 800$, where ΔT is the full-width at half maximum of a mass peak. We observed that with the introduction of the reflectron, the resolution improved beyond 2500. In Fig. 3.14, we show a typical mass spectrum of methanol cluster beam obtained in the reflectron mode. The ionization potential of methanol is 10.85 ± 0.01 eV, slightly higher than the three photon energy at 355 nm. We, therefore, do not observe the methanol monomer (32 u) in the spectrum. The dimer (64 u) and the higher nuclearity clusters (96, 128, 160 u etc...) corresponding to potential drops of ~ 0.2 to 0.3 eV can be seen since three photon ionization becomes possible [19].

The spectrum in Fig. 3.14 shows protonated methanol cluster ions up to a nuclearity of 20 with populations tapering off around n = 11. The inset shows a full-width half maximum of 0.01 μs for the mass peak corresponding to the $(CH_3OH)_{11}H^+$ cluster. The protonated methanol peaks are believed to arise due to a rapid intracluster proton-transfer reaction following ionization of the neutral clusters [20]. From Fig. 3.14, we also see mass peaks (83, 115 u etc.) due to methanol clusters attached to a water molecule. It is interesting that water present as an impurity in extremely small amounts (~ 10 ppm) gives rise to such mixed clusters.
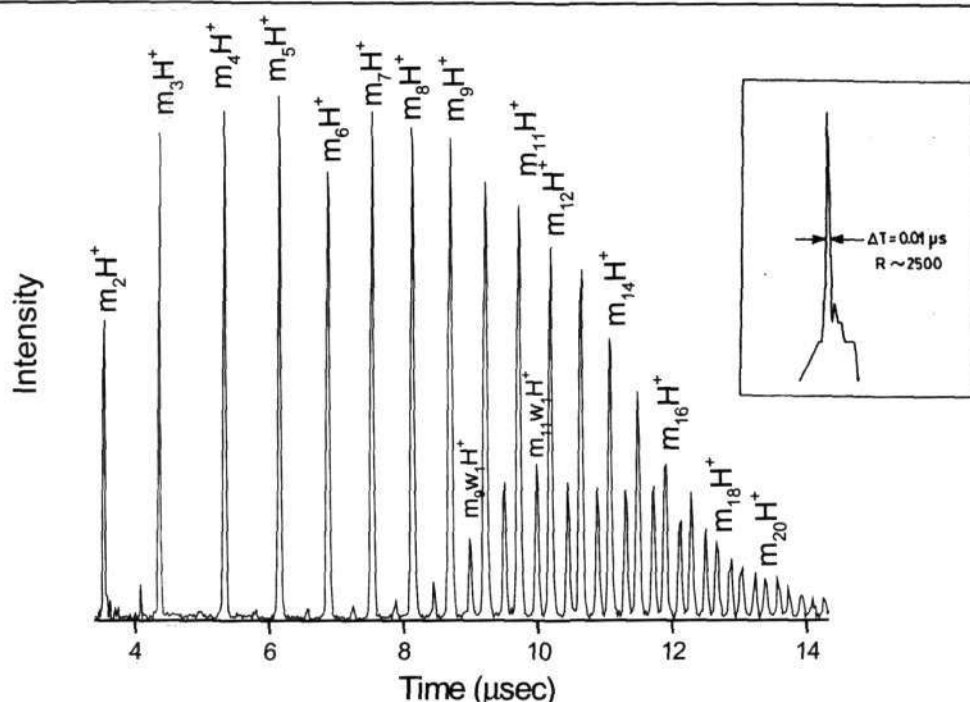
Fig. 3.14 Time-of-flight mass spectrum of methanol clusters obtained with our R-TOF mass spectrometer. The inset depicts typical resolution of the spectrometer. In addition to the $(CH_3OH)_nH^+$ peaks, small intermediate peaks corresponding to $(CH_3OH)_n(H_2O)H^+$ are also observed.

By using the solid sample cell, carbon clusters were obtained from a graphite rod. The pulsed valve was operated with helium at 10 atms and the vaporization laser pulse was delayed with respect to the helium pulse by 80 µs. The
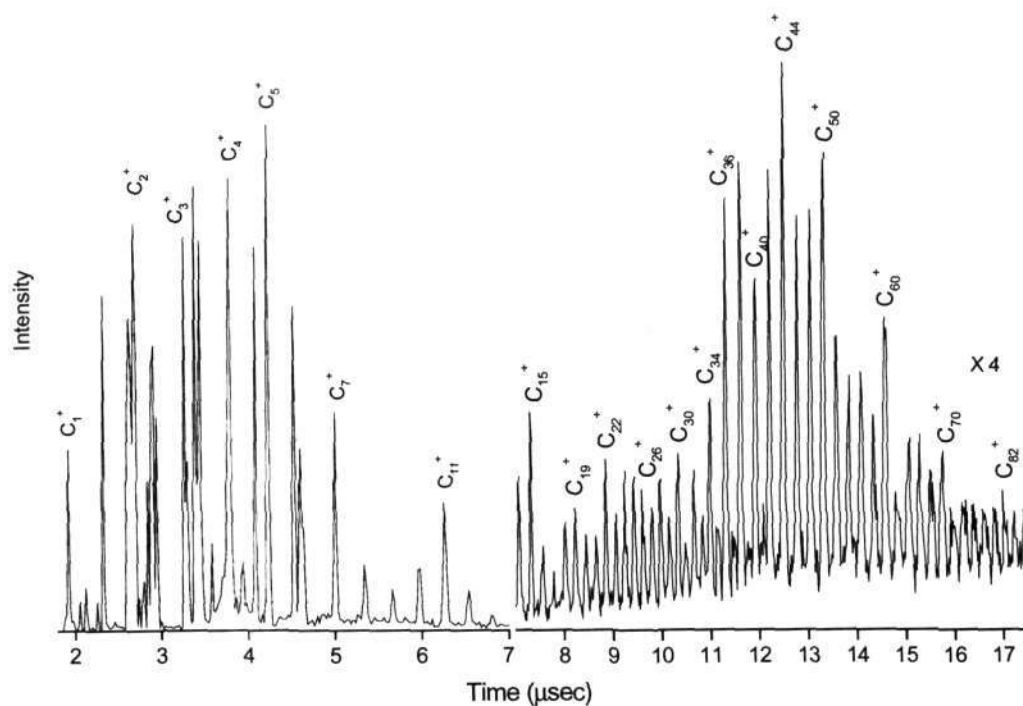
Fig. 3.15 Time-of-flight mass spectrum of graphite rod subjected to ablation using the 355 nm laser output. Carbon clusters upto a nuclearity of ~ 100 are detected.

graphite target was rotated at ~ 2 rpm. We were able to observe carbon clusters of nuclearity ~100 (1200 u) (see Fig. 3.15). Higher mass clusters can be obtained by fine-tuning of laser fluence to prevent multiphoton fragmentation [21].

3.6 Optimization of cell design

As mentioned before, the shape and the dimension of the waiting room, also called the thermalization zone, where the plume of the material mixes with the inert gas- is critical in controlling the size distribution of the clusters generated. Once the clusters are formed and thermalized in the waiting room, they move to the expansion nozzle where they undergo free supersonic expansion. It may be noted that a cell optimized for one set of conditions and a particular sample need not work the same way for another sample. Towards this, we made several attempts to improve the cluster size range by adopting different designs for the thermalization zone and the expansion nozzle. A few of the adopted sample cell designs and the corresponding mass spectra of carbon clusters, are shown in Fig. 3.16. It is clear that the shape and dimension of the expansion nozzle significantly affects the cluster size distribution.

3.7 Conclusions

A cluster source apparatus coupled to a reflectron time-of-flight mass spectrometer has been designed and fabricated. Different sample cells attached to pulsed supersonic valve have been developed to generate cluster beams from liquids and solid targets, the latter in conjunction with a vaporization laser. The mass spectrometer with a resolution of R ~ 2500 is capable of detecting masses of several thousand daltons. Ion optics simulation software SIMION was employed to optimize on the location of the various elements of the mass spectrometer.
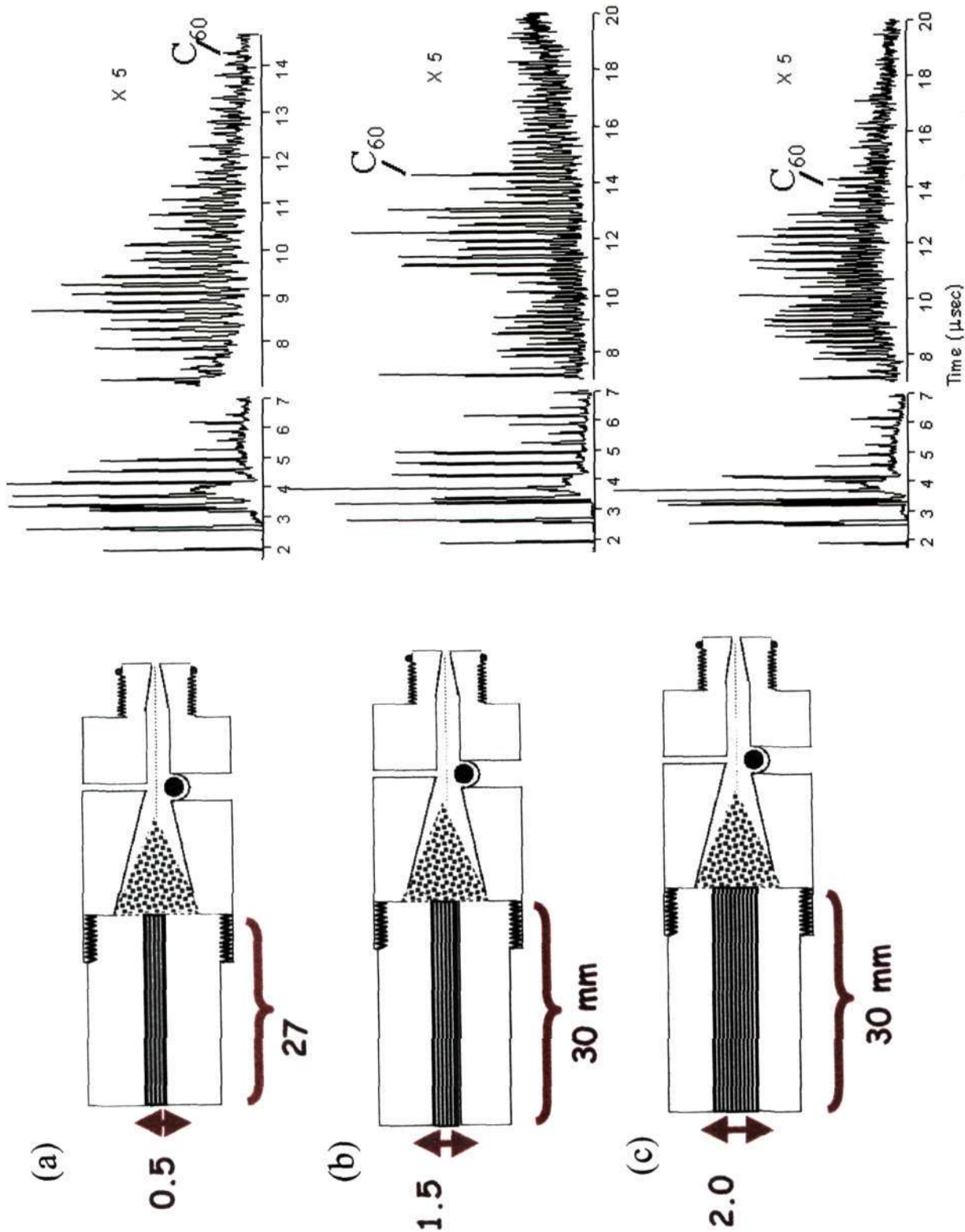
Fig. 3.16 Effect of change in sample cell design for solid targets. For different cell design (a), (b) and (c) are shown the corresponding mass spectra obtained for carbon clusters.

References

[1] G. Schmid 'Clusters and colloids, From Theory to Applications' VCH: Weinheim (1994).

[2] P. P. Edwards, R. L. Johnston and C. N. R. Rao In 'Metal Clusters in Chemistry' Edited by. P. Braunstein, G. Oro, P. R. Raithby, Wiley-VCH: New York (1999).

[3] G. Scoles 'Atomic and Molecular Beam Method, Vol. 1 & 2, Oxford University Press: New York (1988).

[4] H. Haberland 'Clusters of Atoms and Molecules' I &II, Springer-Verlag: Berlin (1994).

[5] S. C. O'Brien, Y. Liu, Q. Zhang, J. R. Heath, F. K. Tittel, R. F. Curl and R. E. Smalley, J. Chem. Phys. 84, 4074 (1986).

[6] J. J. Breen, W. B. Tzeng, R. G. Keesee, and A. W. Castleman Jr., J. Chem. Phys. 90, 11 (1988).

[7] E. Barborini, F. Siviero, S. Vinati, C. Lenardi, P. Piseri and P. Milani, Rev. Sci. Instrum., 73, 2060 (2002).

[8] M. Joseph, N. Sivakumar and C. K. Mathews, Bull. Mater. Sci. 17, 935 (1994).

[9] T. Sheuring and K. Weil, Surf. Science 156, 457 (1985).

[10] K. Sattler, J. Muhibach and E. Recknagel, Phys. Rev. Lett. 45, 821 (1980).

[11] J. B. Hopkins, P. R. R. Langridge-Smith, M. D. Morse and R. E. Smalley J. Chem. Phys. 78, 1627 (1983).

[12] B. A. Mamyrin, V. I. Karatev, D. V. Shmikk and V. A. Zagulin, Sov. Phys. JETP 37, 45 (1973).

[13] T. Bergmann, T. P. Martin and H. Schaber, Rev. Sci. Instrum. 60, 347 (1989).

[14] F. Hillenkamp, M. Karas, R. C. Beavis and B. T. Chait, Anal. Chem 63, 1193 (1991).

[15] M. L. Mandich, W. D. Reents, Jr. and V. E. Bondybey, In 'Atomic and Molecular Clusters' Edited. by E. R. Bernstein, Elsevier Science Publishers B. V.: Netherlands, 69 (1990).

[16] S. Maruyama, L. R. Anderson and R. E. Smalley Rev. Sci. Instrum. 61, 3686 (1990).

[17] D. A. Dahl, SIMION 3D, Version 6.0, User's Manual, Idaho National Engineering Laboraory, USA (1995).

[18] R. M. Jordan USA http://rmjordan.com/ttl.html.

[19] A. Holden 'The nature of solids' Columbia U. P.: New York (1965).

[20] M. T. Bowers, T. Su and V. G. Anicich *J. Chem. Phys.* 58, 5175 (1973).

[21] E. A. Rohlfing, D. M. Cox and A. Kaldor *J. Chem. Phys.* 81, 3322 (1984).

4. Alcohol-water clusters: Surface-enrichment in alcohol-water liquid mixtures*

SUMMARY

Molecular beams generated from the vapors above the surfaces of alcohol-water mixtures have been examined by time-of-flight mass spectrometry. The alcohols examined are methanol, ethanol, n-propanol and n-butanol. Neat clusters of water and alcohol as well as mixed alcohol-water clusters have been observed, the relative populations varying with the composition. The variation of the vapor phase mole fraction of the alcohol, estimated from the cluster populations in the molecular beam, with the liquid mole fraction, is found to be identical to that of the surface concentration of the alcohol in the liquid obtained from surface tension measurements. The results compare as well with those obtained from neutron reflection. The populations of the neat alcohol clusters, as distinct from those of alcohol-water clusters, also exhibit a similar trend. Surface-enrichment is considerably more pronounced in the case of n-butanol and n-propanol compared to ethanol. Thus, it is shown that the mass-spectrometric method of determining surface compositions of liquid mixtures is more direct, model-independent, and applicable over the entire range of compositions. However, methanol-water mixtures present a special case, owing to the lower surface enriching ability of methanol. In this case, our experiment rather reveals the non-ideal nature of the bulk mixture.

Similarly, the surfaces of ternary mixtures, water-methanol-ethanol, water-ethanol-1-propanol and water-methanol-1-propanol have also been examined. The enriching propensities in the ternary mixtures are compared with those in the binary mixtures. The net surface enrichment in ternary mixtures is generally lowered in comparison to that in the binary mixtures, except in the case of water-methanol-ethanol, where it is similar. While the surface enriching ability of methanol is nearly unaffected, that of ethanol is enhanced. The enriching ability of the longer chain propanol, however decreases significantly.

4.1 Introduction

It is well known that a fluid surface can cause the concentration of a component in a miscible mixture to be higher at the surface than in the bulk, a phenomenon commonly known as surface-enrichment [1]. The component with lower surface free energy tends to segregate to the surface to minimize the total free energy of the system. For a binary liquid mixture in contact with its vapor, each component may have its own concentration profile at the interfacial region depending on its volatility (see Fig. 4.1). This often results in a change in the surface tension of the solution relative to the pure components, the magnitude of the change depending on differences in the shape, size and the chemical nature of the molecules involved.
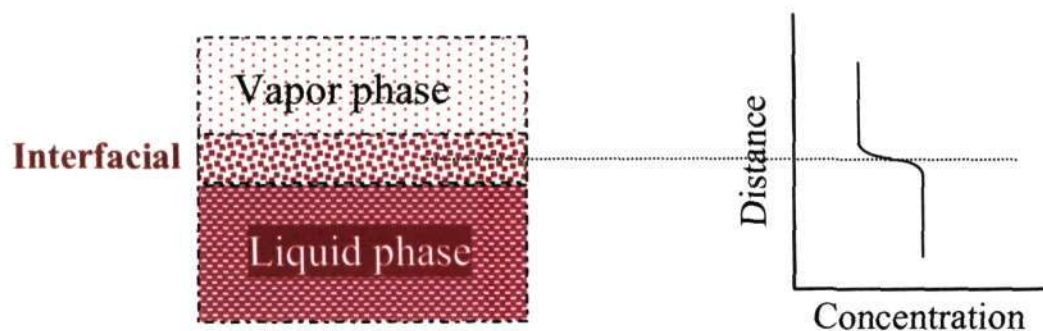
Fig. 4.1 Schematic illustration of the change in concentration going from vapor to liquid interface.

It is known that when an alcohol molecule is added to an aqueous solution, it has a tendency to segregate to the top. Interesting trends have been observed in the compositional dependence of surface tension in alcohol-water mixtures [2,3] (see Fig. 4.2) While methanol produces a gradual decrease of the surface tension of aqueous solutions with increase in concentration, ethanol and n-propanol produce more dramatic effects. Thus, in the case of n-propanol, the surface tension decreases

sharply as the alcohol concentration is increased up to a composition, beyond which it changes marginally.
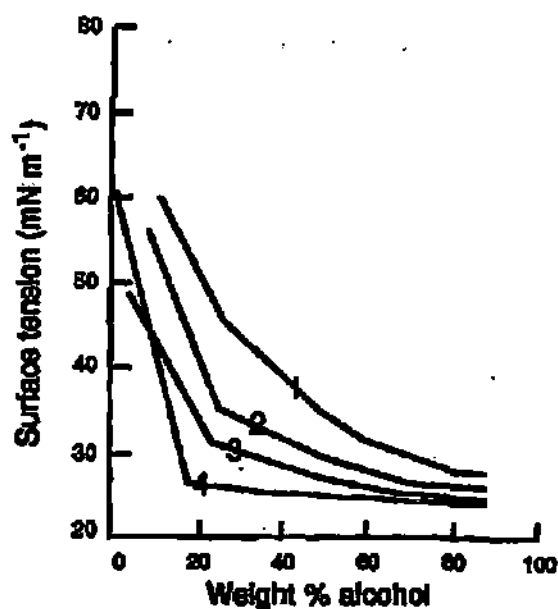
Fig. 4.2 Effect of short-chain alcohols on the surface tension of water: 1= Methanol, 2= Ethanol, 3= n-Propanol, and 4= n-Butanol [2].

The phenomenon of surface-enrichment by alcohol molecules in alcohol-water mixtures has intrigued many workers over the last few decades, much of the interest arising from the difficulty in predicting cluster nucleation rates from these liquid mixtures [4-9]. A useful relation from thermodynamics, which connects the surface excess concentration to the interfacial surface tension, is given by Gibbs adsorption equation, viz.

$$d\sigma = -RT\Gamma d\ln x\gamma \qquad (4.1)$$

where 'σ' is surface tension, 'Γ' is surface excess concentration of solute, 'x' is mole fraction of solute and 'γ' is the activity coefficient [10]. Schofield [11] and Guggenheim [4] employed the Gibbs adsorption equation and the knowledge of the partial molecular areas of ethanol and water at the surface to calculate the

surface mole fraction of ethanol as a function of the bulk mole fraction. More recently, Laaksonen [8] has taken the surface tension of the alcohol-water mixture, $\sigma(x_A)$, to be proportional to the surface tensions of the pure substances multiplied by their volume fractions in the surface layer as given by the equation,

$$\sigma(x_A) = \frac{(1 - x_A(s))v_W\sigma_W + x_A(s)v_A\sigma_A}{(1 - x_A(s))v_W + x_A(s)v_A} \qquad (4.2)$$

Here, x_A and $x_A(s)$ are the bulk and the surface mole fractions of the alcohol respectively, v_W and v_A are the partial molecular volumes of water and alcohol respectively while σ_W and σ_A are the values of the surface tension of pure water and alcohol. The above equation was fitted to the experimental values of surface tension, to obtain a relation between the surface and bulk mole fractions.

Quantitative estimations of the concentration profiles of surface-active liquid mixtures are indeed difficult, although there has been some effort in this direction in the case of polymer blends [12-14]. With regard to miscible alcohol-water mixtures, there is a report on the ethanol-water system based on neutron reflectivity measurements [15]. The surface excess of ethanol estimated from the neutron study compares well with the values obtained using surface tension data. The study, however, assumes different models for the distribution profiles of ethanol and water near the liquid surface.

In order to obtain direct experimental evidence for surface-enrichment, we have determined surface concentration profiles of binary alcohol-water mixtures over the entire compositional range by mass spectrometric analysis of the binary vapor in equilibrium with the liquid surface. For this purpose, we generated a

cluster beam of the binary vapor swept off the surface of the alcohol-water liquid mixture, by injecting it into vacuum through a pulsed supersonic valve.

4.2 Experimental

Mixtures of the alcohols (HPLC grade, Aldrich) and water (quartz-distilled) were prepared with varying molar composition over the entire range at ~ 0.1 intervals. In order to generate a molecular beam, 6 ml of the binary mixture was placed in a stainless steel cell connected to a pulsed supersonic valve (R.M. Jordan, USA) and was subjected to a helium backpressure of 2 atmospheres from the top (see schematic in Fig. 4.3). The alcohol-water vapor was injected into a vacuum of 10^{-7} torr through a 0.5mm orifice of the pulsed valve, operating at 10 Hz and 4000 A.

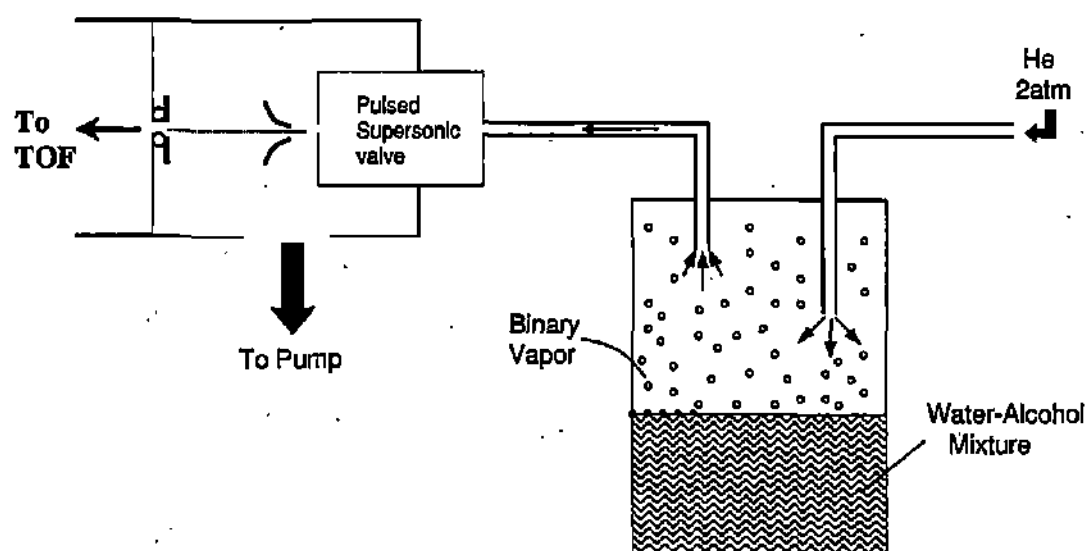Fig. 4.3 Schematic of the experimental set-up: He backpressure of 2 atm is applied on the water-alcohol mixture. The binary vapor produced is sampled through a pulsed supersonic valve and the cluster beam is analyzed using the time-of-flight (TOF) mass spectrometer.

For each binary mixture, the spectrum was collected under similar conditions after averaging the data in each channel over 5000 sweeps.

Measurements were repeated at a few molar compositions to ascertain the reproducibility in the experiments. In order to avoid residual contamination from a previous experiment, the pulse valve was pumped out each time before filling in the fresh vapor. Prior to each experiment, therefore, the pulsed valve and the associated electronics were allowed to stabilize for a few minutes. A computer code developed in the laboratory has been used to analyze the mass spectra in terms of the abundance and the internal compositions of the various cluster species.

4.3 Binary alcohol-water mixtures

Mass Spectra

Binary mixtures of the alcohols (HPLC grade, Aldrich) and water (quartz-distilled) were prepared with varying molar composition over the entire range at ~ 0.1 intervals. The mass spectra obtained at different compositions gave the nuclearity, population and composition of the various cluster species.

In Fig. 4.4, the TOF mass spectra of ethanol-water (E-W) mixtures corresponding to the liquid mole fractions of ethanol, x_E, of 0.1, 0.35 and 0.8 are shown. The mass spectra of the last two compositions are dominated by neat ethanol clusters (E_nH^+), mixed E-W clusters ($E_nW_mH^+$) being associated with much smaller intensities. The E_nH^+ clusters become prominent when $x_E > 0.2$, but their dominance persists even in the water-rich composition, as can be seen from Fig. 4.4c. Clusters of water and the mixed species with higher water attachments are seen in the mass spectra of the water-rich compositions.

Fig. 4.4 Time-of-flight mass spectra from ethanol-water mixtures for ethanol mole fraction in the liquid, x_E, of (a) 0.8, (b) 0.35 and (c) 0.1. The peaks are assigned to various protonated neat clusters of ethanol and water as well as mixed clusters.

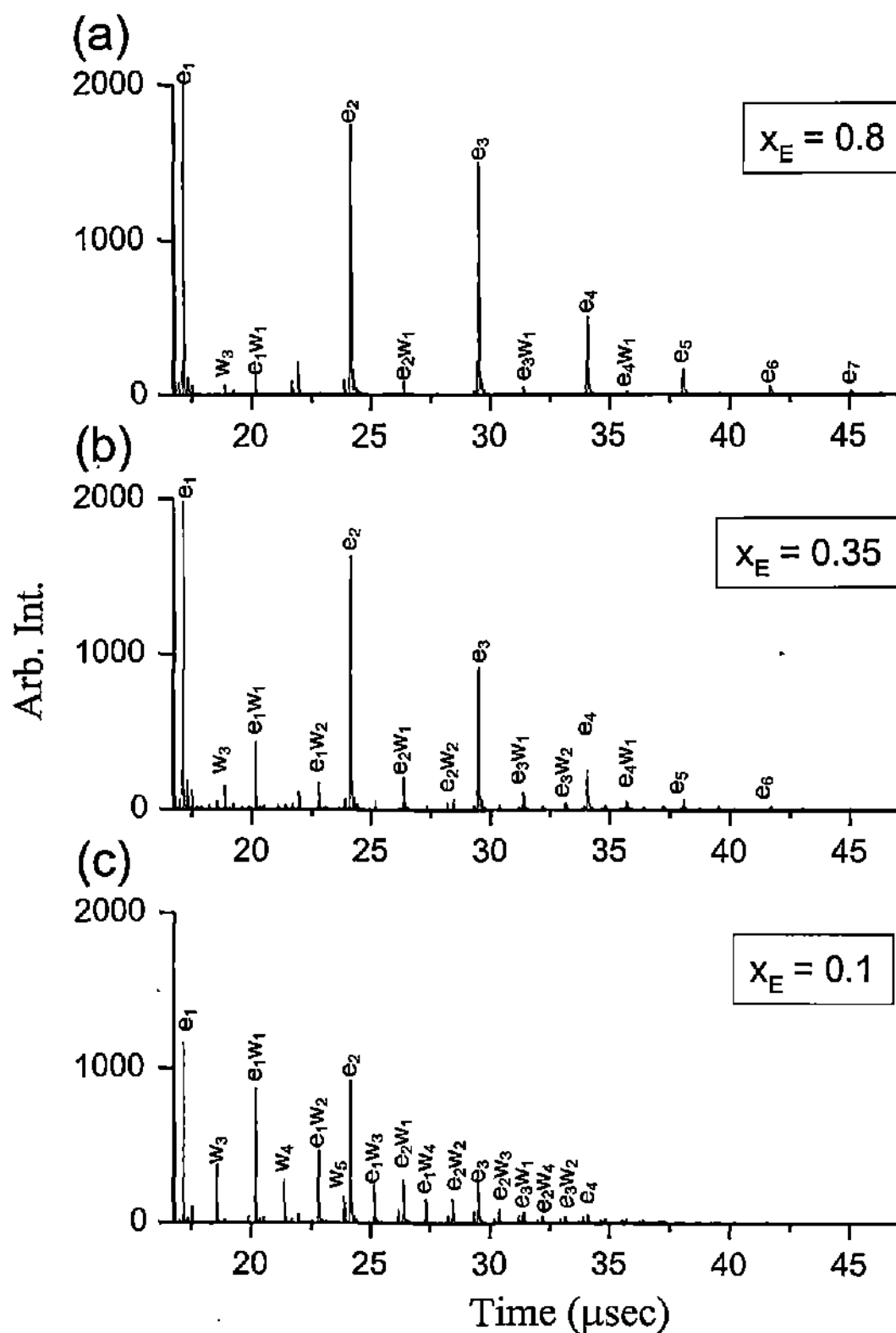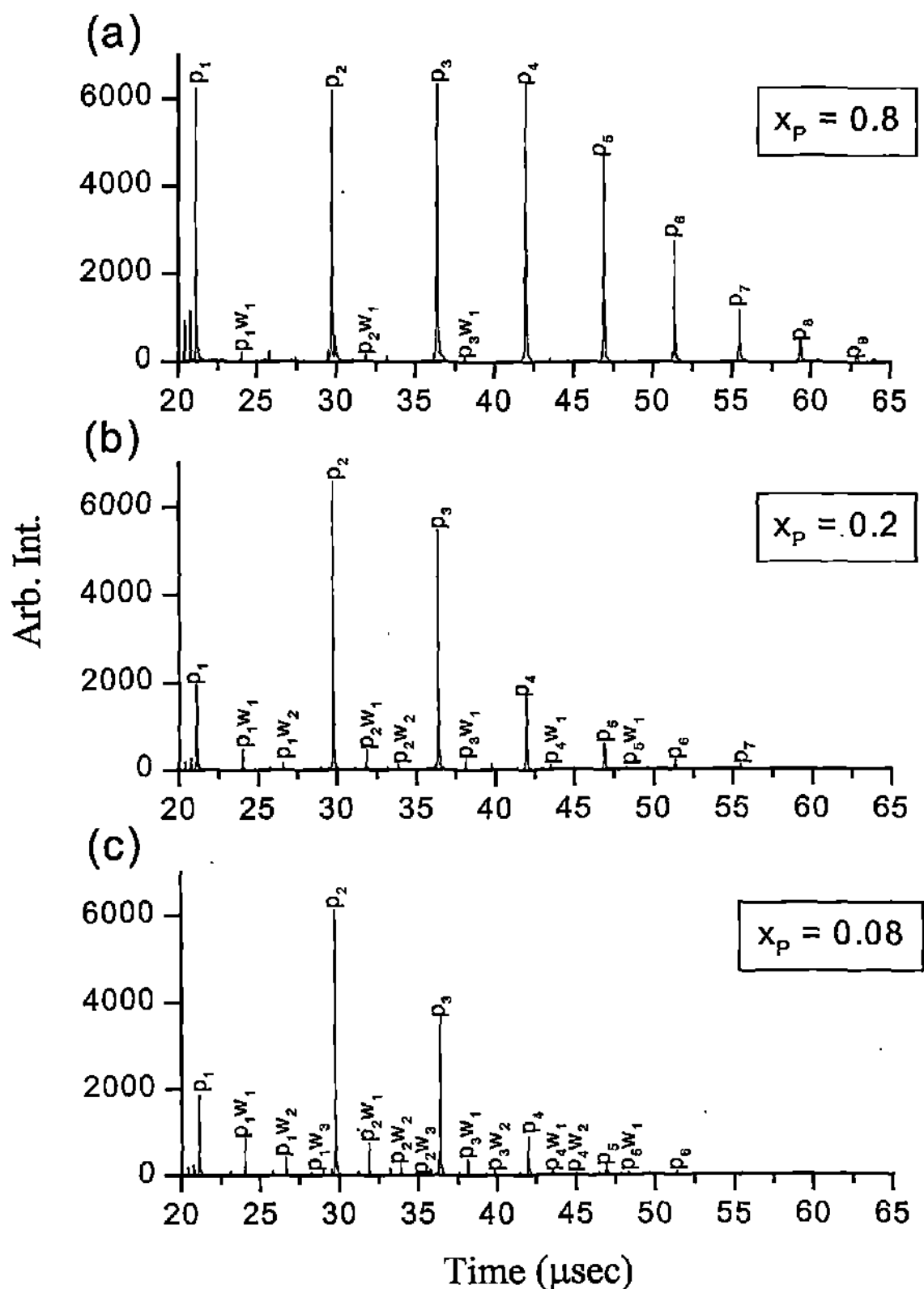**Fig. 4.5** Time-of-flight mass spectra from n-propanol-water mixtures for propanol mole fraction in the liquid, x_P, of (a) 0.8, (b) 0.2 and (c) 0.08. The peaks are assigned to various protonated neat clusters of propanol and water as well as mixed clusters. The relative increase in the signal strength compared to Fig. 4.4 is due to an additional set of deflection plates employed in the flight tube.

In Fig. 4.5, are shown the mass spectra from n-propanol-water (P-W) mixtures corresponding to the liquid mole fractions of propanol, x_P, of 0.08, 0.2 and 0.8. As in the case of ethanol, we observe that neat propanol clusters (P_nH^+) dominate the spectra at all the compositions. Mixed cluster species $(P_nW_mH^+)$ containing a few water molecules $(m \leq 3)$ are present only in water-rich compositions. Similarly, mass spectra for the n-butanol-water mixtures were also collected in the miscibility regime of about 2% of n-butanol in water.

Fig. 4.6 shows the TOF mass spectra obtained with water-methanol mixtures of liquid molar compositions (W:M) of 40:60 and 67:33. The spectra exhibit well-resolved peaks due to protonated neat clusters of water and methanol of different nuclearities $(W_nH^+$ and $M_mH^+)$ as well as those corresponding to various protonated mixed species $(W_nM_mH^+)$. Under the given experimental conditions, the 40:60 composition produces a cluster beam where M_m and W_1M_m clusters dominate (see Fig. 4.6a), the abundance of W_1M_m $(m>1)$ being nearly half of that of the corresponding M_m $(H^+$ omitted for brevity). The next prominent species are W_2M_m. Clusters with higher water attachments are, however, poor in intensity. For the 67:33 composition (Fig. 4.6b), we notice that the peaks due to the mixed species are relatively less intense. Peaks due to the neat methanol clusters dominate the mass spectrum, the maximum intensity being associated with the monomer. The intensity decreases gradually with higher nuclearity. Among the water clusters, only the monomer species carried an appreciable intensity.

Analysis and discussion

From the mass abundance of the various cluster species obtained from different molar composition alcohol-water liquid mixtures, we calculated values for

the vapor mole fraction of alcohol, y_A, by counting the number of alcohol molecules in the neat as well as the mixed cluster species.
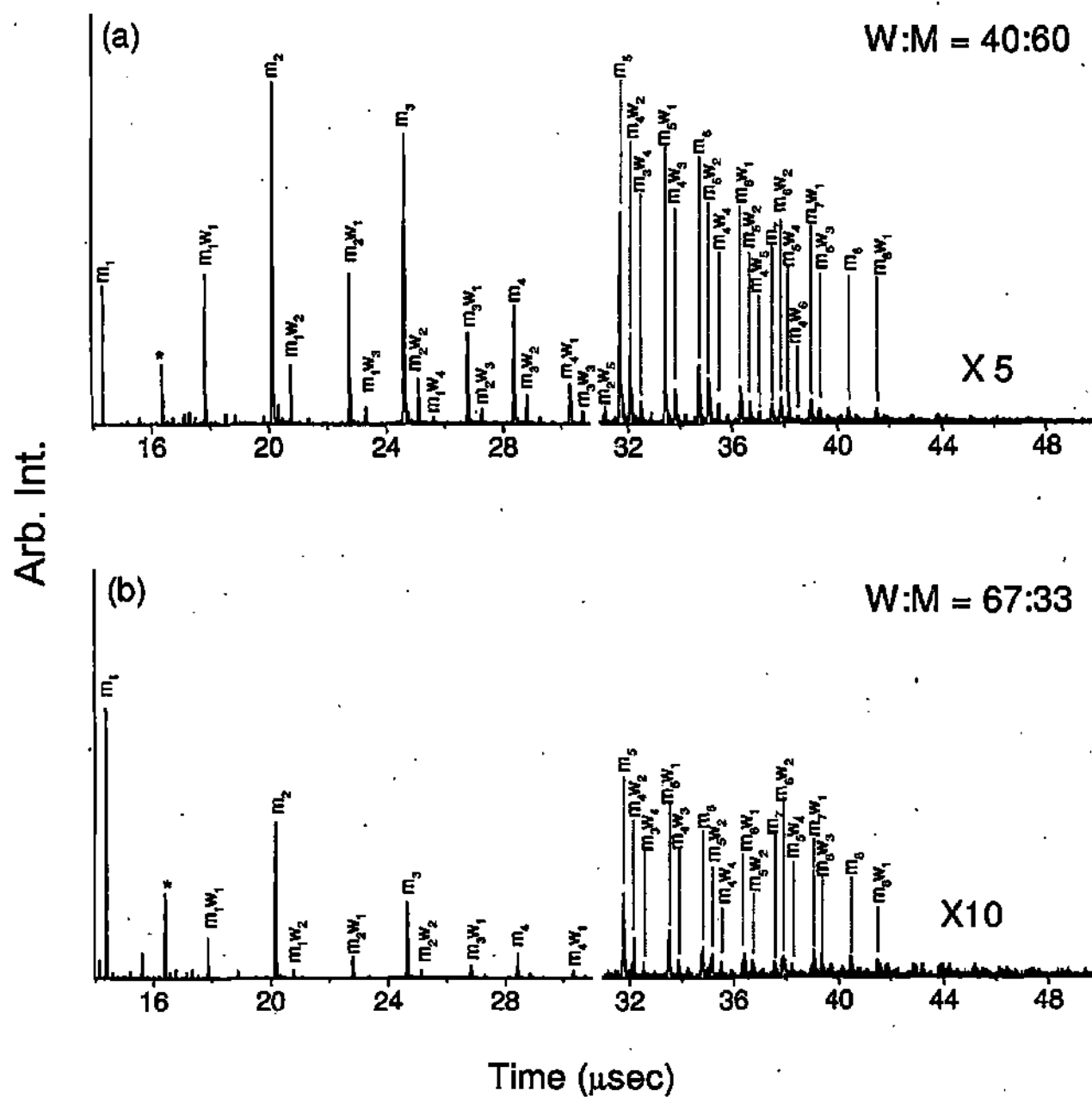
Fig. 4.6 Time-of-flight mass spectra of water-methanol clusters for liquid composition of (a) W:M = 40:60 and (b) W:M = 67:33. The peaks are assigned to various protonated W_nM_m clusters. For the sake of clarity, the peaks in the spectral range, 31 to 50 μs are magnified. Peaks from the ambient are shown by asterisk.

Thus,

$$y_A = \frac{\sum n}{\sum n + \sum m} \qquad (4.3)$$

where n and m correspond to the number of alcohol and water molecules in a cluster; the summations are over all the cluster species both neat and mixed. For the rest of the discussion below, y_A shall denote the vapor mole fraction of the alcohol and x_A that of the liquid mole fraction of alcohol.
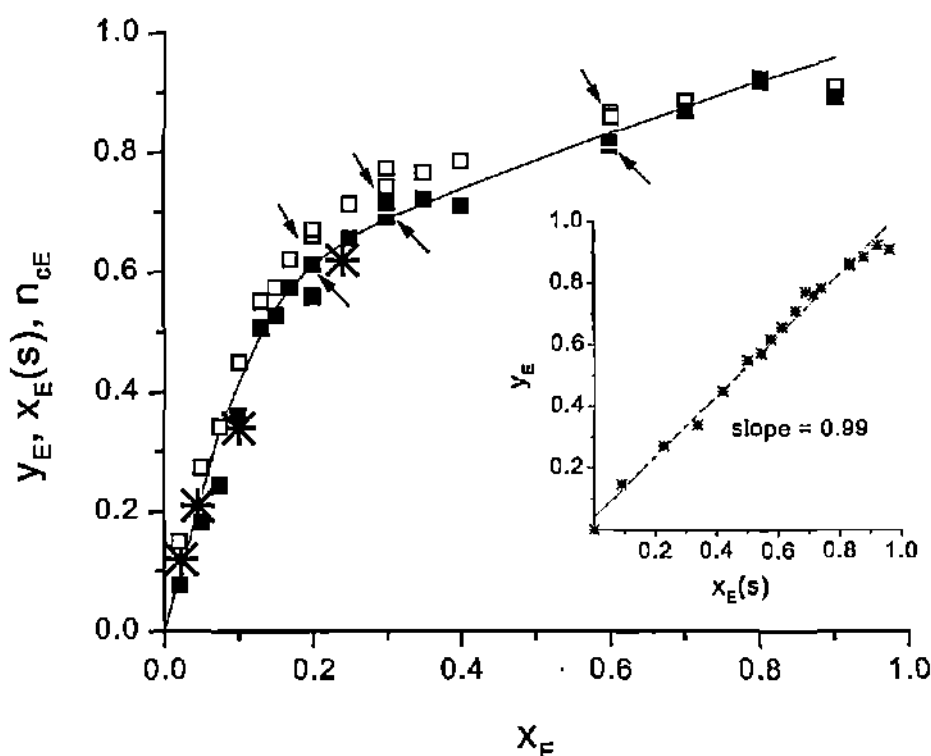
Fig. 4.7 Variation in the mole fraction of ethanol in the vapor, y_E (open squares) and the relative population of neat ethanol clusters, n_{cE} (filled squares) with the mole fraction of ethanol in liquid, x_E. The solid curve represents the surface mole fraction of ethanol, $x_E(s)$ taken from Ref. [8]. The neutron values are also shown (asterisk). Arrows indicate the repeat experiments. The inset shows the variation of y_E with $x_E(s)$.

In Fig. 4.7, the variation of y_E, with the liquid mole fraction of ethanol, x_E, in the ethanol-water mixtures is shown. The data points of the repeat experiments at x_E of 0.2, 0.3 and 0.6 provide an average estimate of the experimental error (± 0.02)

89

in y_E. The mole fraction of ethanol in the vapor increases sharply reaching a value of ~ 0.6 at $x_E \sim 0.2$, beyond which the increase in y_E is gradual. The variation of y_E with x_E in Fig. 4.7 is a clear reflection of surface-enrichment. In order to determine from this the surface-enrichment, we had to find a way to relate our results to the mole fraction of the alcohol on the surface '$x_A(s)$'. In order to achieve this, we compared our experimental results with those from surface tension and neutron diffraction data.

In order to compare our results quantitatively with those from surface tension and other measurements [11,15,16], we had to convert the surface excess values 'Γ' expressed as mol cm^{-2} in the literature to $x_E(s)$ values. Thus, in the case of neutron diffraction data for ethanol-water mixtures, the surface layer was taken to be 5.5 Å thick (approximate length 'l' of ethanol molecule [15,17]). The normalized surface excess values (per cm^3) is, then, given by Γ/l. The number of moles of ethanol per cm^3 at the surface due to the bulk concentration is given by

$$\frac{x_E}{x_W V_W + x_E V_E} \qquad (4.4)$$

where V_E and V_W stand for molar volumes of ethanol and water respectively. The number of moles per cm^3 of ethanol in the surface layer is obtained by adding the surface excess of ethanol per cm^3 to the bulk concentration. Thus, the total number of moles of ethanol/cm^3 at the surface is

$$\frac{\Gamma}{l} + \frac{x_E}{(x_W V_W + x_E V_E)} \qquad (4.5)$$

and the total number of moles of water/cm^3 at the surface is

$$\frac{x_W}{(x_W V_W + x_E V_E)} - \frac{\Gamma}{l} \qquad (4.6)$$

90

Therefore, the surface mole fraction of ethanol $x_E(s)$ is,

$$x_E(s) = \frac{\Gamma}{l}(x_W V_W + x_E V_E) + x_E \qquad (4.7)$$

We have plotted the values of surface concentration of ethanol, $x_E(s)$, reported by Laaksonen [8] against x_E in Fig. 4.7. Remarkably, it is seen that the variation of $x_E(s)$ with x_E is identical to that of y_E. Accordingly, the plot of y_E versus $x_E(s)$ is linear with a slope of unity as shown in the inset of Fig. 4.7. Thus, this justifies that the vapor from our experiment represents truly the surface of the liquid mixture. In Fig. 4.7, we have also shown the $x_E(s)$ values thus obtained from neutron data for compositions reported. As can be seen from the figure, the neutron values, once again, agree closely with our data. This, unequivocally, proves that the mass spectrometric analysis of the vapor in the cluster beam is a very accurate method of determining the surface compositional profiles for alcohol-water mixtures.

In Fig. 4.7, we have also shown the variation of the relative population of neat ethanol clusters, n_{cE}, with x_E. The variation of n_{cE} with x_E parallels that of y_E, indicating that the major contribution to the mole fraction of ethanol in the vapor phase comes from the neat clusters of the alcohol. Below $x_E \sim 0.2$, however, the difference between y_E and n_{cE} becomes large indicating the presence of several mixed species in this concentration regime. Our results are consistent with the observations of Matsumoto et al. [18] who found no clusters characteristic of the aqueous medium for $x_E \geq 0.2$, the dominant species being ethanol clusters and their hydrates. In Table 4.1, we list our results along with the values from surface tension, for the compositions where neutron results are also available. As can be seen from the Table 4.1, the surface mole fraction values of ethanol obtained from

our experiments agree well with the values obtained previously, especially for dilute solutions ($x_E < 0.1$).

Table 4.1
Surface mole fraction of ethanol from different methods

x_E	Based on surface tension			Neutron Reflection [15] $x_E(s)$	Our Expt. y_E
	Schofield [11] $x_E(s)$	Guggenheim [16] $x_E(s)$	Laaksonen [8] $x_E(s)$		
0.022	0.17	0.17	0.10	0.12	0.14
0.045	0.25	0.24	0.20	0.21	0.25
0.1	0.35	0.35	0.42	0.34	0.45
0.24	0.59	0.56	0.65	0.62	0.72

At $x_E = 0.1$, the surface mole fraction obtained by us matches closely that from Laaksonen calculations [8], but is slightly higher compared to the values from other sources [11,15,16]. For $x_E = 0.24$, the $x_E(s)$ value from our method seems to be slightly larger. It is noteworthy that the mass spectrometric technique employed by us enables the measurement of surface compositions over the entire range of x_E as shown in the Fig. 4.7. Unlike the neutron diffraction results, mass spectrometry is not model-dependent.

Figure 4.8 shows the variations of the experimental vapor mole fraction, y_P, and the surface mole fraction, $x_P(s)$, from the calculations of Laaksonen [8] with the liquid mole fraction, x_P. For $x_P \leq 0.1$, there is a steep rise in y_P to a value of ~ 0.85, the increase being rather gradual for $x_P \geq 0.1$. The agreement between the experimental vapor mole fractions, y_P, and the calculated values of $x_P(s)$ is excellent in this system as well. The plot y_P versus $x_P(s)$ is perfectly linear, with a slope of unity (see inset of Fig. 4.8). The variation in the population of neat propanol

clusters, n_{cP}, with x_P, mimics that of y_P, similar to the situation observed in the case of ethanol-water system.
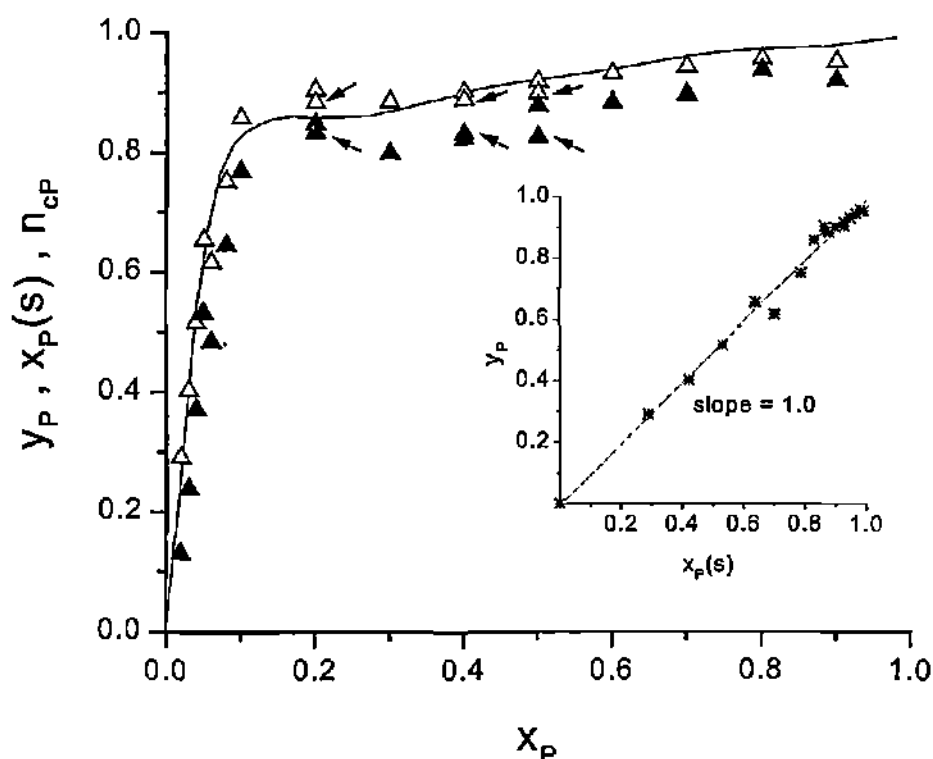
Fig. 4.8 Variation in the mole fraction of propanol in the vapor, y_P (open triangles) and the relative population of neat propanol clusters, n_{cP} (filled triangles) with mole fraction of propanol in liquid, x_P. The solid curve represents the surface mole fraction of propanol, $x_P(s)$ taken from Ref. [8]. Arrows indicate the repeat experiments. The inset shows the variation of y_P with $x_P(s)$.

Having established the reliability of the method to determine surface enrichment in miscible water-ethanol and water-n-propanol systems, we sought to examine the n-butanol-water system whose miscibility is only limited to a butanol mole fraction, x_B, of 0.02. In Fig. 4.9, we show the variation of y_B with x_B along with $x_B(s)$ values derived from surface tension data [19]. We are able to compare the present results with those from a neutron reflectivity study [19] performed in the miscible regime of this system (Fig. 4.9). The surface excess values from the neutron study were converted to $x_B(s)$ assuming the length of the n-butanol molecule to be 7 Å [19]. We notice from Fig. 4.9 that the y_B values lie close to the

$x_B(s)$ values from surface tension and neutron data, albeit the lower sensitivity of our method at very low alcohol concentrations. Unlike in other alcohols, the surface enrichment in the butanol-water system is reached at an extremely low concentration of the alcohol ($x_B \sim 0.0025$).
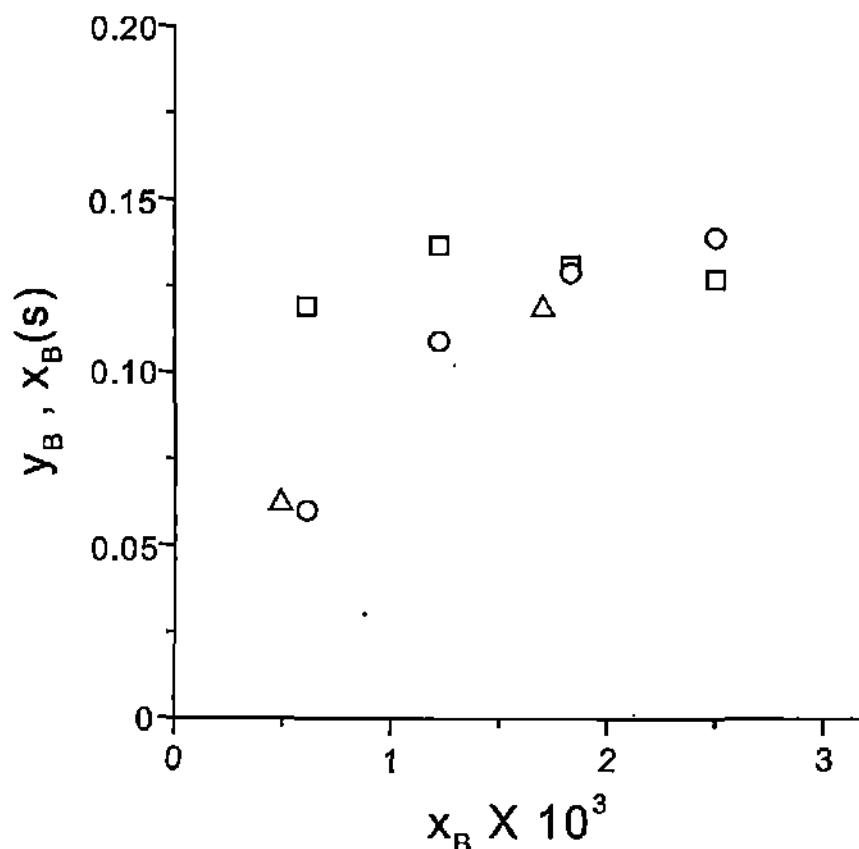
Fig. 4.9 Variation in the mole fraction of butanol in the vapor, y_B (squares) with mole fraction of butanol in liquid, x_B. Circles and triangles represent the surface mole fraction of butanol, $x_B(s)$, from surface tension and neutron data, respectively [19].

We have investigated the methanol-water system as well. Methanol being the smallest molecule in the series (~ 4 Å), one would expect a relatively poor surface-enrichment in the methanol-water system. The plot in Fig. 4.10 does indeed present such a scenario. Unlike in the case of higher alcohols, the mole fraction of methanol in the vapor, y_M, increases rather gradually with the increasing mole fraction of methanol, x_M, in the liquid. The agreement between our data and the Laaksonen's model is only moderately good. At low x_M, the experimental mole

fraction, y_M, is overestimated in comparison to the value of the surface mole fraction, $x_M(s)$ while at high x_M, y_M is somewhat underestimated. Neutron reflection data is, however, not available for this case.
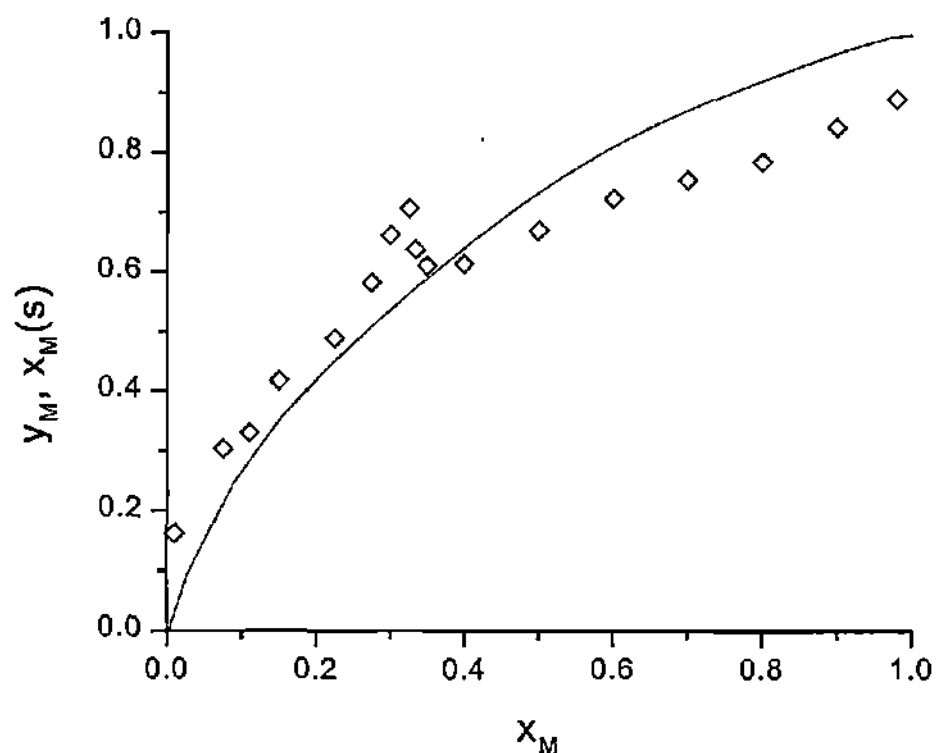
Fig. 4.10 Variation in the mole fraction of methanol in the vapor, y_M (diamonds) with mole fraction of methanol in liquid, x_M. The solid curve represents the surface mole fraction of methanol, $x_M(s)$ taken from Ref. [8].

The degree of surface enrichment in the different alcohol-water systems can be compared in terms of the initial slopes of the plots of the vapor mole fraction, y_A, against the liquid mole fraction, x_A (Figs. 4.7- 4.10). In Fig. 4.11, we show variation of the slopes with the number of methylene units in the alcohol. This is also evident from the inset in Fig. 4.11 where we show the variation of y_A with chain length for fixed values of x_A.
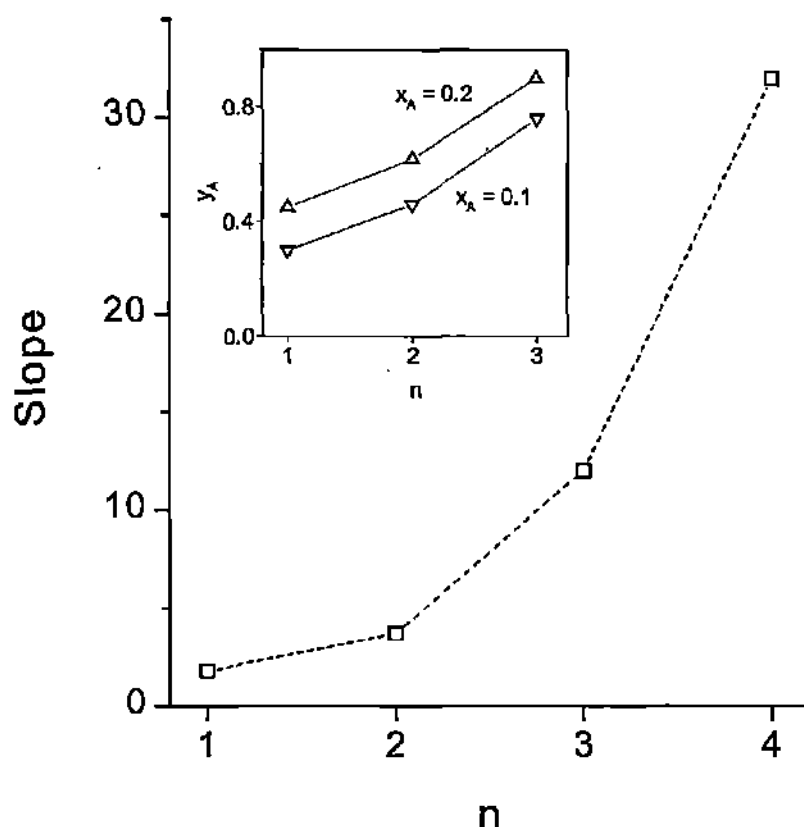
Fig. 4.11 Slopes of the plots of y_A versus x_A for the various alcohol-water systems against the number of carbon atoms in the alcohol molecule, n, in the low concentration regime prior to saturation of surface enrichment (squares). The inset shows the variation of y_A with n for $x_A = 0.1$ (down-triangles) and 0.2 (up-triangles).

Conclusions

In conclusion, we have demonstrated that the cluster-beam produced from the binary vapor in equilibrium with the surface of an alcohol-water mixture can be used to obtain composition profiles of the surface. The method faithfully reflects the surface concentrations in the alcohol-water mixtures. Neat alcohol clusters dominate the cluster beam right from the dilute regime, implying that the surface of the liquid is mainly made up of a stratum of alcohol molecules, perhaps a monolayer thick. With the increasing length of the alcohol molecule, the liquid surface is enriched at a faster rate. In the case of the higher alcohols, once the surface is enriched at high x_A, the surface composition hardly changes with the liquid composition (see Figs. 4.7 and 4.8). It is also interesting that as the length of the alcohol molecule

increases, the saturation of surface-enrichment occurs at progressively lower concentrations of the alcohol in the liquid mixture. Thus, the saturation occurs at x_A of ~ 0.3, 0.2, 0.1 and 0.0025 for methanol, ethanol, n-propanol and n-butanol systems respectively. Accordingly, the surface activity of an alcohol molecule in an aqueous mixture increases with the increasing length of its hydrocarbon chain, eventually leading to partial miscible mixtures forming two-layers.

4.4 The Special case of methanol-water mixture

As shown in Fig. 4.10, the vapor mole fraction of methanol from methanol-water liquid mixtures has only moderate agreement with the surface mole fraction of alcohol from Laaksonen's surface data. This is on account of the lower surface-enriching ability of methanol. Hence, we considered it important to examine the binary vapor from water-methanol liquid mixture in order to throw more light on the issue of molecular interactions in it.

Non-ideal binary liquid mixtures exhibit diverse properties depending on the relative strengths of the homo- and the hetero-interactions between the component molecules. When the strengths are equal, the mixture forms an ideal solution and follows the Raoult's law. Deviations from the Raoult's law are seen in the asymmetric variations with composition of the thermodynamic functions [20,21] like excess enthalpy, entropy, free energy of mixing or partial molar volumes. Thus, a non-ideal liquid associated with a negative heat of mixing and volume contraction would contain molecules where hetero-interactions are stronger than the homo-interactions [22]. The water-methanol mixture is a typical non-ideal system, characterized by a minimum in the excess enthalpy of mixing (H^E ~900 Jmol^{-1}) at a water mole fraction of ~0.7 [23]. A widely accepted notion is that molecular

association [24] in water-alcohol media occurs mainly via hydrogen bonding, although hydrophobic forces also play a role in the liquid structure. It is of great interest to relate the thermodynamic behavior of the system with the nature of the interactions between the component molecules in the liquid. Toward this end, there have been many studies on water-methanol mixtures based on mass spectrometry. Clusters of the type, $(CH_3OH)_m(H_2O)_nH^+$ produced from mixed vapors of water and methanol have been examined by Kebarle et al. [25] and Stace et al. [26] who found that methanol is taken up preferentially in small clusters. Another class of experiments [27-29] pertains to cluster beams generated by the adiabatic expansion of liquid jets of water-alcohol mixtures. Nishi et al. [27] studied the relative stability of monomer and dimer hydrates of methanol as well as other organic molecules. Wakisaka et al. [28] found that alcohol molecules have substitutional interaction with the water clusters. More recently, Takamuku et al. [29] have performed a detailed analysis of the structure of water-methanol clusters using mass spectrometry and X-ray diffraction and proposed that the chain-like clusters present in methanol-rich mixtures give way to tetrahedral species when water content increases from 0.3 to 0.7.

Analysis and Discussion

Before discussing the observed trends in the cluster abundance, we show in Fig. 4.12 the variations in the mole fractions of water and methanol constituting the entire cluster beam.
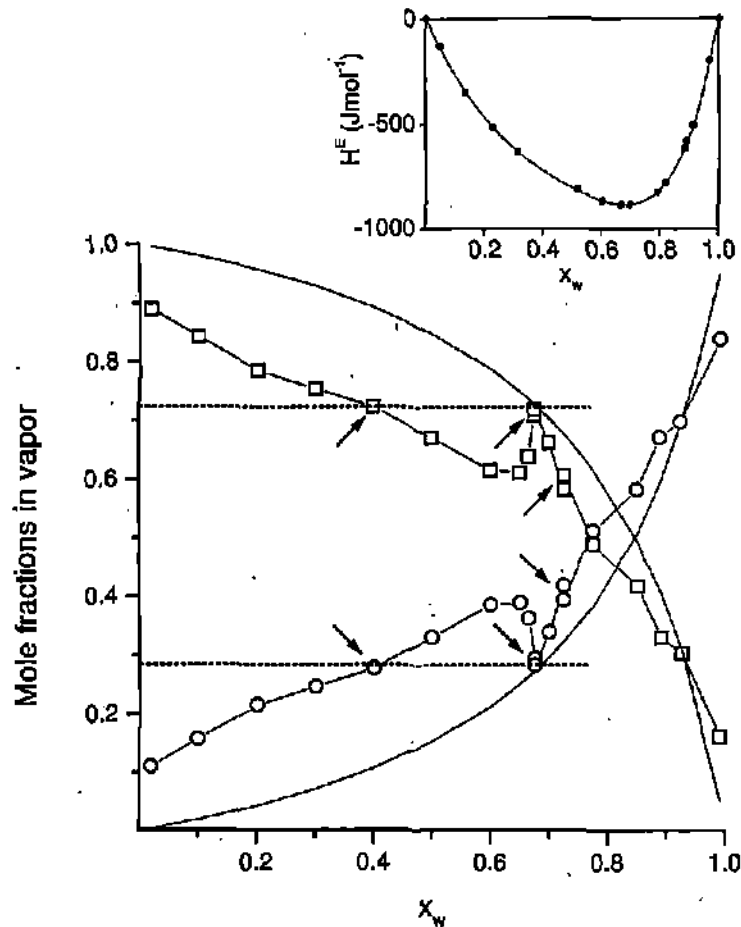
Fig. 4.12 Variations in the mole fractions of the water and methanol in the vapor with x_w, methanol, squares; water, circles. The experimental values (open symbols) are obtained from the populations of the clusters in the molecular beam. Calculated mole fractions assuming ideality of the mixture are shown by solid curves. The arrows indicate the repeat measurements for three mixtures. The dashed line passes through equal experimental mole fraction points. The inset shows the variation of excess enthalpy of mixing with x_w (from Ref. 28).

These experimental values have been compared with the calculated vapor compositions, assuming water-methanol mixture to be ideal. The latter were obtained using the formula [30],

$$y_w = (x_w * p^*_w)/(p^*_m + (p^*_w - p^*_m)*x_w) \qquad (4.8)$$

where y_w and x_w are the mole fractions of water in the vapor and the liquid states respectively and p^*_m and p^*_w are the vapor pressures of the corresponding pure

liquids at 2 atmosphere pressure (methanol, 17.5 kPa; water, 3.2 kPa at 25°C). Several interesting observations can be made from Fig. 4.12.

Mixtures containing small quantities of water ($x_w \leq 0.1$) produce molecular beams in which the total water present is quite significant (~ 0.1 to 0.2). The situation is just the opposite with methanol. The methanol fraction in the vapor is 0.9 at $x_w = 0.02$ and reduces to around 0.6 when $x_w = 0.6$ and the variation is gradual. In the range, x_w ~ 0.6 - 0.75, the mole fraction of methanol passes through a sharp rise while water follows the opposite trend. More importantly, the experimental mole fraction curves in Fig. 4.12 touch the calculated curves at $x_w = 0.67$. Beyond $x_w = 0.75$, the mole fractions regain the gradual variation and remain rather close to the ideal values. The variation in the mole fraction of each component can, therefore, be considered as arising due to the superposition of two trends, namely a sharp feature at $x_w = 0.67$ standing on a more gradual variation across the rest of the composition range.

The above experimental observations led us to infer the following. In the liquid composition range, $0 < x_w \leq 0.6$, the fraction of water in the vapor is more and that of methanol is less compared to the values from "the ideal" mixture. In other words, methanol exhibits a promotional effect on water vaporization simply reflective of the interaction between the component molecules in the non-ideal liquid. The analysis of the mixed cluster species is expected to throw more light on this. When x_w increases from 0.6 to 0.75, the vapor composition goes through a rather sharp variation, even matching the "ideal" at x_w ~0.67. Surprisingly, this liquid composition corresponds to the minimum in the excess enthalpy of water-methanol system [28] (see inset of Fig. 4.12) and could have immense influence on the vapor composition. In addition we infer from Figs. 4.6 and 4.12 that, although

the experimental vapor compositions for the 40:60 and 67:33 liquid mixtures are almost equal (~ water content of 0.3, see dashed lines in Fig. 4.12), the cluster distribution is noticeably different in the two cases (Fig. 4.6). The diverse nature of the cluster beams could not have originated entirely by the method employed for vapor injection alone. A stagnation pressure of 2 atmospheres He and an orifice of 0.5 mm optimally opened using current pulses of 4000 A (maximum rated 5000 A) is indeed considered to be a weak clustering condition. Moreover the experimental conditions being the same throughout, the clustering induced by the pulse valve, if any, should be similar for all the vapor mixtures or at best may vary gradually with vapor composition. Our experimental observations, thus, allow us to deduce that the vapor arising from a water-methanol mixture possesses an intrinsic structure imparted by the liquid.

The variations in the cluster populations are shown in Fig. 4.13. The relative populations of the W_n, M_m and mixed cluster species were obtained as fractions of the total cluster population. As shown in Fig. 4.13a, the population of the neat methanol clusters decreases steadily from 0.9 at $x_w = 0.02$ to 0.4 at $x_w = 0.6$ with a small change of slope around $x_w = 0.3$. It exhibits a sharp feature at $x_w = 0.67$, decreasing steeply thereafter. When methanol is rich in the liquid mixture, higher nuclearity methanol clusters, M_3, M_4 and M_5, dominate among the neat methanol clusters as shown in the inset of Fig. 4.13a for the 20:80 mixture (curve A). At 50:50 composition, M_2 is more abundant (curve B) and on further decrease of methanol in the mixture (89:11), the methanol monomer, M_1, predominates over the higher nuclearity methanol clusters (curve C). It may be recalled from Fig. 4.6b that the monomeric methanol species are relatively more abundant in the cluster beam at $x_w = 0.67$. Thus, it is clear that the preference for higher nuclearity methanol clusters decreases as the methanol content in the liquid mixture is reduced and the
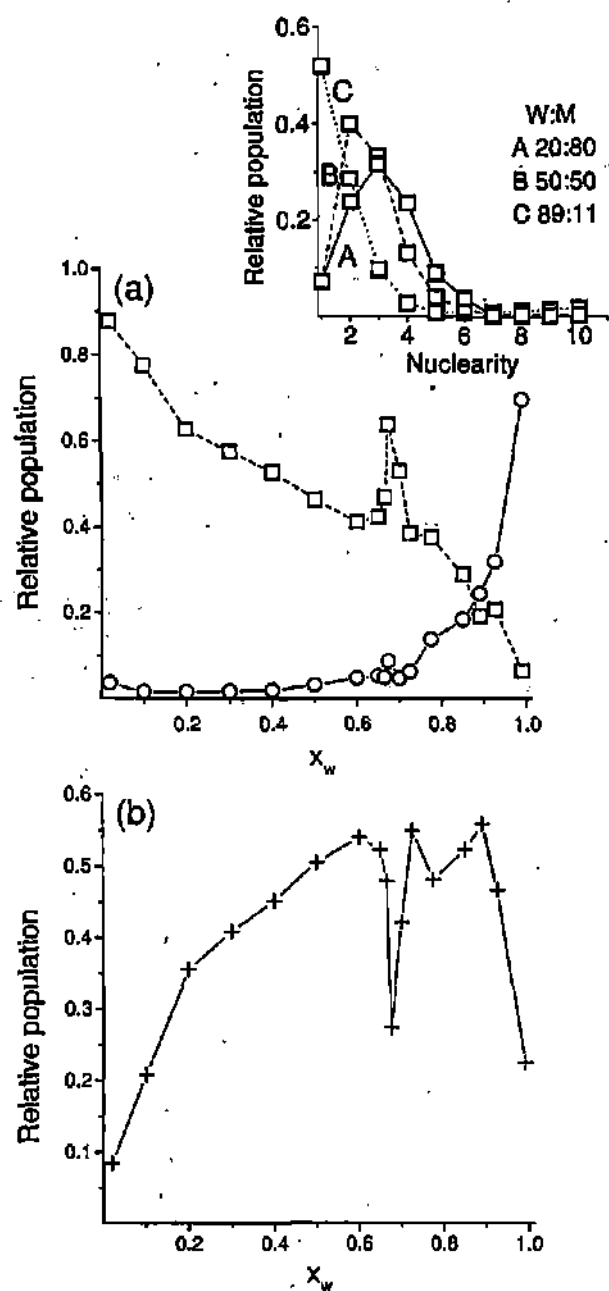
Fig. 4.13 (a) Variation in the relative population of neat clusters as function of x_w is shown; methanol, squares; water, circles. The inset shows the variation in the relative populations of neat methanol clusters with nuclearity, n, for different compositions of the liquid mixtures, namely, W:M = 20:80, 50:50 and 89:11.(b) Variation in the relative population of the mixed clusters as a function of x_w.

cluster population decays gradually with nuclearity [31]. As regards the neat water clusters, their population is rather low till $x_w = 0.6$ and increases sharply beyond $x_w = 0.8$ following a small kink at $x_w = 0.67$ (see Fig. 4.13a). Higher nuclearity water clusters are seen from compositions rich in water ($x_w > 0.9$). The relative abundance

of the mixed cluster species (Fig. 4.13b) shows a steady rise till $x_w = 0.6$ where the mixed clusters constitute 55% of the cluster beam. The population drops suddenly around $x_w = 0.67$. The variation of the mixed species is, obviously, complementary to that of neat methanol clusters for $x_w < 0.75$.

A detailed examination of the various mixed cluster species has shown that the populations of the water-rich clusters increase and those of the methanol-rich clusters decrease with x_w. The overall intensity of a cluster species is high if the methanol content in it is more relative to the water content. In the given experimental conditions, the intensities of the higher nuclearity clusters (n>7) are smaller as expected. Clusters containing equal number of water and methanol molecules show a broad distribution centered around $x_w = 0.6$ often with a small dip at $x_w = 0.67$. Indeed, all mixed cluster species showed sharp variations near $x_w = 0.67$, the magnitude being larger for water-rich clusters. As examples of mixed cluster analysis we show in Fig. 4.14, the populations of $W_n M_m$ with total nuclearities of 4, 5 and 6, against x_w.

The water-methanol system is enthalpy driven and therefore, clustering of molecules in the liquid involving hetero-interactions is energetically favored [22]. Clearly, the deviation from ideality in Fig. 4.12 arises due to the imbalance in the hetero- and homo-interactions between the component molecules in the liquid. The mixed cluster population in the vapor could, therefore, be a representative of this deviation. We have examined this aspect by plotting the relative population of mixed clusters against Δ in Fig. 4.15, where Δ is the difference between the experimental mole fractions and those obtained assuming ideality. We identify four regimes in the plot with respect to x_w. In regime I ($0 < x_w < 0.3$), the fraction of mixed clusters is proportional to Δ or in other words, goes hand in hand with the increasing imbalance between the homo-hetero interactions in the liquid. In regime
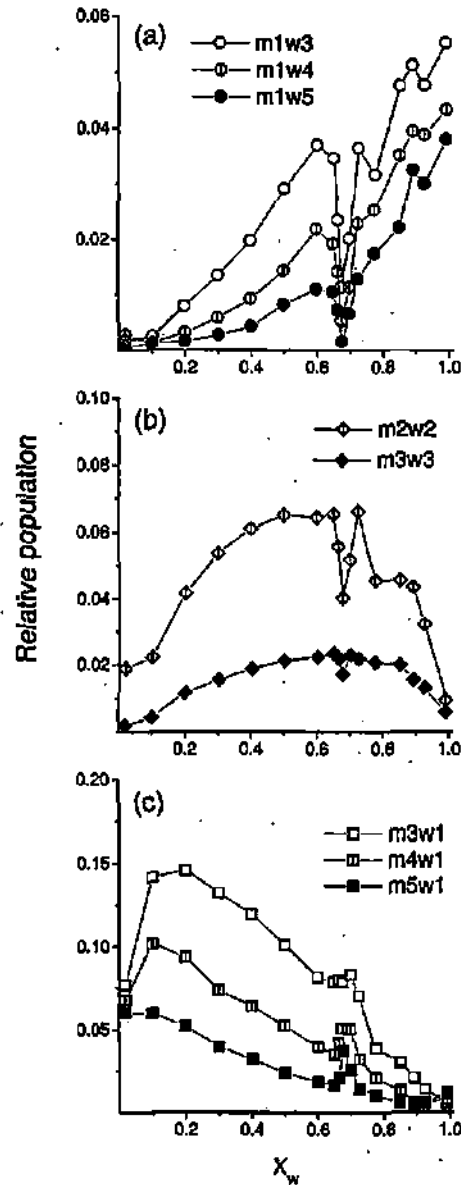
Fig. 4.14 Variation in the relative populations of mixed clusters of nuclearity four, five and six with x_w for (a) W_nM_1 clusters (b) W_nM_n clusters and (c) W_1M_n clusters.

II ($0.3 < x_w \leq 0.6$), the mixed cluster population increases with practically no change in Δ, the latter being at its maximum value (~ 0.17). Interestingly, this change in the trend from regime I to II is consistent with that in Fig. 4.13 where the population fraction of the mixed clusters varies roughly proportional to x_w with somewhat different slopes in the two regimes. Our findings are in close agreement

with the XRD studies [29] according to which, the chain-like structures predominantly of methanol present in the first regime (x_w < 0.3) give way to tetrahedral species characteristic of water when x_w increases beyond 0.3. With the imbalance between homo-hetero interactions remaining constant ($\Delta \sim 0.17$), the beginning of regime II should mark a change in the nature of the mixed species with x_w. This is clearly seen in Fig. 4.14. Below x_w=0.3 (regime I), water-rich species are less populated in the cluster beam (see W_nM_1 in Fig. 4.14a), while those rich in methanol are on the increase (W_1M_m in Fig. 4.14c). In regime II (0.3 < x_w ≤ 0.6), the water-rich clusters increase steeply while the methanol-rich clusters decrease. In regime III (0.85 <x_w < 1), the hetero interactions in the liquid diminish with greater abundance of the tetrahedral water species giving rise to more neat water clusters in the vapor (see Fig. 4.13a).
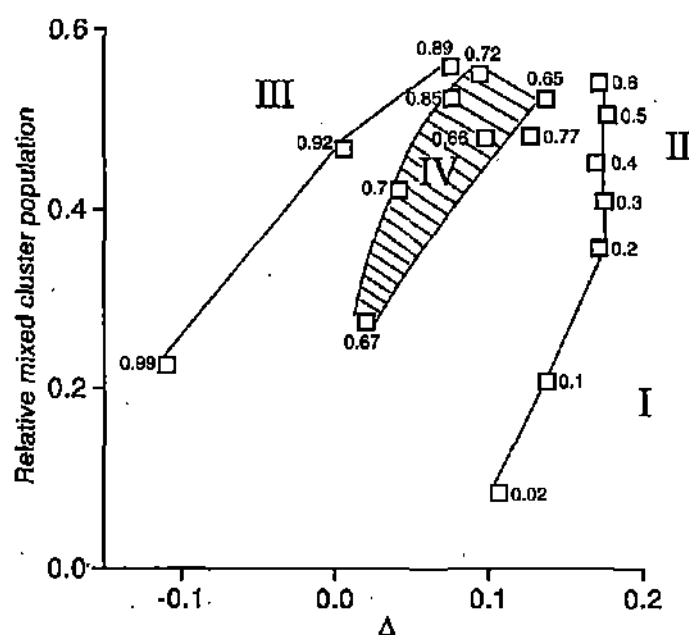

Fig. 4.15 Fraction of mixed clusters against the deviation, Δ, of the mole fraction from the ideal (from Fig. 4.12). Four different regimes are identified in the plot. The x_w values are shown alongside each point.

In contrast to previous studies [29], we identify an additional, but relatively narrower regime, IV (x_w = 0.65 to 0.77) in Fig. 4.15, where cluster populations

undergo dramatic changes (see Fig. 4.13 and 4.14) due to a transient structure adopted by the liquid mixture.

Mixed cluster population decreases and reaches minimum at $x_w = 0.67$, matching well with that at the end of regime I. Therefore, only the methanol-rich chain-like clusters seem to survive. The Δ value at $x_w = 0.67$ is close to zero. This does not simply mean that the liquid turned ideal, but instead reflects a situation where the water-methanol interaction in the liquid is maximized with the excess enthalpy of mixing reaching minimum. At this composition, the nucleation of tetrahedral water species perhaps reaches a criticality, giving rise to an extended hydrogen bonded network of water and methanol in the liquid [24,28].

Under such a circumstance, what could emerge out of the liquid mixture are the small nuclearity species from the boundaries of hydrogen bonded domains. Accordingly, we observe a relative rise in the monomeric species mainly of methanol as shown in Fig. 4.13a. This scenario exists only for a narrow range of x_w, 0.6 to 0.75. On either side, the homo-interactions could intercept the network structure yielding water clusters stabilized by the methanol molecules or vice versa [28]. In regime IV, therefore, the Δ value is complementary to the nature of interactions in the liquid and provides a strong evidence for an 'enthalpy-frozen liquid'.

Conclusions

The binary vapor emerging from the surface of water-methanol liquid mixture has been examined in the form of a molecular beam by time-of-flight mass spectrometry. Hydrated neat clusters of water (W_nH^+) and methanol (M_mH^+) as well as mixed species of the type $W_nM_mH^+$ were observed (n, m upto 10) under the given

experimental conditions, the relative populations varying with the liquid composition. When the water mole fraction in the liquid, x_w, is < 0.6, M_mH^+ and $W_1M_mH^+$ clusters dominate the mass spectrum. A comparison of the mole fractions of water and methanol in the vapor estimated from the populations of the various cluster species with those obtained assuming ideality of the liquid mixture showed that methanol promotes water vaporization considerably in the form of mixed cluster species. With $x_w > 0.75$, W_nH^+ start appearing with a gradual decline in the populations of M_mH^+. In the range $0.6 < x_w < 0.75$, the populations of neat clusters pass thorough a sharp rise while those of mixed species exhibit a complementary trend. Interestingly, this anomaly is observed at a liquid composition where the excess enthalpy of mixing reaches a minimum implying that the hetero-interactions are the most favored. The liquid seems to adopt a transient structure involving extended network of water and methanol molecules held in place by the intermolecular hydrogen bonds. The reluctance of the mixed species to emerge out of the liquid is perhaps due to the inter-locking of molecules in the network. As a result, only monomeric species are observed. Coincident with this, the mole fractions of water and methanol in the vapor approach 'the ideal' values. Our work has, thus, shown that the binary vapor adopts varying structures as though it remembers from which liquid mixture it is originating. It is quite a representative of the liquid structure barring the range, $0.6 < x_w < 0.75$ where it, indeed, provides a complementary picture of the liquid structure.

4.5 Ternary alcohol-water mixtures

Introduction

Ternary systems such as alkane-alcohol-alcohol have been studied extensively with the primary motivation of deducing thermodynamic properties such as excess molar enthalpies and volumes besides vapor-liquid and liquid-liquid equilibria [33-36]. However, the study of ternary systems containing associating components like water and primary alcohols has proved extremely difficult in the absence of a reliable thermodynamic model [37]. A lone example from our literature survey is due to Ikari et al. [38], who studied vapor-liquid equilibria of the water-ethanol-1-propanol system added with a small amount of furfural added On the other hand, there has been some effort to study the surfaces of water-alcohol liquid mixtures, especially the aspect of surface enrichment by the alcohol molecules.

We have been interested in investigating the competitive surface enrichment in aqueous alcohols. In our earlier work on binary mixtures of primary alcohols and water (see section 4.3), we ___ demonstrated based on mass spectrometric analysis, that the vapor generated in equilibrium with the liquid surface can be used directly to obtain the surface concentration profile of the alcohol. It was shown that as the length of the alcohol molecule increased, the surface enrichment reached saturation at progressively lower concentrations of alcohol in the liquid mixture. Although, there are a few other techniques to determine the surface enrichment such as neutron reflectivity [39], second-harmonic and sum-frequency spectroscopy [40], our method based on mass spectrometry is straightforward and easy to use, and can be performed over the entire compositional range. Neutron reflectivity, for instance, suffers from an inherent problem of not being able to resolve small molecules owing to diminishing contrast between their scattering factors in multicomponent systems,

especially at low concentrations [39]. Having proven that the mass spectrometric way of looking at the vapor of an alcohol-water liquid mixture is a reliable method to determine the surface composition profiles in such mixtures and also the simplicity of our method, we decided to investigate competitive surface enrichment in ternary mixtures of alcohol-alcohol-water. This study is the first of its kind. Specifically, we have determined the surface concentration profiles of water-methanol-1-propanol, water-ethanol-1-propanol and water-methanol-ethanol liquid mixtures at different compositions by mass spectrometric analysis of the ternary vapor in equilibrium with the liquid surface. For this purpose, we generated a cluster beam of the ternary vapor swept off the surface of the liquid mixture, by injecting it into vacuum through a pulsed supersonic valve. We have compared the results from this study with the binary water-alcohol mixtures from our earlier study (section 4.3).

Experimental

Ternary mixtures of water-methanol-ethanol, water-methanol-1-propanol and water-ethanol-1-propanol containing equimolar proportions of alcohols were prepared covering a whole range of water:alcohol compositions. As in the case of binary mixtures, 6 ml of the ternary mixture was placed in a stainless steel cell connected to a pulsed supersonic valve (R.M. Jordan, USA) and was subjected to a helium backpressure of 2 atmospheres from the top. In order to generate the molecular beam, the alcohol-water vapor was injected into a vacuum of 10^{-7} torr through a 0.5 mm orifice of the pulsed valve, operating at 10 Hz and 4000 A.

Mass Spectra

Water-methanol-1-propanol system

In Fig. 4.16, we show as an example the time-of-flight mass spectrum obtained with a water-methanol-propanol ternary liquid mixture with the composition, $x_W : x_M : x_P = 0.6:0.2:0.2$, where x stands for the mole fraction. The dominance of propanol clusters, p_1 to p_3, is clearly seen in the mass spectrum. Mixed clusters of alcohols like m_1p_1, m_1p_2 and m_2p_1 are the next highest in intensity. The intensities of the water attached clusters, such as m_nw_m, p_lw_m and $m_np_lw_m$ ($n < 3$, $l < 4$, $m < 4$) are rather small.

We found it useful to compare this spectrum with those from the corresponding water-methanol and water-propanol binary mixtures. For this purpose, the ternary mixture was assumed to be a mixture of two binary systems with internal ratios of $x_W/2 : x_M$ and $x_W/2 : x_P$, water being equally partitioned between the two alcohols. The corresponding compositions of the binary mixtures are, therefore, $x_W : 2x_M$ and $x_W : 2x_P$ respectively such that $x_W + 2x_M = 1$ and $x_W + 2x_P = 1$. Thus, the 0.6:0.2:0.2 ternary system may be considered to be a mixture of two binary systems with compositions of 0.6:0.4 each. In the inset of Fig. 4.16, we show the mass spectra from W-M ($x_W : x_M = 0.6:0.4$) and W-P ($x_W : x_P = 0.6:0.4$) systems. Comparing the populations of methanol clusters between the ternary W-M-P system and the binary W-M system, we find that clustering of m_2 and m_3 is not favored as much in the ternary system and accordingly, the water attachment to these clusters is also suppressed. In contrast, the populations of p_1 and p_2 in the ternary as well as in the corresponding W-P binary system show similar trends.

Fig. 4.16 Time-of-flight mass spectra of water-methanol-propanol ternary system of composition $x_W : x_M : x_P = 0.6:0.2:0.2$. The peaks are assigned to different protonated clusters of methanol, propanol and water as well as their mixed clusters. The degeneracy in mass assignments of some peaks is mentioned alongside. The insets show the mass spectra from the chosen binary mixtures of water-methanol ($x_W : x_M = 0.6:0.4$) and of water-propanol ($x_W : x_P = 0.6:0.4$).

Water attachment to the propanol clusters is enhanced in the ternary system as compared to the binary system.

Water-ethanol-1-propanol system

In Fig. 4.17 is shown the time-of-flight mass spectrum obtained with a water-ethanol-propanol ternary liquid mixture with the composition, $x_W : x_E : x_P =$ 0.5:0.25:0.25, where x stands for the mole fraction. Mixed clusters of alcohols such as e_1p_1, e_1p_2 and e_2p_1 as well as pure propanol clusters (p_2 and p_3) are dominant followed by pure ethanol clusters (e_1 and e_2). The intensities of the water attached clusters, such as e_1w_m, p_1w_m and $m_1p_nw_m$ ($n < 3$, $1 < 4$, $m < 3$) are rather small.
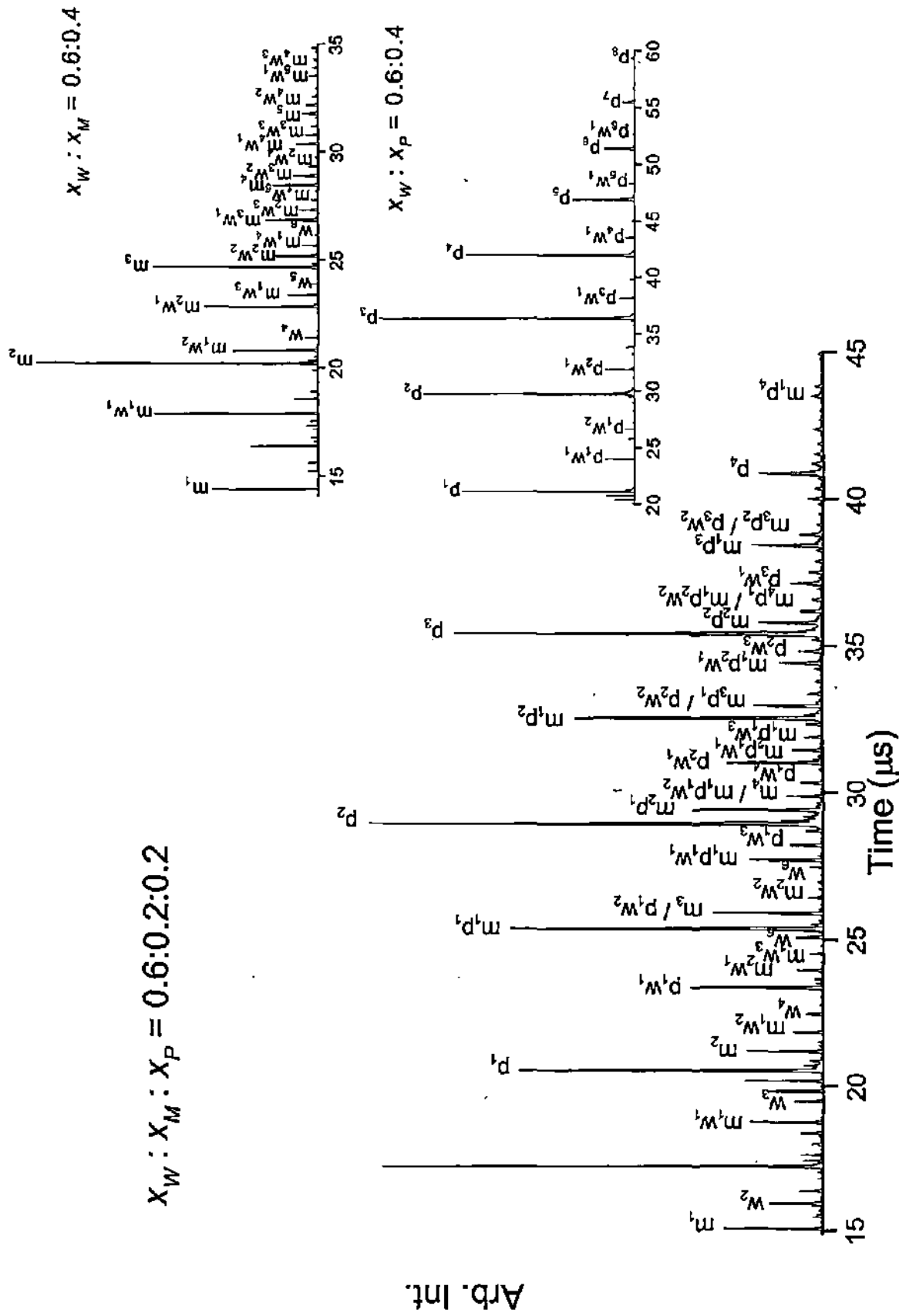
$$x_W : x_E : x_P = 0.5{:}0.25{:}0.25$$

Fig. 4.17 Time-of-flight mass spectra of water-ethanol-propanol ternary system of composition $x_W : x_E : x_P = 0.5{:}0.25{:}0.25$. Different protonated clusters of pure ethanol, propanol and water as well as their mixed clusters are seen in the mass spectrum. Degeneracy in mass assignments of some peaks is mentioned alongside.

112

Water-methanol-ethanol system

Fig. 4.18 shows the time-of-flight mass spectrum obtained with a water-methanol-ethanol ternary liquid mixture with the composition, $x_W : x_M : x_E = 0.5:0.25:0.25$, where x stands for the mole fraction. Pure ethanol clusters, e_1 to e_4 dominate the spectrum. Mixed clusters of alcohols such as m_1e_1, m_1e_2 and m_2e_1 are next highest in intensity followed by water attached clusters such as m_ne_t, e_1w_t and $m_ne_1w_t$, ($n < 4$, $t < 4$, $l<4$) which have the lowest intensities.
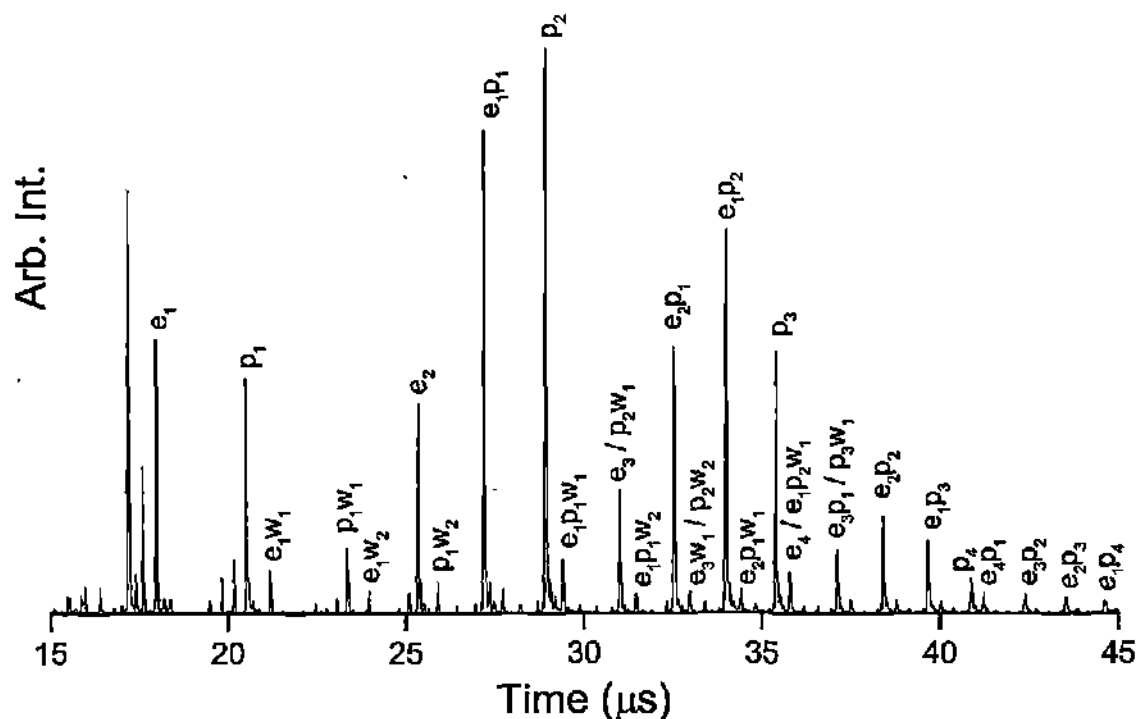
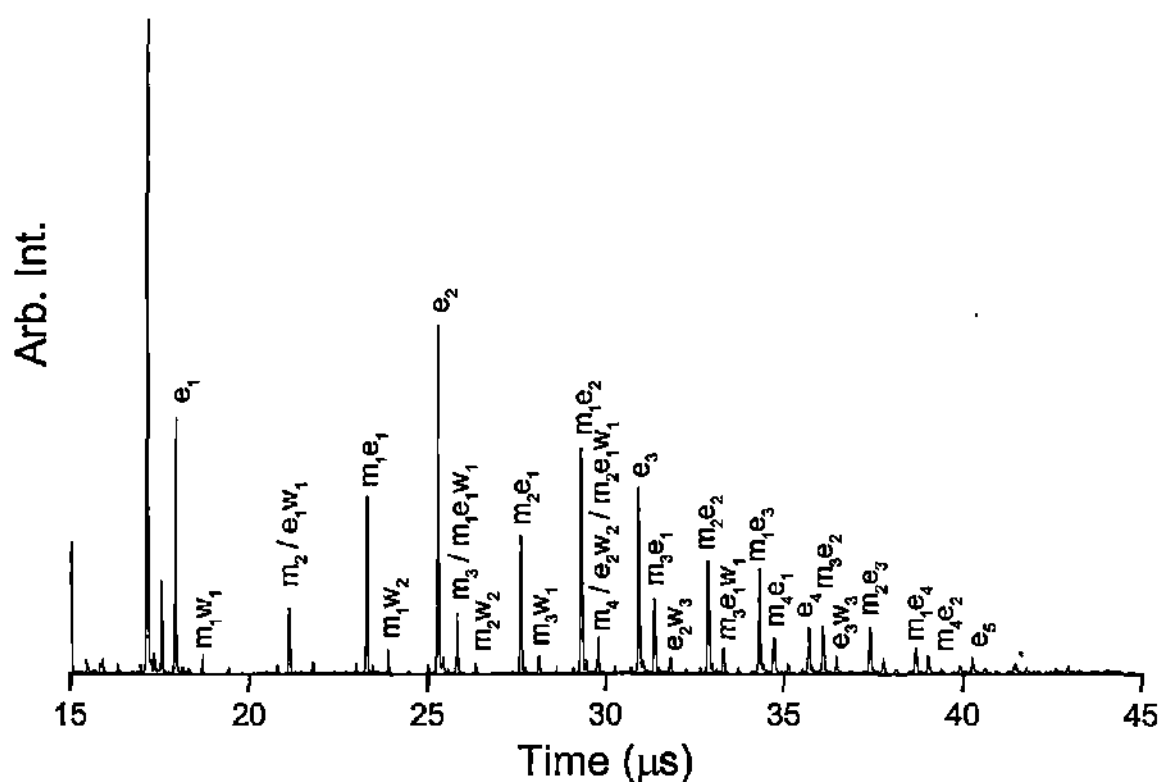$$x_W : x_M : x_E = 0.5:0.25:0.25$$

Fig. 4.18 Time-of-flight mass spectra of water-methanol-ethanol ternary system of composition $x_W : x_M : x_E = 0.5:0.25:0.25$. Different protonated clusters of pure methanol, ethanol and water as well as their mixed clusters are seen in the mass spectrum. Degeneracy in mass assignments of some peaks is mentioned alongside.

Analysis and discussion

Cluster species obtained from ternary mixtures of water-methanol-ethanol, water-methanol-1-propanol and water-ethanol-1-propanol were analyzed in a similar manner as in the case of binary alcohol-water mixtures. We estimated the vapor composition (y_M and y_P) of the ternary system by counting the number of methanol, propanol and water molecules in neat as well as mixed cluster species.

$$y_M = \frac{\sum m}{\sum m + \sum p + \sum w} \qquad (4.9)$$

$$y_P = \frac{\sum p}{\sum p + \sum m + \sum w} \qquad (4.10)$$

where m, p and w correspond respectively to the number of methanol, propanol and water molecules in a given cluster and the summation is over all the clusters observed in the mass spectrum.
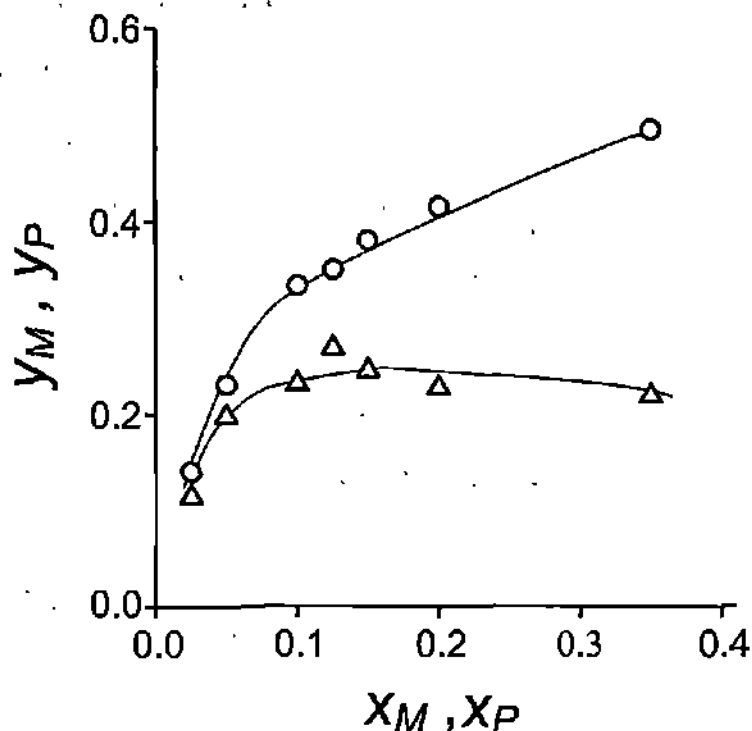

Fig. 4.19 Ternary W-M-P mixture: Variation in the vapor mole fractions of methanol, y_M ($\triangle$) and propanol, y_P (O) with the mole fraction of methanol, x_M and propanol, x_P in the liquid.

In Fig. 4.19, the y_M and y_P values are plotted against the mole fractions of the individual alcohols, x_M and x_P in the ternary liquid mixture. We observe that y_P values are greater than y_M at all compositions above $x_M(x_P)$ of 0.05. Although, the vapor pressure of methanol is much higher (17.5 kPa) than that of propanol (1.3 kPa), the dominance of the latter in the vapor is clearly related to its ability to enrich the liquid surface. While y_P shows a gradual increase, y_M decreases to some extent beyond x_M of 0.12. It remains to be seen whether this effect arises due to the longer chain propanol pushing methanol molecules deep into the liquid bulk or due to increased affinity between water and methanol. In the dilute regime (x_M (x_P) < 0.05), where water is abundant, y_M is nearly equal to y_P suggesting equal propensity for both methanol and propanol to be in the vapor.

It is instructive to compare the ternary vapor mole fractions, y_M and y_P, with the corresponding values obtained from binary water-methanol and water-propanol mixtures. To make this comparison feasible, we propose a pseudo ternary liquid system containing equal fractions of water-methanol and water-propanol binary mixtures (as detailed above) wherein there is no interaction, whatsoever, between methanol and propanol molecules (see schematic in Fig. 4.20). Thus, our pseudo-ternary liquid is a semi-ideal system where water alone interacts individually with the two alcohol molecules. The vapor composition of this system may be calculated as follows:

$$y'_M = \frac{\sum m}{\sum m + \sum w_M + \sum p + \sum w_P} \qquad (4.11)$$

$$y'_P = \frac{\sum p}{\sum p + \sum w_P + \sum m + \sum w_M} \qquad (4.12)$$

where m and p correspond to the number of methanol and propanol molecules, obtained from the cluster beams of the respective binary mixtures while w_M and w_P stand for the respective water molecules.

Compare

Interaction ON
Experimental ternary

Interaction OFF
Pseudo-ternary

$x_W{:}x_M{:}x_P = 0.6{:}0.2{:}0.2$

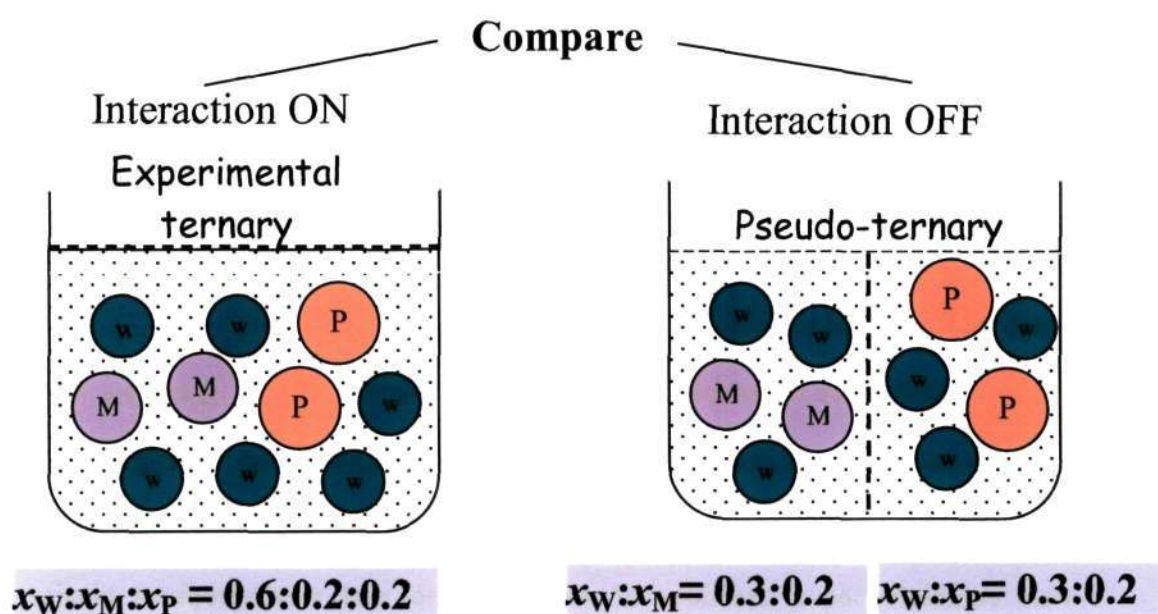$x_W{:}x_M = 0.3{:}0.2$ $x_W{:}x_P = 0.3{:}0.2$

Fig. 4.20 Schematic illustration of an alcohol-alcohol-water ternary system (experimental ternary) which can be assumed to be made up of two corresponding binary alcohol-water system (psuedo-ternary).

Water-methanol-1-propanol system

The experimental vapor mole fractions of methanol and propanol (y_M and y_P) are compared with the corresponding values from the psuedo-ternary system in Fig. 4.21. In the dilute regime ($x_M \leq 0.15$), y_M and y'_M have similar values, implying that the methanol-propanol (M-P) interaction is minimal (Fig. 4.21a). Thus, the fraction of methanol emerging from the ternary liquid mixture remains unbiased in the presence of propanol. When the alcohol content increases beyond $x_M = 0.15$, y_M

values appear somewhat smaller than y'_M. This may be taken to indicate that the methanol molecules are driven away into the bulk due to the presence of propanol molecules on the surface. Similarly for propanol (Fig. 4.21b), y_P is close to y'_P in the dilute regime ($x_P \leq 0.05$), indicating that M-P interaction does not significantly influence the W-P interaction. With increase in the alcohol content ($0.05 < x_P \leq 0.25$), y_P becomes lesser than y'_P which means that the surface enrichment of propanol in the W-M-P system suffers to some extent due in the presence of methanol. This clearly provides an evidence for methanol-propanol interaction in the ternary liquid. In the alcohol-rich region ($0.25 < x_M \leq 0.4$), the surface-enriching behavior of propanol dominates and, therefore, y_P almost matches y'_P. Comparing y_P and y_M values in Fig. 4.21a and b, it is apparent that propanol prefers itself to be on the surface of the liquid mixture especially at higher alcohol contents, an observation that goes well with the known behavior of propanol (section 4.3). We compare in the inset of Fig. 4.21, the total vapor fraction of alcohol, y_A ($= y_M + y_P$) from experimental ternary, and y'_A ($= y'_M + y'_P$) from the pseudo-mixture as a function of total alcohol content, x_A ($= x_M + x_P$). We see that y_A values are comparable to y'_A in the dilute region ($x_A \leq 0.2$) while above $x_A = 0.2$, y_A is less by ~ 0.2. The surface enrichment of both propanol and methanol therefore, appear demoted in the alcohol-rich region. In other words, methanol molecules are pushed more into the bulk liquid while propanol does not enrich the surface as much as it would have, in the absence of methanol.

Water-ethanol-1-propanol system

The vapor composition y_E and y_P were estimated in a similar manner as for W-M-P system (see equations 4.9 and 4.10). The y'_E and y'_P values of the W-E-P

pseudo-system were calculated following similar equations as in equations (4.11) and (4.12).
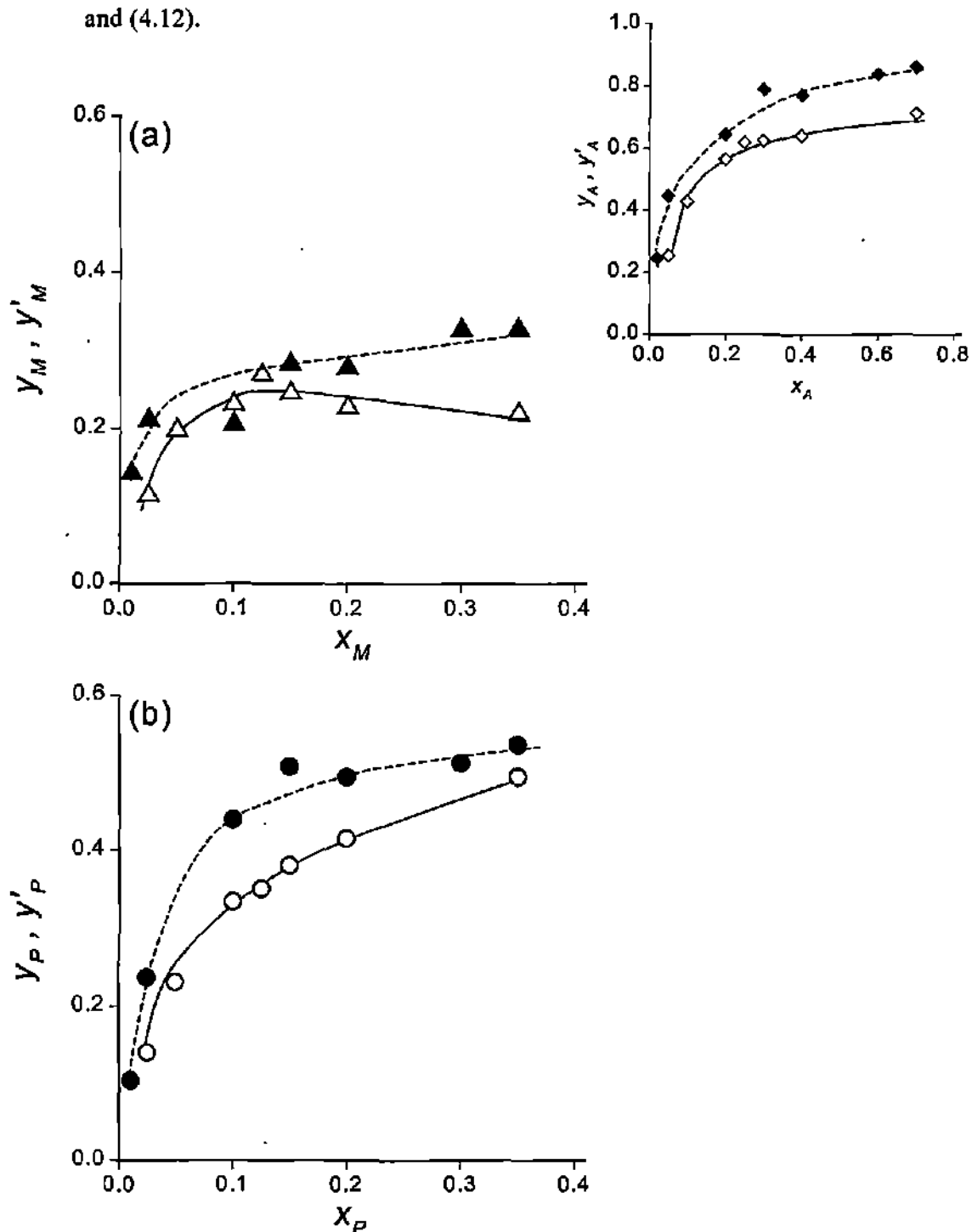

Fig. 4.21 Ternary W-M-P mixture: (a) Variation in the methanol vapor mole fraction, y_M ($\triangle$), from the experimental ternary and y'_M ($\blacktriangle$) from the psuedo-mixture as a function of methanol fraction in the liquid, x_M. (b) Variation in the propanol vapor mole fraction, y_P (O), from the experimental ternary and y'_P ($\bullet$) from the psuedo-mixture as a function of propanol fraction in the liquid, x_P. Inset shows the variation of the total alcohol fraction in the vapor, y_A ($\diamondsuit$) from the experimental ternary and y'_A ($\blacklozenge$) from the psuedo-mixture as a function of the total alcohol fraction in the liquid, x_A.

Their variations with respect to the liquid composition, x_E (x_P), are shown in Fig. 4.22. The y_E (Fig. 4.22a) and y_P (Fig. 4.22b) values exhibit similar trends as in the case of W-M-P system. In the dilute region $(x_E(x_P) \leq 0.1)$, y_E matches well with y_P indicating equal propensity for both ethanol and propanol to be in the vapor. Beyond the dilute region, $0.1 < x_E$ $(x_P) \leq 0.45$, y_P values are higher due to the higher surface enriching ability of propanol.

In the dilute region $(x_E(x_P) \leq 0.05)$ in Fig. 4.22a, y_E from the ternary W-E-P system matches well with y'_E from the pseudo-ternary system, as do y_M and y'_M in the case of W-M-P system. This indicates that the water-ethanol interaction is not influenced by the presence of propanol or by the E-P interaction in this region. With the increase in the alcohol concentration, the E-P interaction comes into play and as a result, y_E fraction appears higher than y'_E. In other words, the propanol molecules in this ternary mixture like to associate themselves with the ethanol molecules, thereby enhancing the surface enrichment of ethanol. Figure 4.22b shows the corresponding variation for y_P and y'_P in the W-E-P system. In this case, y_P values are considerably lowered compared to y'_P, more than that in the W-M-P system although the y_P values by themselves are comparable in the two ternary systems (see Figs. 4.21b and 4.22b). Obviously, the E-P interaction is stronger than the M-P interaction. The inset shows the variation of the total alcohol fraction in the vapor as a function of total alcohol content in the ternary liquid mixture, along with the corresponding values from the pseudo-mixture. Comparing the insets of Figs. 4.21 and 4.22, we see that the total fraction, y_A, is lowered less compared to y'_A. Thus, propanol seems to behave differently in the two ternary systems. In the W-M-P system, the association between methanol and propanol is poorer and therefore, propanol enriches the liquid surface more or less independently.
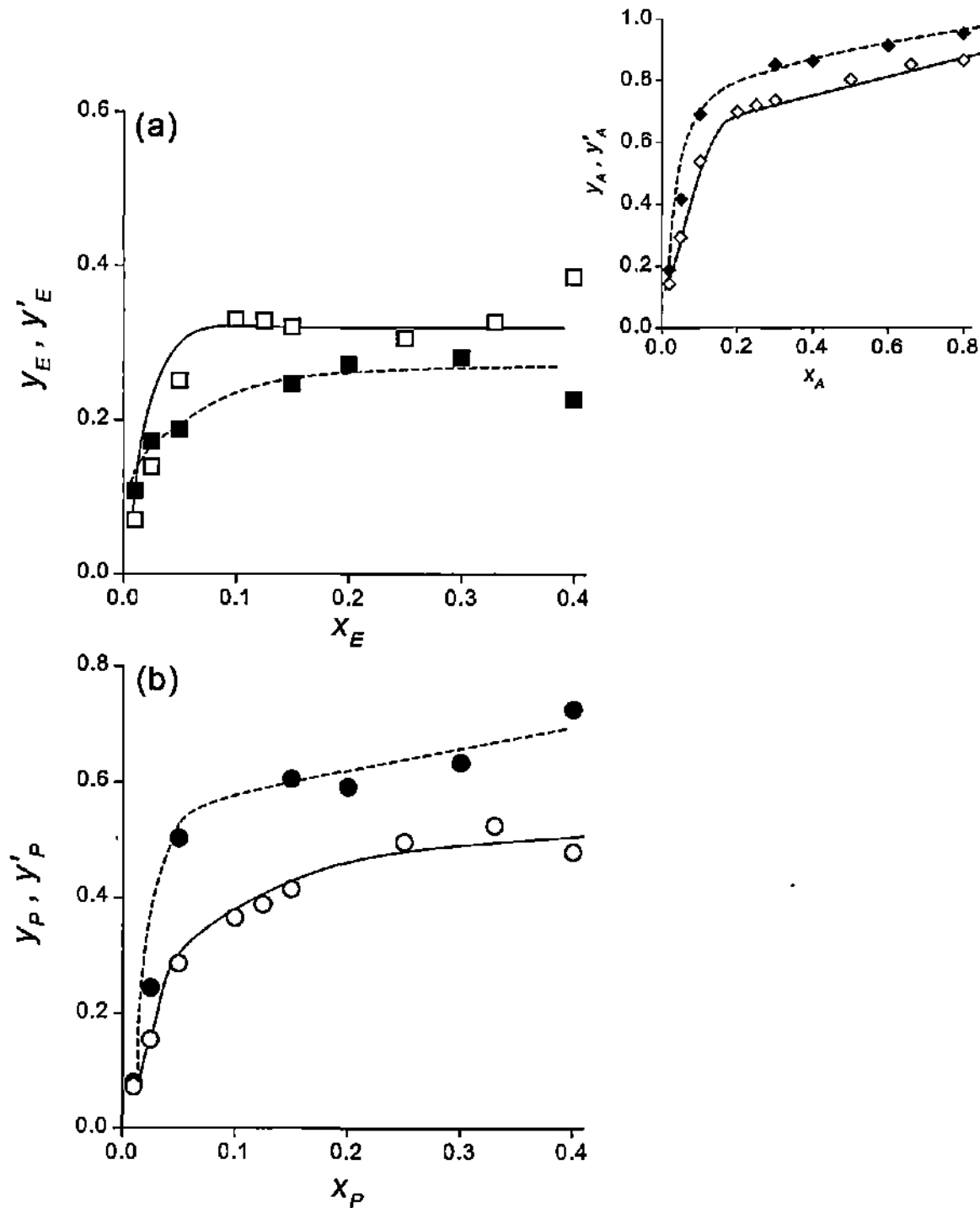
Fig. 4.22 Ternary W-E-P mixture: (a) Variation in the ethanol vapor mole fraction, y_E (□), from the experimental ternary and y'_E (■), from the psuedo-mixture as a function of ethanol fraction in the liquid, x_E. (b) Variation in the propanol vapor mole fraction, y_P (○), from the experimental ternary and y'_P (●), from the psuedo-mixture as a function of propanol fraction in the liquid, x_P. Inset shows the variation of the total alcohol fraction in the vapor, y_A (◇) from the experimental ternary and y'_A (◆) in pseudo-mixture as a function of the total alcohol fraction in the liquid, x_A.

On the other hand, propanol associates itself more with ethanol and as a consequence, ethanol is also promoted to the surface. In both cases, this comes about at a cost for propanol for, its surface enriching ability gets demoted substantially causing the total alcohol fraction at the surface also to decrease.

Water-methanol-ethanol system

The experimental vapor mole fractions, y_M and y_E, from the ternary W-M-E mixture are plotted in Fig. 4.23 as a function of $x_M(x_E)$, along with the values, y'_M and y'_E, from the corresponding pseudo-mixture. The trends seen here are very different compared to the other two systems, W-M-P and W-E-P in Figs. 4.21 and 4.22. In the dilute region, the y_M values (Fig. 4.23a) are nearly double that of y_E (Fig. 4.23b). Surface enriching ability being poor for methanol (section 4.4), this observation may be related to its higher vapor pressure. As the ethanol concentration increases, y_E increases dramatically to a value of ~ 0.7 for x_E of 0.4, while y_M decreases to some extent. On comparing with the values from the pseudo-mixture, we find that y_M values are much higher than y'_M at low concentrations of methanol in the liquid, x_M (x_E) ≤ 0.15 (see Fig. 4.23a). It appears that the M-E interaction is present even at such low concentrations. With increase in the concentration (0.15< $x_M(x_E)$ $\leq$ 0.4), y_M is lowered below y'_M while the trend is reversed for ethanol (see Fig. 4.23b). Accordingly, the total alcohol fraction, y_A, from the W-M-E ternary system closely matches that of y'_A from the pseudo-ternary system as shown in the inset of the figure. This is indeed misleading, as it implies no interaction between methanol and ethanol, contrary to observations made from Fig. 4.23a and b. However, this is not the correct scenario.
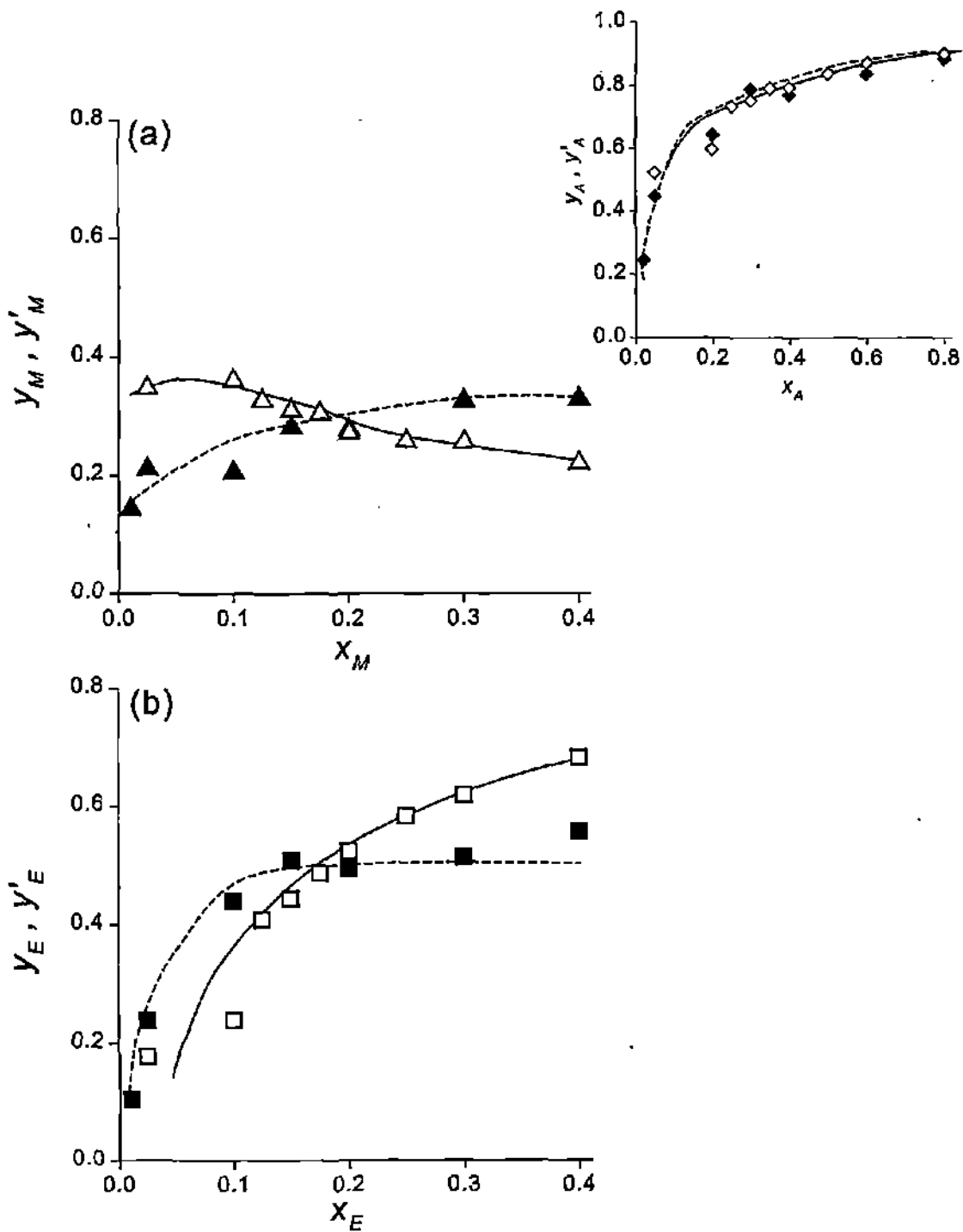
Fig. 4.23 Ternary W-M-E mixture: (a) Variation in the methanol vapor mole fraction, y_M (O), from the experimental ternary and y'_M (●), from the psuedo-mixture as a function of methanol fraction in the liquid, x_M. (b) Variation in the ethanol vapor mole fraction, y_E (□), from the experimental ternary and y'_E (■), from the psuedo-mixture as a function of ethanol fraction in the liquid, x_E. Inset shows the variation of the total alcohol fraction in the vapor, y_A (◇) from the experimental ternary and y'_A (◆) from pseudo-mixture as a function of the total alcohol fraction in the liquid, x_A.

Since both alcohols possess only moderate ability for surface enrichment, their enriching abilities and the vapor pressures seem to balance each other such that the actual surface coverage of alcohol remains similar to what would be there in the absence of any interaction between the two.

Conclusions

The investigations of the effect of competing surface-enrichment of primary alcohols in ternary alcohol-water mixtures has revealed that the net surface enrichment by alcohol molecules is lowered in comparison with that in binary mixtures. The surface enriching ability for the longer chain propanol suffers in the ethanol-water mixture on account of stronger association between the two molecules. As a result, the enriching ability of ethanol is promoted, while that of methanol is not affected. In the W-M-E system, methanol due to its higher vapor pressure, enriches the liquid surface at lower concentrations while ethanol with relatively higher enriching ability, does it at higher concentrations. Both the factors balance out to give rise to a net surface enrichment as if there were no interaction between the two alcohols.

References

[1] J. W. Cahn, *J. Chem. Phys.* 66, 3667 (1977).

[2] D. Myers, *'Surfaces, Interfaces, and Colloids, Principles and Applications'* VCH: New York (1991).

[3] A. Ozawa and A. Minamisawa, *Jpn. J. Appl. Phys.* 36, 2951 (1977).

[4] E. A. Guggenheim, *'Thermodynamics'* North-Holland: Amsterdam (1967).

[5] R. A. Zahoransky and F. Peters, *J. Chem. Phys.* 83, 6425 (1985).

[6] G. Wilemski, *J. Phys. Chem.* 91, 2492 (1987).

[7] J. L. Schmitt, J. Whitten, G. W. Adams and R. A. Zalabsky, *J. Chem. Phys.* 92, 3693 (1990).

[8] A. Laaksonen, *J. Chem. Phys.* 97, 1983 (1992).

[9] Y. Viisanen, R. Strey, A. Laaksonen and M. Kulmala, *J. Chem. Phys.* 100, 6062 (1994).

[10] D. Myers in *'Surfaces, Interfaces and Colloids Principles and Applications'* VCH Publishers: New York (1991), p.21.

[11] R. K. Schofield and E. K. Ridel, *Proc. R. Soc. Lond. A* 109, 60 (1925).

[12] J. Penfold and R. K. Thomas, *J. Phys.: Condens. Matter*, 2, 1369 (1990).

[13] X. Zhao, W. Zhao, J. Sokolov, M. H. Rafailovich, S. A. Schwarz, B. J. Wilkens, R. A. L. Jones and E. Kramer, *J. Macromolecules* 24, 5991 (1991).

[14] S. J. Roser, R. Felici and A. Eaglesham, *Langmuir* 10, 3853 (1994).

[15] Z. X. Li, J. R. Lu, D. A. Styrkas, R. K. Thomas, A. R. Rennie and J. Penfold, *Mol. Phys.* 80, 925 (1993).

[16] E. A. Guggenheim and N. K. Adam, *Proc. R. Soc. Lond. A* 139, 213 (1933).

[17] If, as an upper limit, the length of the molecule is assumed to be 7 Å, the value of $x_E(s)$ changes to some extent. For example at x_E of 0.045, $x_E(s)$ came out to be 0.18 compared to 0.21 for 5.5 Å length.

[18] M. Matsumoto, N. Nishi, T. Furusawa, M. Saita, T. Takamuku, M.Yamagami and T. Yamaguchi, *Bull. Chem. Soc. Jpn.* 68, 1775 (1995).

[19] Z. X. Li, J. R. Lu, R. K. Thomas, A. R. Rennie and J. Penfold, *J. Chem. Soc. Faraday Trans.* 92, 565. (1996).

[20] A.G. Mitchell and W.F.K. Wynne-Jones, *Discuss. Faraday Soc.* 15, 161. (1953).

[21] K. Nakanishi, *Bull. Chem. Soc. Jpn.* 33, 793. (1959).

[22] D.P. Shoemaker and C.W. Garland, *'Experiments in Physical Chemistry'* McGraw-Hill: USA (1962), p.166.

[23] F. Franks and D.J.G. Ives, *Q. Rev., Chem. Soc.* 20, 1 (1966).

[24] *'Water: A Comprehensive Treatise'* Edited by F. Franks, Plenum: New York (1973).

[25] P. Kebarle, R.N. Haynes and J.G. Collins, *J. Am. Chem. Soc.* 89, 5733 (1967).

[26] A.J. Stace and A.K. Shukla, *J. Am. Chem. Soc.* 104, 5314 (1982).

[27] N. Nishi and K. Yamamoto, *J. Am. Chem. Soc.* 109, 7353 (1987).

[28] A. Wakisaka, H.Abdoul-Carime, Y. Yamamoto and Y. Kiyozumi, *J. Chem. Soc., Faraday Trans.* 94, 369 (1998).

[29] T. Takamuku, T. Yamaguchi, M. Asato, M. Matsumoto and N. Nishi, *Z. Naturforsch.* 55a, 513 (2000).

[30] P.W. Atkins, *'Physical Chemistry'*, Oxford University Press: Oxford (1986), p.169.

[31] E.P. Grimsrud and P. Kebarle, *J. Am. Chem. Soc.* 95, 7939 (1973).

[32] M. Matsumoto, N. Nishi, T. Furusawa, M. Saita, T. Takamuku, M. Yamagami and T. Yamaguchi, *Bull. Chem. Soc. Jpn.* 68, 1775 (1995).

[33] A. Aucejo, S. Loras, R. Muñoz and L. M. Ordoñez, *Fluid Phase Equilibria* 162, 241 (1999).

[34] A. G. Pradhan, V. R. Bhethanabotla and S. W. Campbell, *Fluid Phase Equilibria* 84, 183 (1993).

[35] J. R. Battler, W. M. Clark and R. L. Rowley, *J. Chem. Eng. Data* 30, 254 (1985).

[36] I. Nagata, K. Tamura and K. Miyai, *Fluid Phase Equilibria* 149, 147 (1998).

[37] G. M. Kontogeorgis, I. V. Yakoumis, H. Meijer, E. Hendriks and T. Moorwood, *Fluid Phase Equilibria* 158-160, 20 (1999).

[38] A. Ikari, Y. Hatate, Y. Uemura and A. Hamashima, *J. of Chem. Engg. Japan* 30, 539 (1997).

[39] Z. X. Li, J. R. Lu, D. A Styrkas, R. K.Thomas, A. R. Rennie and J. Penfold, *Mol. Phys.* 80, 925 (1993).

[40] K. B. Eisenthal, *Chem. Rev.* 96, 1343 (1996).

5. Reactive laser ablation of graphite in NH_3/He atmosphere: $(HCN)_m(NH_3)_nH^+$*

SUMMARY

The reaction of carbon vapor produced by the laser ablation of graphite with varying concentrations of jet-cooled ammonia seeded in helium carrier gas, has been investigated using a cluster apparatus. Carbon clusters are not formed in the presence of ammonia. Instead, new cluster species of the type $(HCN)_m(NH_3)_nH^+$ with m = 1 to 4 and n = 1 to 7 are observed, besides the $(NH_3)_nH^+$ species. The populations of the various cluster ions, determined at different NH_3/He ratios, show that the most preponderant species correspond to m = 1 and 2, viz. $(HCN)_1(NH_3)_4H^+$, $(HCN)_1(NH_3)_3H^+$ and $(HCN)_2(NH_3)_3H^+$. These clusters involving the tetrahedral coordination in the first solvation shell of NH_4^+ ion are also the most stable species, as verified by the molecular-orbital calculations performed using Gaussian 98W. The average complexation energy per addition of each NH_3 molecule in $(HCN)(NH_3)_nH^+$ decreases linearly with increasing n for n > 2.

---

* A paper based on this work has appeared in Chem. Phys. Lett. (2003).

5.1 Introduction

Mass spectrometry has been used extensively to study reactivity of carbon clusters including fullerenes [1]. Bare carbon clusters larger than C_{40}, in particular C_{60}, are essentially found to be unreactive with respect to NH_3, SO_2, NO_2, H_2, CO and O_2 [2,3]. On the other hand, smaller carbon clusters react with NH_3 and CH_3CN molecules to produce polar cyanopolyynes species [4]. It was proposed that CN radicals formed as intermediate species, react with free protons to give rise to cyanopolyynes with H and CN adding to the ends of linear carbon chains. Indeed, atomic carbon in the vapor state reacts readily with NH_3 and N_2 to produce the CN radical, which has been studied by various spectroscopic techniques such as optical absorption, laser-induced fluorescence, optical emission spectroscopy [5-9]. Shevin and co-workers [10,11] have reported the formation of HCN by co-condensing arc-generated carbon vapor and NH_3:

$$C + NH_3 \rightarrow \overset{-}{C}-\overset{+}{N}H_3 \rightarrow H\text{—}C\text{—}NH_2 \rightarrow H_2C\text{=}NH \rightarrow HCN + H_2 \qquad (5.1)$$
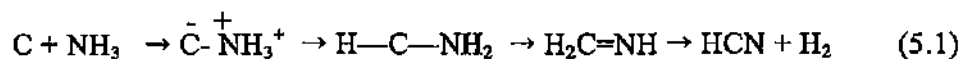
Co-expansion of the reactant gas and the carrier gas along with the plume of the target material is one of the most commonly employed experimental methods to study the reactivity of gas-phase clusters. We have performed a time-of-flight mass spectrometric analysis of the reaction products formed by co-expanding through a pulsed supersonic valve, the carbon vapor produced by laser ablation of graphite and a NH_3-He mixture. Our interest was to look at the reactivity of carbon clusters with different nitrogen containing molecules, towards the formation of carbon-nitrogen clusters. Besides ammonia, we also attempted reaction of carbon clusters with nitrogen and dimethylamine. In the case of nitrogen, we did not observe much reactivity and with dimethylamine as well as ablation of melamine and triazine, the degeneracy in the mass assignments became a problem to differentiate the reacted

carbon-nitrogen clusters formed. We observe that in the presence of NH$_3$, the nucleation of carbon clusters is completely suppressed and instead, adducts of the type $(HCN)_m(NH_3)_nH^+$ are formed (m upto 4; n upto 7), the relative intensity of the clusters depending on the NH$_3$/He ratio employed. These species are protonated in contrast to adducts of the type $(HCN)_n(NH_3)$ obtained by co-expanding HCN and NH$_3$ seeded in a mixture of argon and neon through a pulsed nozzle [12,13]. We also carried out molecular-orbital calculations to understand the stability of these clusters.

5.2 Experimental

Ammonia (purity, 99.9%) was introduced into a sample cell [14] along with He (99.999%) at a total back-pressure of 9.5 atm through a pulsed supersonic valve and the ratio of ammonia and helium in terms of their pressures was monitored using a Quadrupole Mass Spectrometer (RGA300, SRS). Vaporization laser (Nd-YAG 532 nm, ~60 mJ/pulse) was fired 120 μsec after the peak of the current pulse driving the spring of the pulsed valve. The carbon plume, formed by laser ablation of graphite was mixed with the NH$_3$-He gas pulse in the sample cell. The mass spectra were recorded both in off and on conditions of the vaporization laser, for various concentrations of NH$_3$ in He (0 to 1.8) keeping all other parameters fixed.

5.3 Results and discussion

In the laser-off condition, the mass spectrum showed prominently protonated $(NH_3)_n$ clusters (see Fig. 5.1), formed due to multi-photon ionization of the neutral clusters via intracluster ion-molecule reactions [15, 16]. Such cluster species contain a central NH$_4^+$ ion with four hydrogen bonding sites in the first

solvation shell [17,18]. Accordingly, the $(NH_3)_5H^+$ species was prominent in the spectrum, due to its magic nuclearity. Each of these mass peaks is accompanied by a small peak, which is one amu higher. As denoted in Fig. 5.1, such features may correspond to the ammonia cluster species containing one water molecule, the latter originating from the residual vacuum. Beyond n = 5, the mass peaks occur as multiplets and are generally of low intensity. These peaks are assignable to ammonia clusters containing 1-3 water molecules. Although the residual water in the chamber as well as impurity in ammonia were well below 10^{-6} torr as measured by the residual gas analyzer, water attachment to ammonia cannot be ruled out since ammonia is known to exhibit a greater affinity towards water, more so when n > 5.
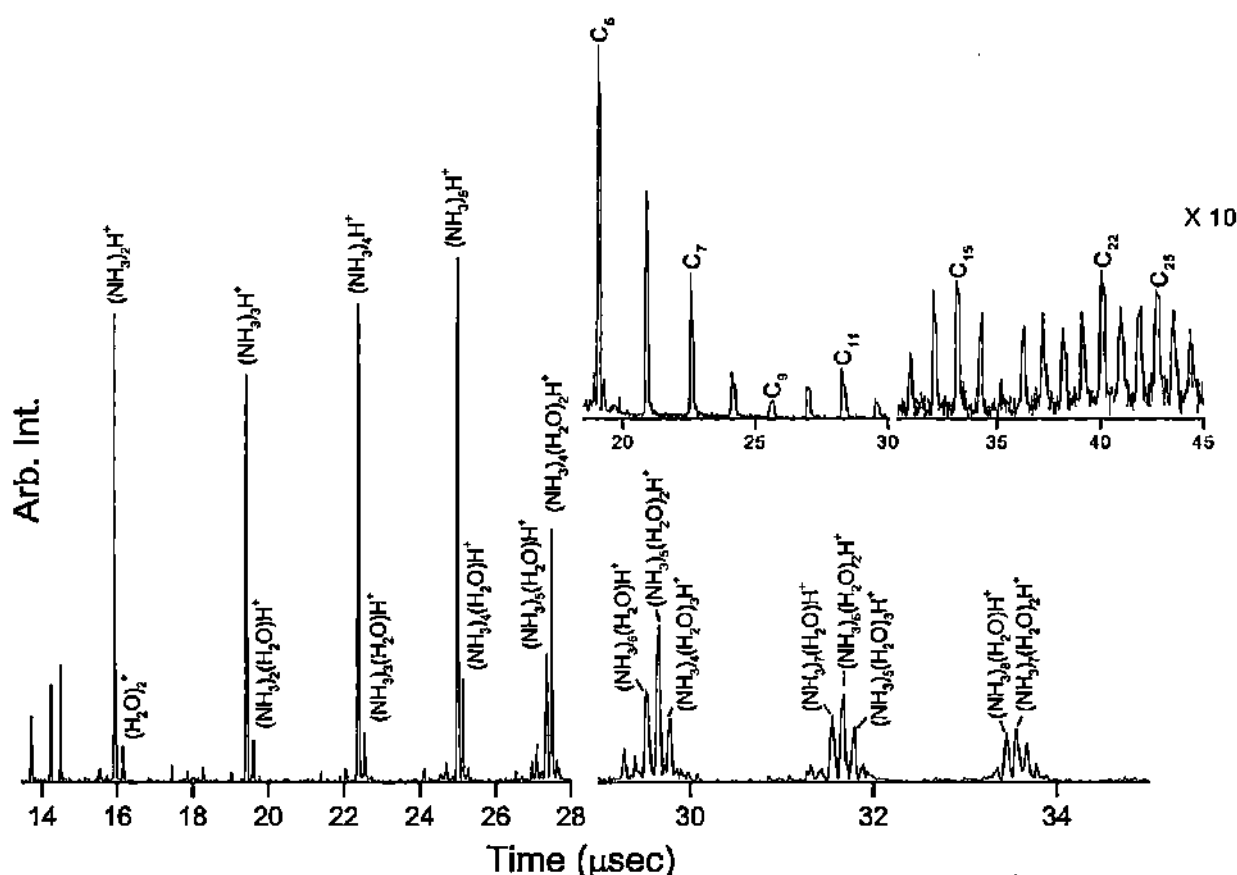

Fig. 5.1 Time-of-flight mass spectrum of protonated ammonia clusters $(NH_3)_nH^+$. The intensities of the peaks reach maximum at a NH₃/He ratio of ~ 0.2. The inset shows mass spectrum of carbon clusters produced by laser ablation of graphite in the presence of helium (NH₃/He=0). The spectrum was obtained under the same conditions used to optimize the C-NH₃ interaction (see experimental). When optimized for carbon clusters (delay, 110 µs; vaporization laser, 70 mJ/pulse; ionization laser, 80 mJ/pulse), we obtained high intensity mass peaks for C_n species up to n ≅ 90.

The preference for water attachment beyond $(NH_3)_5H^+$ during intracluster rearrangement has been reported by Nishi et al [19]. Alternatively, the minor peaks may be assigned to doubly protonated ammonia species, which is however, quite unlikely the situation since higher protonation is known to occur only in high nuclearity ammonia clusters [20]. Fortunately, this possible degeneracy in the minor peaks pertains only to the ammonia spectrum (the laser-off condition) and does not cause any difficulty in the assignment of reaction products, as discussed below.

In the laser-on condition and with no ammonia, the carbon cluster spectrum obtained with pure helium as the carrier gas reveals C_n^+ species with n up to 30 (see inset of Fig. 5.1). However, when ammonia is introduced along with He, the spectrum does not show any carbon clusters (even with 1% of ammonia). Instead, we observe several new peaks as shown in Fig. 5.2.
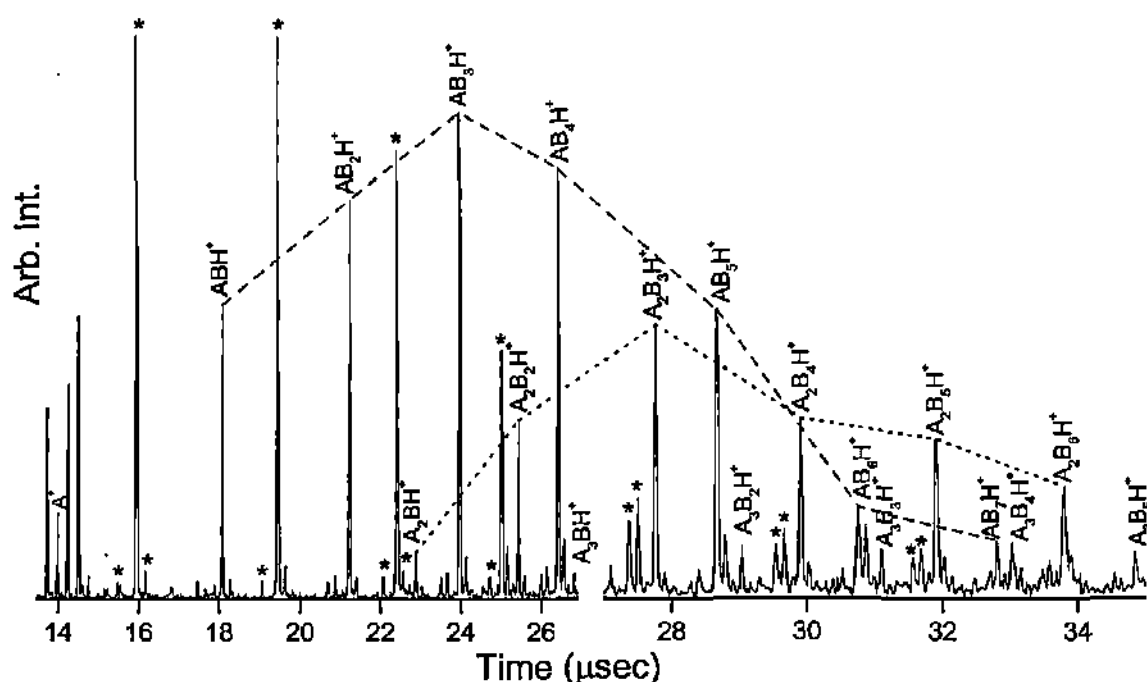

Fig. 5.2 Time-of-flight mass spectrum of $A_mB_nH^+$ cluster species, A = HCN, B = NH_3, $1 \leq m \leq 4$ and $1 \leq n \leq 7$, produced by laser ablation of graphite in presence of NH_3 seeded in helium (NH_3/He ~ 0.2). To guide the eye, the prominent peaks containing HCN monomer and dimer are connected by dashed and dotted lines respectively. Ammonia related peaks common with Fig. 5.1 are denoted by asterisk.

The peak at 27 u is assigned to the HCN^+ species, the series of peaks at 45, 62, 79, 96 u and so on, representing successive addition of up to 7 NH_3 molecules to HCN, corresponding to the series $(HCN)(NH_3)_n H^+$. Ammonia attachment to HCN is indeed not surprising, since such adducts are observed from a jet-cooled admixture [12,13]. The peaks corresponding to $n = 2$, 3 and 4 exhibit relatively high intensity. The other prominent mass series observed is 72, 89, 106, 123 u and so on, corresponding to $(HCN)_2(NH_3)_n H^+$ where $n = 1$ to 6. Here, the prominent peak is one with $n = 3$. In addition to these two series, we also observe the $(HCN)_3(NH_3)_n H^+$ and $(HCN)_4(NH_3)_n H^+$ series, albeit with lower intensity.

Smalley et al. [4] reacted carbon vapor with ammonia seeded in helium and reported the formation of HC_8H, HC_7N, $HC_{10}H$ and HC_9N cyanopolyynes appearing as satellite features to the carbon peaks. This is not, however, the case under the experimental conditions employed in the present study. The low-intensity peaks corresponding to $(HCN)_3(NH_3)H^+$ (mass, 99 u) and $(HCN)_2(NH_3)_4H^+$ (mass, 123 u) could, in principle, be assigned to HC_7N and HC_9N respectively, but we do not see evidence for other related species in the spectrum. Similarly, it can be argued that the main products in Fig. 5.2 cannot result from water-attached species. The assignments are also substantiated by the systematics observed in the mass spectra. It appears that the formation of HCN involves the mechanism given by Eq. 5.1.

The relative populations of the various species with $m = 1$ and 2, and n up to 6 vary with the NH_3/He ratio (see Fig. 5.3). The populations reach maximum values at a NH_3/He ratio of ~ 0.2. It appears that cluster formation is suppressed at low concentrations of NH_3 (NH_3/He < 0.2) primarily due to the dilution effect, while there is a gradual decay due to decreased thermalization in the presence of excess NH_3. In the laser-off experiments, the intensities of ammonia clusters were also highest when the NH_3/He ratio was ~ 0.2, thereby confirming optimal cooling
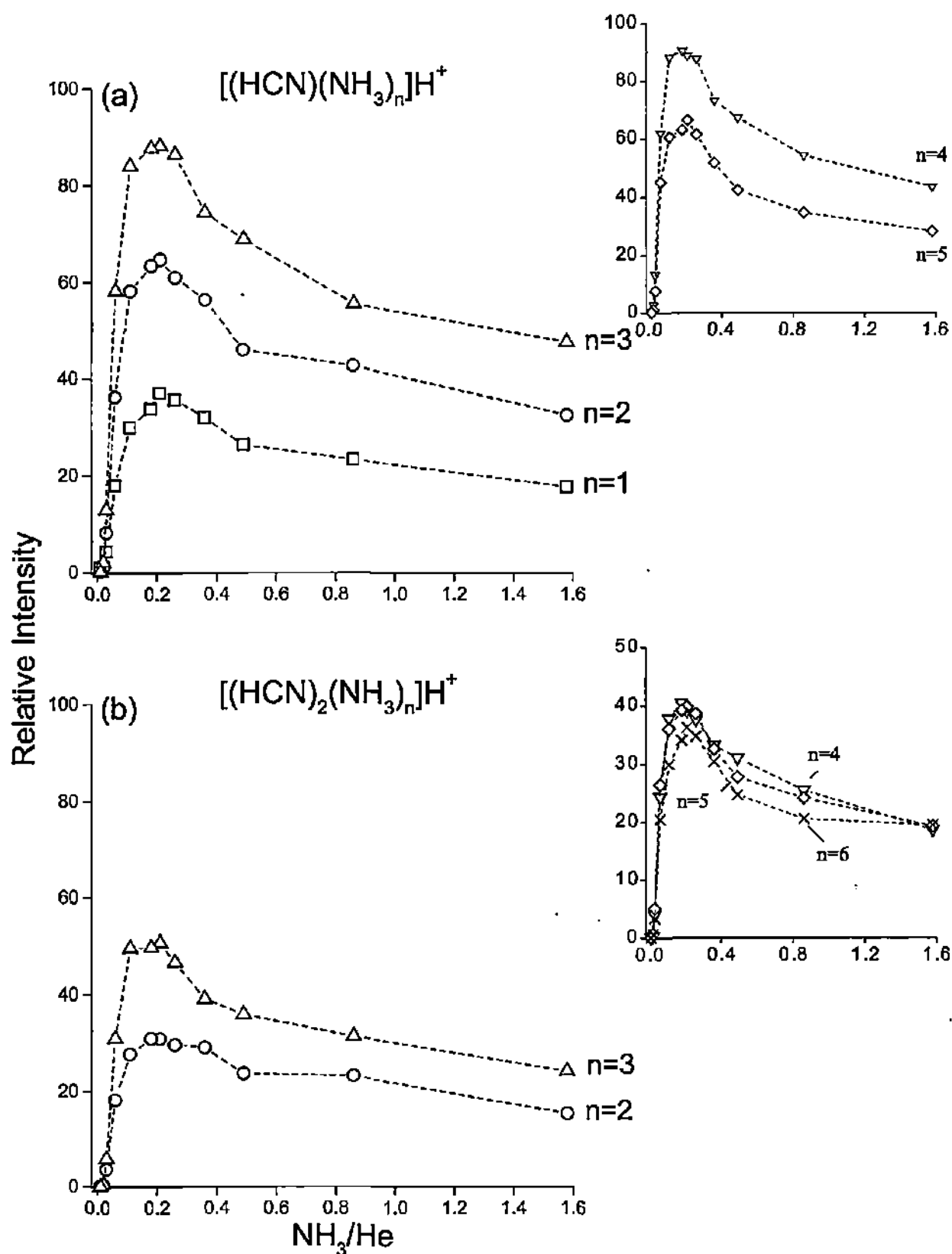
Fig. 5.3 Plots showing the variation in the intensity of $(HCN)_m(NH_3)_nH^+$ with NH_3/He, (a) m=1 with $1 \leq n \leq 5$, (b) m=2 with $2 \leq n \leq 6$; n = 1(squares), 2(circles), 3(uptriangle), 4(down triangle), 5(diamond) and 6(cross). For the sake of clarity, some of the curves are presented in the insets.

at this ratio. We notice from Fig. 5.3a that for the $(HCN)_1(NH_3)_nH^+$ species, the population is particularly high for n = 3 and 4, and lowest for n = 1. Figure 5.3b shows similar plots for the $(HCN)_2(NH_3)_nH^+$ species. Thus, species with m = 1, n = 3, 4 and with m = 2, n = 3 or in general those with n+m close to 5, exhibit higher intensities suggesting a greater stability.

5.4 Gaussian calculations

We have performed RHF/6-31G(d) level calculations using the GAUSSIAN 98W [21] package for the medium sized systems, $(HCN)_m(NH_3)_nH^+$ (m = 1, 2 and n up to 4) and $(NH_3)_nH^+$ (n up to 5). Our results on the $(NH_3)_nH^+$ species corroborate well with those of Kassab et al. [22] who used the RHF method with 4-31G+3S basis set. Calculations on $(HCN)_m(NH_3)_nH^+$ species were performed starting with an input geometry where a NH_4^+ ion is centrally located and surrounded by HCN and NH_3 molecules. Given the nature of the molecules present in the coordination shell of the NH_4^+ ion, both the proton affinity and dipolar forces are expected to come into play [15]. The proton affinity of NH_3 is 854 kJ/mole while that of HCN is somewhat lower, 717 kJ/mole. On the other hand, the dipole moment of HCN is much higher (3.2 Debye) compared to that of NH_3 (1.77 Debye).

The optimized geometries and energies of some of the initial members of the $(HCN)_m(NH_3)_nH^+$ species are shown in Fig. 5.4 and those for $(NH_3)_nH^+$ species in Fig. 5.5. The geometry-optimized structure for $(HCN)(NH_3)H^+$ gives an intermolecular H$\cdots$N hydrogen bond distance of 1.88 Å and an angle of 179.9°, as shown in Fig. 5.4a. The complexation energy of the cluster species was estimated to be 20.6 kcal/mole, by subtracting its total energy from the sum-total of energies of the NH_4^+ ion and the HCN molecule, as given by equation (5.2)
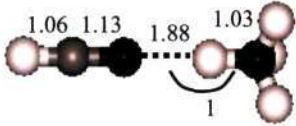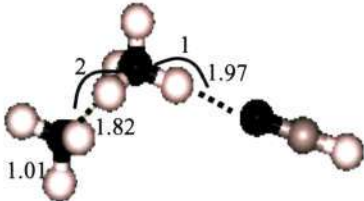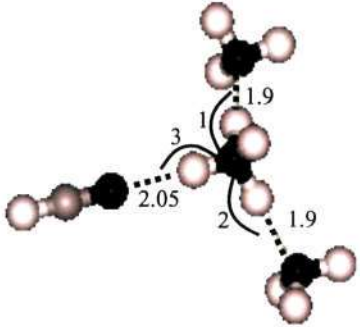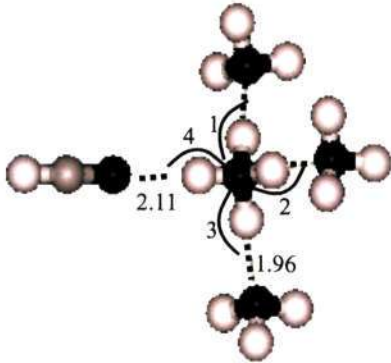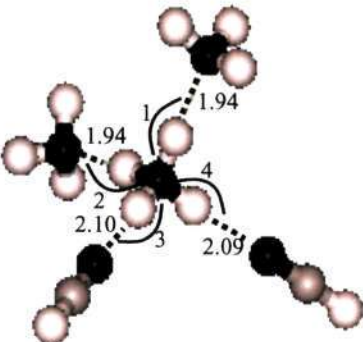
	Cluster Composition		Optimized structure	H-bond angles	Total Energy, E (A.U.)
	m	n			
(a)	1	1	1.06 1.13 1.88 1.03 ∠1	∠1 = 179.9°	-149.44
(b)	1	2	2 1 1.97 1.82 1.01	∠1 = 177.5° ∠2 = 179.9°	-205.66
(c)	1	3	1.9 3 1 2.05 2 1.9	∠1 = 179.0° ∠2 = 179.0° ∠3 = 178.0°	-261.87
(d)	1	4	4 1 2.11 3 2 1.96	∠1 = 179.2° ∠2 = 179.2° ∠3 = 179.2° ∠4 = 180.0°	-318.08
(e)	2	3	1 1.94 1.94 4 2 2.10 3 2.09	∠1 = 179.0° ∠2 = 178.0° ∠3 = 178.3° ∠4 = 178.1°	-354.76

Fig. 5.4 Optimized geometric parameters for five of the $(HCN)_m(NH_3)_nH^+$ species obtained at RHF/6-31 G(d) level of theory using Gaussian 98W. Bond lengths are reported in angstroms, angles in degrees and total energies in atomic units (1 A. U. = 627.51 kcal/mole).

Cluster species	Optimized structure	H-bond angles	Total Energy, E (A.U.)
(a) $(NH_4)^+$	1.01	$\angle 1 = 109.5°$	-56.53
(b) $(NH_4)^+(NH_3)$	1.06 1.76	$\angle 1 = 179.9°$	-112.76
(c) $(NH_4)^+(NH_3)_2$	1.04 1.85	$\angle 1 = 178.9°$	-168.97
(d) $(NH_4)^+(NH_3)_3$	1.93 1.03	$\angle 1 = 180.0°$	-225.19
(e) $(NH_4)^+(NH_3)_4$	1.99 1.02	$\angle 1 = 180.0°$	-281.39

Fig. 5.5 Geometry optimized structures of five of the $(NH_3)_nH^+$ species obtained at RHF/6-31 G(d) level of theory using Gaussian 98W. Bond lengths are reported in angstroms, angles in degrees and total energies in atomic units.

136

$$E_{comp} [HCN(NH_3)H^+] = E_{tot} [(NH_3)H^+] + E_{tot} [HCN] - E_{tot} [HCN(NH_3)H^+] \qquad (5.2)$$

Mayer [23] has reported a complexation energy value of 20.3 kcal/mole based on the (MP2/6-31+G(d)) method. The corresponding energy for the $(NH_3)_2H^+$ species (Fig. 5.5b) is somewhat higher (26.3 kcal/mole).

In $(HCN)(NH_3)_2H^+$ (Fig. 5.4b), the N-H...N hydrogen bond along HCN deviates considerably from linearity (177.5°) and the bond distance increases to 1.97 Å as against 1.88 Å in $(HCN)(NH_3)H^+$ (Fig. 5.4a). The H···N distance along the NH_3 molecule has a more favorable value of 1.82 Å, owing to its relatively higher proton affinity. The incremental complexation energy of this species, obtained by subtracting its total energy from the total energy of the $(HCN)(NH_3)H^+$ species and NH_3 molecule, is 22.0 kcal/mole. This energy is comparable to the corresponding value for $(NH_3)_3H^+$ (21 kcal/mole) (Fig. 5.5c). In $(HCN)(NH_3)_3H^+$ (Fig. 5.4c), the NH_4^+ ion is solvated by HCN on one H-bonding site and by two NH_3 molecules on the other two H-bonding sites resulting in further relaxation of the solvent shell. The incremental complexation energy in this case is 18.1 kcal/mole which is slightly higher compared to that in $(NH_3)_4H^+$ (17.2 kcal/mole) (Fig. 5.5d).

With the addition of the fourth NH_3, the first solvation shell of the NH_4^+ ion becomes complete (Fig. 5.4d). The H-bonds between NH_4^+ ion and the NH_3 molecules further increase to 1.96 Å and so does the distance involving HCN (2.11 Å) and are quite linear. Its incremental complexation energy is found to be 15 kcal/mole, which may be compared with that of the $(NH_3)_5H^+$ species (14.4 kcal/mole) (Fig. 5.5e). The completion of the solvation shell around NH_4^+ explains the high intensity observed for this species in the mass spectrum (Fig. 5.2).

It is interesting to examine how the presence of the HCN molecule in the solvation shell of NH_4^+ influences the complexation energy of the system. In Fig. 5.6, we have plotted the incremental complexation energy due to added NH_3 for both $(HCN)(NH_3)_nH^+$ and $(NH_3)_nH^+$ species. For the sake of comparison, we have shown the values obtained by Kassab et al. [22] for $(NH_3)_nH^+$. The $(NH_3)_nH^+$ system, in both cases, shows a monotonic decrease in the incremental complexation energy with the successive additions of NH_3 molecules to $NH_4^+(NH_3)$.
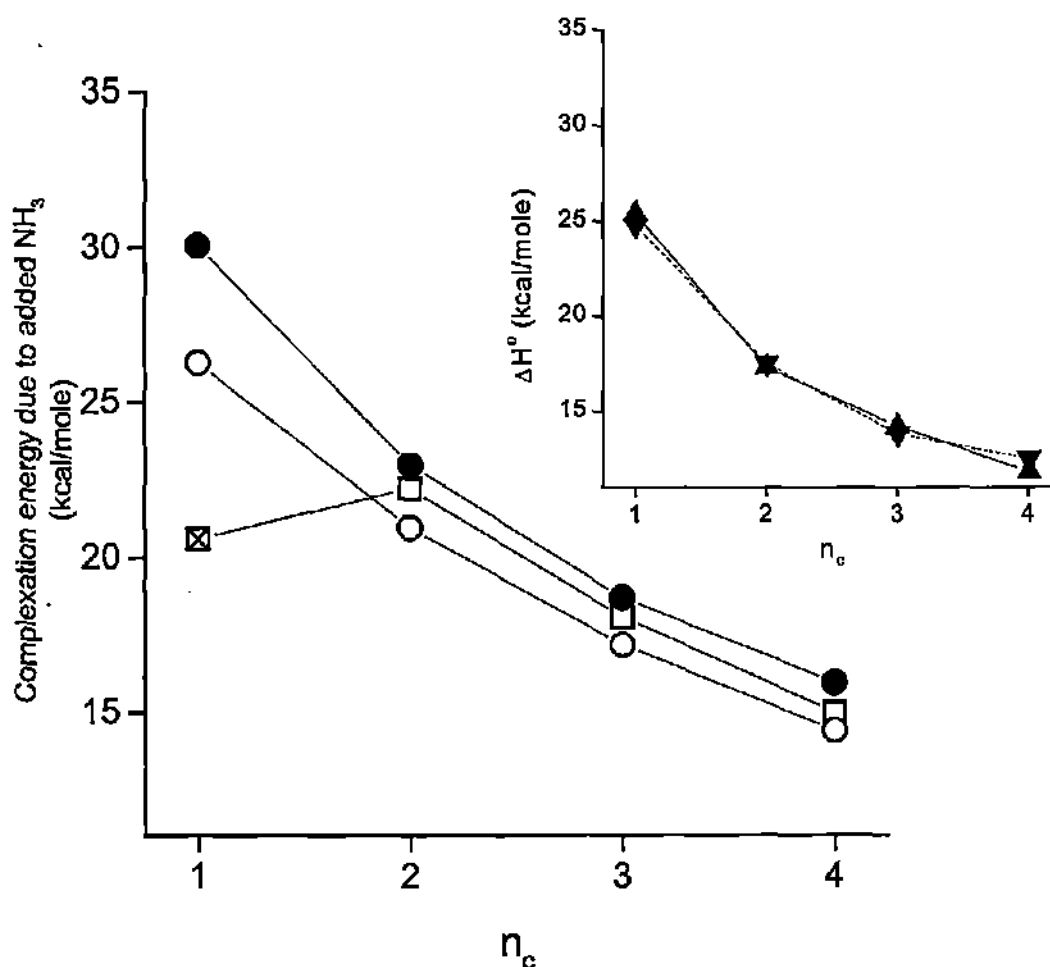
Fig. 5.6 The variation in the average complexation energy per NH_3 with the number of molecules, n_c, present in the solvent shell of NH_4^+. Circles represent $(NH_3)_nH^+$ species (n=2 to 5) and squares, the $(HCN)(NH_3)_nH^+$ species (n=1 to 4). The crossed square stands for HCN in the first coordination site. The pure ammonia species have been optimized using the same method. The values obtained by Kassab et al [22] are shown (filled circles) for the sake of comparison. Inset shows experimentally measured enthalpy values for $(NH_3)_nH+$: uptriangles, [24]; downtriangles, [25].

This stepwise decrease has been explained as due to increased charge dispersion and dielectric shielding in high nuclearity clusters [22]. We have also compared the values with the corresponding experimentally measured enthalpies, ΔH° [24, 25] (see inset of Fig. 5.6), to demonstrate similar trends as the calculated values. The energy required to complex a HCN molecule with the NH_4^+ ion is much lower (20.6 kcal/mole) than that in the case of an NH_3 molecule (26.3 kcal/mole), primarily due to the lower proton affinity of the former. Interestingly, the complexation energy increases to 22.2 kcal/mole with the addition of an NH_3 molecule to $(HCN)(NH_3)H^+$ (at the second site of NH_4^+). Such an increase could be related to weaker dielectric shielding in the presence of the HCN molecule. With further additions of NH_3, the energy follows a similar trend as that of the pure ammonia system. The $(HCN)_n(NH_3)_mH^+$ species being more polarized, the stabilization energies are also somewhat higher ($\sim$1.7 kcal/mole). Thus, it is clear that the solvent preference of ammonium ion changes as the cluster size increases, just as in water-amine ion clusters [26].

In Fig. 5.4e, we have shown the optimized structure of $(HCN)_2(NH_3)_3H^+$ as an example of the cluster species containing two HCN molecules. Here, the NH_4^+ ion is solvated by two HCN molecules and two NH_3 molecules, on the four available H-bonding sites. The solvent shell being complete, its mass peak is associated with a high intensity (Fig. 5.2). The proton affinity of NH_3 molecules being greater than that of HCN, the NH_3 molecules get closer to the central NH_4^+ ion with H-bond distances of 1.94 Å (angle, $\sim$180°) than the HCN molecules (2.09 Å and 2.10 Å). The incremental complexation energy that results following the addition of HCN to $(HCN)_1(NH_3)_3H^+$ is 9.4 kcal/mole. It is to be noted that the complexation energies of the two magic nuclearity clusters differ by about 5.6

kcal/mole indicating that $(HCN)_2(NH_3)_3H^+$ is slightly more stabilized than $(HCN)_1(NH_3)_4H^+$.

5.5 Conclusions

We have examined the reaction products formed by interaction of carbon vapor generated by laser ablation of graphite with NH_3 seeded in He. The presence of even a small concentration of ammonia (~1%), inhibits the formation of carbon clusters and leads to the formation of cluster species of the type $(HCN)_m(NH_3)_nH^+$ along with the $(NH_3)_nH^+$ clusters. The populations of these products reach maximum values for a NH_3/He ratio of ~ 0.2 implying that there is a balance between the adiabatic cooling provided by helium and the reactivity of ammonia. The cluster species with $n+m \sim 5$, corresponding to fully coordinated NH_4^+ ions, are the most preponderant species as one would expect intuitively. Ab-initio molecular orbital calculations show that the complexation energy afforded by addition of each NH_3 to the $HCN-NH_4^+$ cluster decreases after the first addition.

References

[1] C. Lifshitz, *Int. J. of Mass Spectrom.* 200, 423 (2000).

[2] Q. L. Zhang, S.C. O'Brien, Q. Zhang, Y. Liu, R. F. Curl, H. W. Kroto and R. E. Smalley, *J. Phys. Chem.* 90, 525 (1986).

[3] J. A. Zimmerman, J. R. Eyler, S. B. H. Bach and S. W. McElvany, *J. Chem. Phys.* 94, 3556 (1991).

[4] J. R. Heath, Q. Zhang, S. C. O'Brien, R. F. Curl, H. W. Kroto and R. E. Smalley, *J. Am. Chem. Soc.* 109, 359 (1987).

[5] D.B. Geohegan, *'Laser Ablation: Mechanisms and Applications'* Springer: Heidelberg (1991).

[6] J. Hermann, A. L. Thomann, C. Boulmer-Leborgne, B. Dubreil, M. L. De Giorgi, A. Luches and I. N. Mihalescu, *J. Appl. Phys.* 77, 2928 (1995).

[7] L. G. Coccia, T. G. Tyrrel and I. W. Boyd, *Appl. Surf. Sci.* 109/110, 413 (1997).

[8] S. Acquaviva, A. P. Caricato, M. L. De Giorgi, G. Dinescu, A. Luches and A. Perrone, *J. Phys. B: At. Mol. Opt. Phys.* 30, 4405 (1997).

[9] C. Vivien, J. Hermann, A. Perrone and C. Boulmer-Leborgnem, *J. Phys. D:Appl. Phys.* 32, 518 (1999).

[10] D. W. McPherson, M. L. McKee and P. B. Shevlin, *J. Am. Chem. Soc.* 105, 6493 (1983).

[11] P. B. Shevlin, D. W. McPherson and P. Melius, *J. Am. Chem. Soc.* 105, 488 (1983).

[12] G. T. Fraser, K. R. Leopold, D. D. Nelson Jr., A. Tung and W. Klemperer, *J. Chem. Phys.* 80, 3073 (1984).

[13] R. S. Ruoff, T. Emilsson, C. Chuang, T. D. Klots and H. S. Gutowsky, *J. Chem. Phys.* 93, 6363 (1990).

[14] S. Maruyama, L. R. Anderson and R. E. Smalley, *Rev. Sci. Instrum.* 61, 3686 (1990).

[15] A. O. Echt, P. D. Dao, S. Morgan and A. W. Castleman, Jr., *J. Chem. Phys.* 82, 4076 (1985).

[16] S. Wei and A. W. Castleman Jr., *Int. J. of Mass Spectrom. Ion Processes* 131, 233 (1994).

[17] K. Fuke, R. Takasu and F. Misaizu, *Chem. Phys. Lett.* 229, 597 (1994).

[18] Th. Freudenberg, W. Radlolf, H.-H. Ritze, V.Stert, F. Noack and I.V. Hertel, *Z. Phys. D.* 41, 267 (1997).

[19] H. Shinohara and N. Nishi, *Chem. Phys. Lett.*, 141, 292 (1987).

[20] D. C. Sperry, J. I. Lee and J. M. Farrar, *Chem. Phys. Lett.* 304, 350 (1999).

[21] M. J. Frisch, GAUSSIAN 98 (Rev. A.1); Gaussian, Inc., Pittsburgh, PA, (1998).

[22] E. Kassab and E. M. Evleth, *J. Am. Chem. Soc.* 109, 1653 (1987).

[23] P. M. Mayer, *J. Phys. Chem. A* 103, 5905 (1999).

[24] I. N. Tang and A. W. Castleman Jr. *J. Chem. Phys.* 62, 4576 (1975).

[25] J. D. Payzant, A. J. Cunningham and P. Kebarle *Can. J. Chem.* 51, 3242 (1973).

[26] A. J. Stace, *J. Amer. Chem. Soc.* 106, 2306 (1984).

6. Reactive laser ablation of oxides of group 13 and 14 elements in N_2 / NH_3 seeded in He

SUMMARY

Reactive laser ablation of oxides of group 13 elements, B_2O_3, Al_2O_3 and Ga_2O_3 and of group 14 elements, SiO_2 and GeO_2, in pure form as well as in mixture with carbon, has been carried out in the presence of nitrogen or ammonia in a pulsed supersonic jet of helium. The product species have been analyzed using time-of-flight mass spectrometry. *Nitridic species such as* $Si_2N_y^+$ *(y $\leq$ 5) and* GeN_y^+ *(y $\leq$ 4)* are formed in nitrogen while $B_xN_y^+$ (x $\leq$ 2 and y $\leq$ 4) and GaN^+ species require the presence of carbon as well. Oxynitride species predominate in the presence of NH_3 in the case of B, Al and Ge but the nitride species are prominent in the case of Si. Interestingly, in the presence of both carbon and NH_3 (or N_2), nitride species dominate in the case of Ga. With Al_2O_3, $AlON^+$ is the abundant species under all the reaction conditions studied. B_2O_3, SiO_2 and GeO_2 form carbidic species on reaction with carbon in presence of helium jet.

6.1 Introduction

Nitrides of group 13 elements such as B, Al and Ga are all, important materials of technological interest. Thus, BN, which has a layered structure like graphite, has many attributes - a lubricant, a hard material and a good dielectric [1], while AlN and GaN, particularly the latter, are important electronic materials. It is noteworthy that GaN is a wide-gap semiconductor, which finds immense use in producing a variety of lasers and is likely to be used in spintronics and power transistors [2]. Similarly, nitrides of group 14 elements such as C and Si are being investigated widely for potential applications. Several workers have recently synthesized nitrides of group 13 and 14 elements especially in the form of nanowires or nanotubes. An important commonality in the method of synthesis employed for most of these nitrides is the use of oxide precursors. Thus, boron nitride has been synthesized by the reaction of boric oxide (B_2O_3) with ammonia or nitrogen in the presence of carbon [3,4]. Similarly, AlN can be prepared using oxide precursors in the presence of ammonia [5] while GaN is produced from gallium sub-oxide (GaO_x) obtained by reacting Ga_2O_3 with ammonia [6,7]. Silicon oxynitride (Si_2N_2O) and Si_3N_4 are obtained by the reaction of SiO_2 or silicon sub-oxide (SiO_x) with ammonia or nitrogen [8,9]. These reactions are all facilitated by the presence of carbon. It is therefore of interest to find out the mechanism of formation of nitrides, oxynitrides and carbonitrides by the reaction of the corresponding oxides with nitrogen or ammonia. Also of interest is to understand the reactions of the oxides in the presence of carbon. In other words, the pertinent question to be answered is whether nitridic or oxynitridic species of the various metals are formed in the vapor phase on the reaction of the metal oxides with nitrogen or ammonia while carbon may be present or absent along with the oxide.

Laser ablation is an effective way to bring about reactions involving refractory materials [10]. It has been employed to form nitridic species of group 13 elements such as boron [11], aluminum [12] and gallium [13] as well as of group 14 elements such as silicon [14] and germanium, in the presence of ammonia or nitrogen. Carbidic species of boron [15] and silicon [16] have also been obtained by ablating the elements in the presence of carbon or methane. We have carried out reactive laser ablation of the powders of the oxides of group 13 elements, namely B_2O_3, Al_2O_3 and Ga_2O_3 and of group 14 elements, SiO_2 and GeO_2 in the presence of nitrogen or ammonia in a pulsed helium supersonic jet. We have also performed a series of experiments wherein an intimate mixture of the oxides with carbon is made to react with nitrogen or ammonia and have analyzed the reaction products by time-of-flight mass spectrometry.

6.2 Experimental

Boric oxide (B_2O_3), alumina (Al_2O_3 activated, α-form), gallium oxide (Ga_2O_3) and germanium oxide (GeO_2) were procured from Aldrich (purity > 99.5%) and amorphous silica (SiO_2) was prepared in the laboratory by the hydrolysis of tetraethylorthosilicate (TEOS). Nitrogen, ammonia and helium of high purity (99.999%) were used for the experiment. The reactant gas, nitrogen or ammonia was introduced into the sample cell along with carrier gas He (99.999%) through the pulsed supersonic valve, at a total back-pressure of ~ 3 atmospheres (see schematic in Fig. 6.1). A laser-traced spiral groove on a stainless steel target rod was first machined to a depth of 0.3 mm with 0.7 mm pitch. The oxide powder sample was ground and mixed with distilled water to form a thin paste which was filled into the groove. This way, the vaporization laser was incident only on the powder-filled
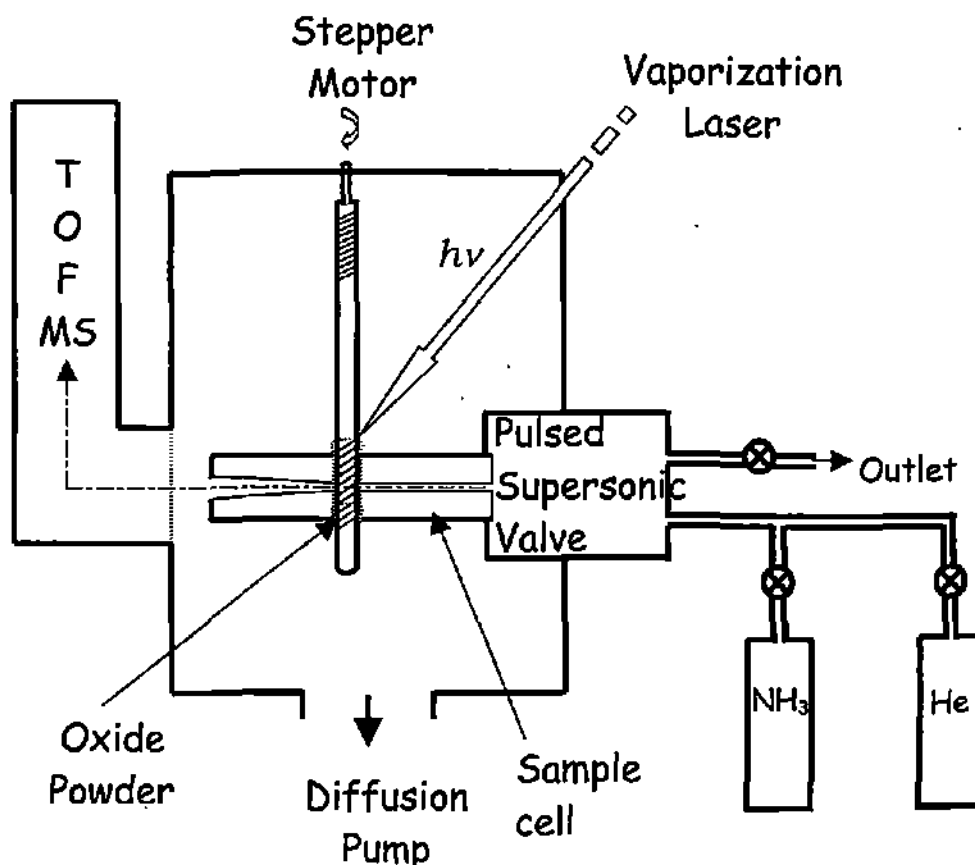
Fig. 6.1 A schematic of the reactive laser ablation experimental set-up.

groove. To perform the ablation of the oxide powder in presence of graphite, a grooved graphite rod was machined in a similar fashion and the powder sample was painted onto it. Once loaded, the sample lasted for about 7 minutes during ablation. The power of the vaporization laser was ~ 100 mJ/pulse. The delay of the laser with respect to the peak of the current pulse driving the pulsed valve spring was typically 90μsec.

6.3 Results and discussion

Interaction of nitrogen with B_2O_3, Al_2O_3 and Ga_2O_3

The TOF mass spectra obtained during the reactive ablation of B_2O_3, Al_2O_3 and Ga_2O_3 in N_2 are shown in Fig. 6.2. Ablation of B_2O_3 in presence of supersonic jet of N_2 in helium results in mass peaks at 98 and 196 u (Fig. 6.2a), which are assignable to species of the type $(B_2O_3)N_2^+$ and $(B_2O_3)_2N_4^+$, respectively.
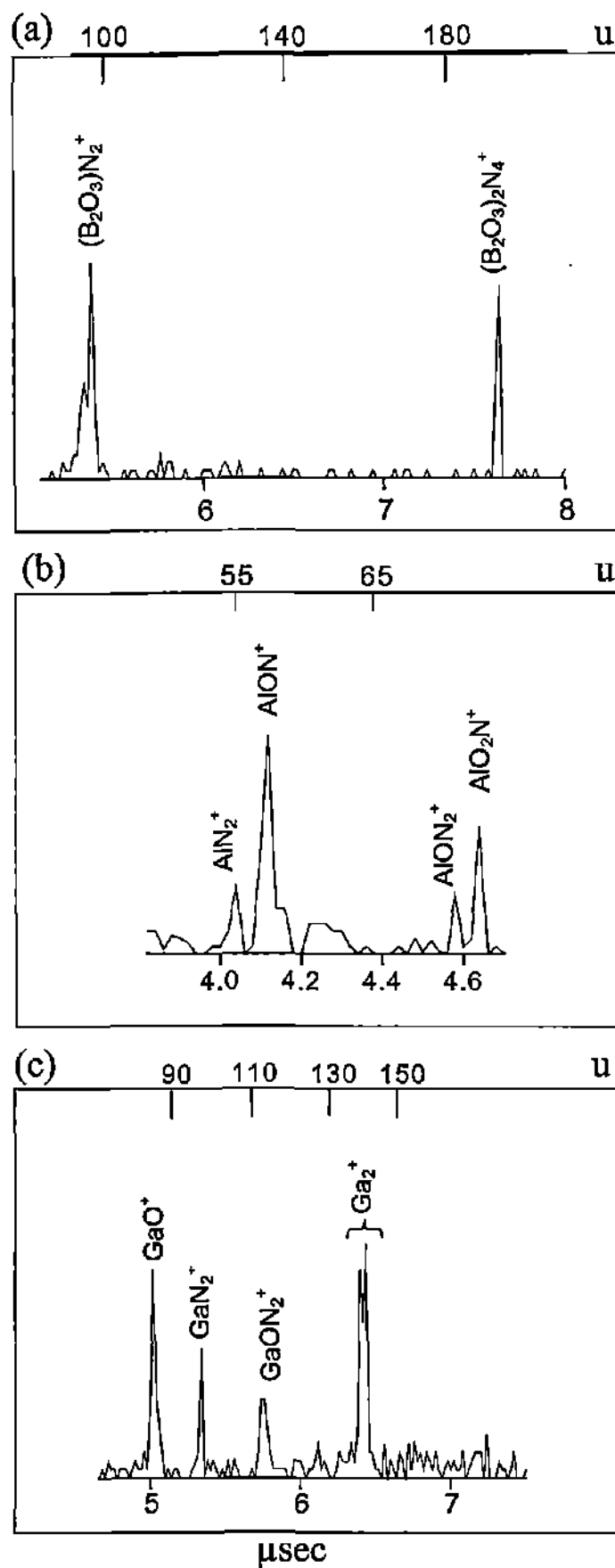
Fig. 6.2 Time-of-flight mass spectra of the cluster species obtained by laser ablating group 13 oxides in N_2-He mixture, (a) B_2O_3, (b) Al_2O_3 and (c) Ga_2O_3.

These species correspond to the most abundant boron isotope (B, 11u). Thus, boric oxide does not seem to dissociate in the presence of nitrogen, instead, it forms molecular adducts with it. We find that the relative populations of these species are about a tenth of the parent B_2O_3 species. The mass spectrum obtained by ablating Al_2O_3 in the presence of nitrogen (Fig. 6.2b) shows peaks at 55, 57, 71 and 73 u, which are assigned to AlN_2^+, $AlON^+$, $AlON_2^+$ and AlO_2N^+ species, respectively. The $AlON^+$ species exhibits the highest intensity with its relative abundance being about 6% with respect to the AlO^+ species. Gallium oxide under similar conditions is not very reactive and produces a spectrum (Fig.6.2c) with peaks of smaller intensities (abundance ~ 2% with respect to Ga^+ species). These are assigned to GaO^+ (85 u), GaN_2^+ (97 u) and $GaON_2^+$ (113 u), the species corresponding to the most abundant gallium isotope (Ga, 69 u). Dimers of the two isotopes of Ga are seen at 138 and 142 u, respectively. We observe that for Al_2O_3 and Ga_2O_3, the dissociated metal and metal oxide species attach to N_2 or N, while B_2O_3 attaches molecularly to N_2 or N_4. However, N attachment directly to the metal species does not occur and accordingly BN^+, AlN^+ and GaN^+ are not observed. Thus, oxides of group 13 elements exhibit varying reactivity when ablated in the presence of nitrogen.

Interaction of ammonia with B_2O_3, Al_2O_3 and Ga_2O_3

The ablation of group 13 oxides was also carried out in the presence of a supersonic jet of NH_3 in helium (Fig. 6.3). The reactive ablation of B_2O_3 produces mass peaks at 63, 65 and 71 u which are assignable to B_3ON^+, $B_3O_2^+$ and $B_2O_3H^+$, respectively (Fig. 6.3a), with the first species having the highest population of 58% with respect to the B^+ peak. It is clear that B_2O_3 seems to dissociate partially in the presence of ammonia. The mass spectrum in the case of Al_2O_3 (Fig. 6.3b) gives peaks at 57 and 114 u corresponding to $AlON^+$ and $Al_2O_2N_2^+$ with nearly equal
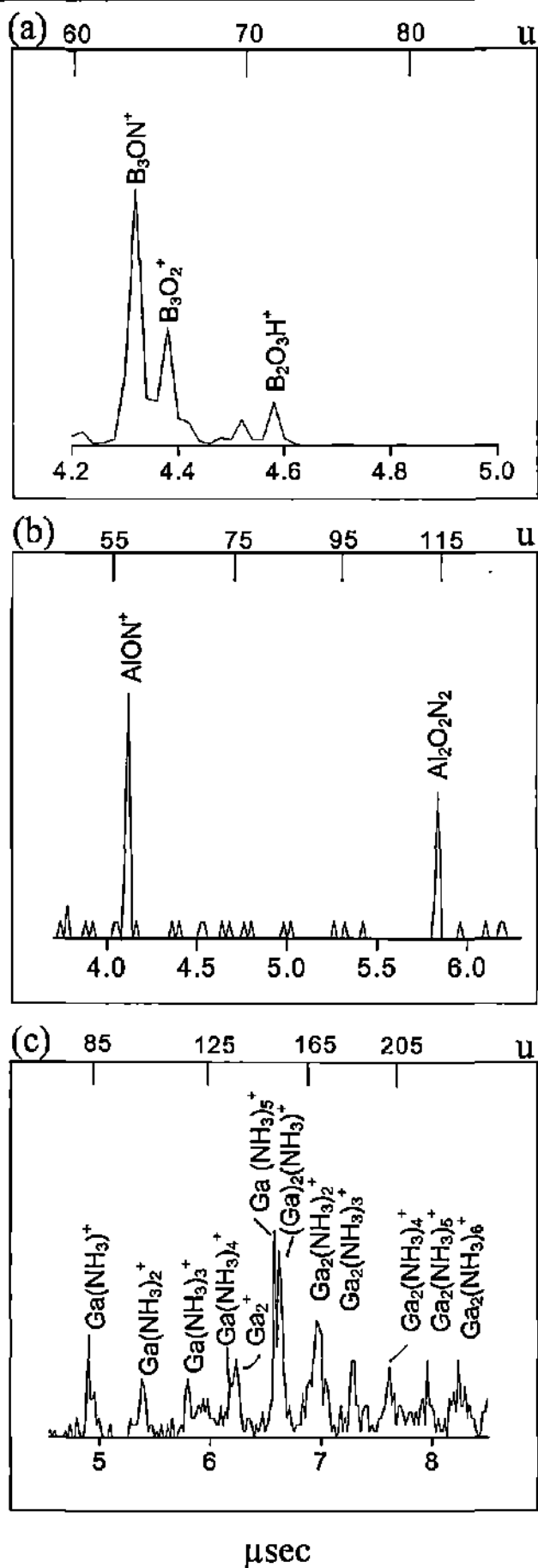
148

Fig. 6.3 Time-of-flight mass spectra of the cluster species obtained by laser ablating group 13 oxides in NH_3-He mixture, (a) B_2O_3, (b) Al_2O_3 and (c) Ga_2O_3. The H^+ attachment to some species comes from the ambient in the mass spectrum.

populations, ~ 4% with respect to AlO^+. The oxynitride species found here are similar to those seen during the ablation of Al_2O_3 with N_2 (Fig. 6.2b). In the case of reactive ablation of Ga_2O_3 (Fig. 6.3c), many intense mass peaks are seen which are assigned to species belonging to two different mass series, $Ga(NH_3)_n^+$ (beginning at 86 u, n upto 5) and $Ga_2(NH_3)_n^+$ (beginning at 155 u, n upto 6), the highest abundance being found for $Ga(NH_3)_5^+$ and $Ga_2(NH_3)^+$. Thus, Ga_2O_3 seems to reduce completely in the presence of NH_3 to produce Ga metal, which in turn forms molecular adducts.

Interaction of N_2 and NH_3 with B_2O_3, Al_2O_3 and Ga_2O_3 in the presence of C

Mass spectra were also obtained in the case of reactive ablation of the group 13 oxides supported on carbon, in an atmosphere of nitrogen (Fig. 6.4). In the presence of carbon, B_2O_3 produces nitridic species such as BN^+ (25 u), BN_2^+ (39 u), BN_3^+ (53 u), $B_2N_3^+$ (64 u) and $B_2N_4^+$ (78 u) (Fig. 6.4a), in contrast to molecular adducts in the absence of carbon (see Fig. 6.2a). Among these, BN^+ and BN_2^+ have appreciable intensities of 57% and 127%, respectively, with respect to B^+ species. These observations may be compared with BN_3 and B_2N species obtained by the laser ablation of boron nitride rod in argon stream and also from elemental boron condensed in an Ar/N_2 atmosphere [11]. Interestingly, B_2O_3 and carbon (in absence of nitrogen) produce carbidic species, BC^+ (23 u), $(BC)_2^+$ (46 u) and $(BC)_3^+$ (69 u) (see inset of Fig. 6.4a), along with C_n^+ species. Here, $(BC)_3^+$ is quite predominant. Similar species are known from laser ablation experiments on pressed pellets of boron-graphite mixture [15]. When the B_2O_3/C reaction was carried out in the presence of ammonia, no reactivity was observed and consequently only peaks corresponding to C_n^+ species were prominent. In the case of ablation of Al_2O_3 with carbon in nitrogen atmosphere, mass peaks at 51, 53, 55, 57 and 71 u corresponding

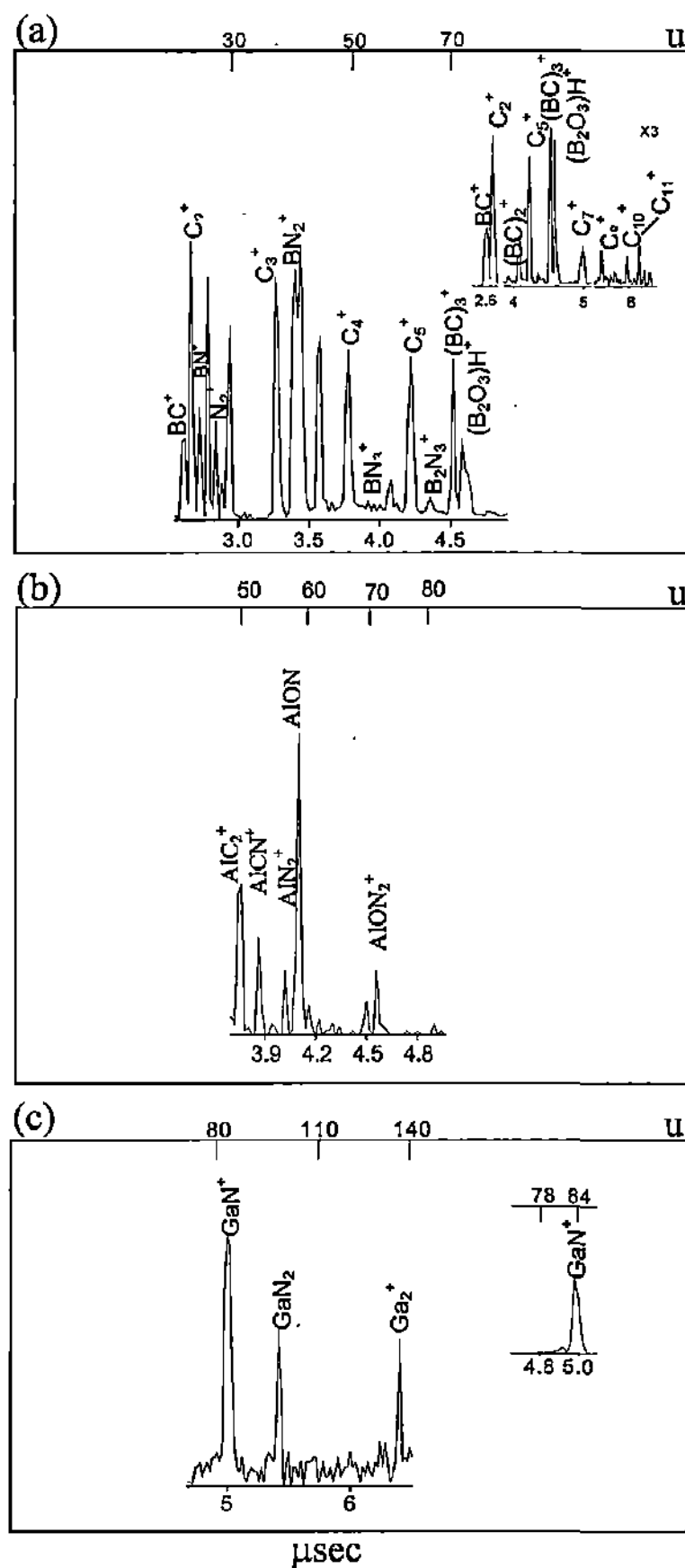Fig. 6.4 Time-of-flight mass spectra of the cluster species obtained by laser ablating group 13 oxides in the presence of carbon and N_2-He mixture, (a) B_2O_3, (b) Al_2O_3 and (c) Ga_2O_3. Inset of (a) shows the product peaks from reaction of B_2O_3 and carbon. Inset of (c) shows the product species from the reaction of Ga_2O_3 + C + NH_3. C_n^+ species are also seen alongside with other peaks.

151

to AlC_2^+, $AlCN^+$, AlN_2^+, $AlON^+$ and $AlON_2^+$, respectively, are observed (Fig. 6.4b). The $AlON^+$ peak has the highest intensity with a relative abundance of 6% with respect to AlO^+ species. $AlCN^+$ and $AlON_2^+$ have relatively smaller intensities of about 2%. It has been reported that AlN_2 along with Al_2N, Al_2N_2, AlN_3 and Al_3N species form, when laser ablated Al atoms are co-deposited with pure N_2 in an argon atmosphere [12]. Similar peaks are observed when ammonia is used instead of nitrogen in the above reaction. Likewise, the ablation of Ga_2O_3 supported on carbon in the presence of nitrogen (Fig. 6.4c), gives small mass peaks assignable to GaN^+ and GaN_2^+. However, GaN^+ is formed with a substantial intensity (~ 17% with respect to Ga^+) in ammonia atmosphere (see inset of Fig. 6.4c). It may be recalled that GaN films have been reported to form by reactive ablation of liquid Ga metal in ammonia [13].

Laser ablation of the oxides results in their dissociation in spite of high lattice energies. However, the dissociated products (the metal and the various sub-oxidic species) may recombine before reaching the detector, depending on their respective reactivity with carbon, oxygen, nitrogen or ammonia, as the case may be. In the case of B_2O_3 (Fig. 6.2a), the dissociated boron is highly reactive to oxidizing agents at high temperatures [17]. It readily recombines with oxygen to form $B_2O_3^+$, which is its most stable oxidic species. In the presence of N_2, it gives rise to adducts of the form $(B_2O_3)N_2^+$ and $(B_2O_3)_2N_4^+$. In the case of Al_2O_3 and Ga_2O_3, the tendency to recombine is less due to their diminishing reactivity with oxygen, especially in the case of Ga (see Fig. 6.2b and 6.2c). Accordingly, the metal (Al and Ga) and the suboxides (AlO and GaO) react with N_2 or N. However, pure AlN or GaN species are not formed. Ammonia, which is more reactive than N_2, is partially able to reduce B_2O_3 and Al_2O_3, giving oxynitride species. The reduction is more facile in the case of Ga_2O_3, and as a result, adducts of the form $Ga(NH_3)_n^+$ and $Ga_2(NH_3)_n^+$ are

formed. In the presence of carbon, B_2O_3 has a higher tendency to react to produce $(BC)_n^+$ species. This is in tune with the known stable boron carbide compounds formed in the bulk phase. Carbon has a somewhat different effect in the case of Al_2O_3 and Ga_2O_3 in that the respective carbides are not formed. In the case of Al_2O_3, $AlON^+$ is the most prominent species in both N_2 and NH_3 atmosphere. For Ga_2O_3, the formation of pure GaN^+ species is promoted in both N_2 and NH_3 atmospheres as oxygen gets driven away in the form of CO or CO_2. In ammonia atmosphere, carbon is not able to bring much reactivity between ammonia and the metal because of its own reaction with the former. Graphite ablation in the presence of ammonia produces adducts of HCN attached to various ammonia clusters as discussed in section 5.3.

Interaction of nitrogen with SiO_2 and GeO_2

The mass spectra in Fig. 6.5 show the reactivity pattern of SiO_2 and GeO_2 in nitrogen atmosphere. In the case of SiO_2 (Fig. 6.5a), we see mass peaks at 70, 71, 85, 99, 113 and 127 u which are assigned to Si_2N^+, Si_2NH^+, $Si_2N_2H^+$, $Si_2N_3H^+$, $Si_2N_4H^+$ and $Si_2N_5H^+$, respectively. Si_2N^+ and Si_2NH^+ peaks have relatively high intensity, $\sim 45\%$ and 32% of Si_2^+ species respectively. The H attachment may arise from the ambient in the cluster apparatus. Si_2N species is also known to form during pulsed laser ablation of Si rod subjected to NO_2 and N_2O [14] as well as from laser ablation of Si_3N_4 [18]. There is some degeneracy in the mass assignments for these peaks, for instance $Si_2N_2H^+$ and $Si_2N_4H^+$ could also be assigned to Si_3H^+ and Si_4H^+. However, the presence of Si_3 and Si_4 seems unlikely as they are not observed when SiO_2 is ablated in pure helium. The mass spectrum of GeO_2 under similar reaction conditions, is shown in Fig. 6.5b. Germanium has several isotopes of approximately equal abundance. We observe that various isotopes of Ge attach to N_x giving rise to
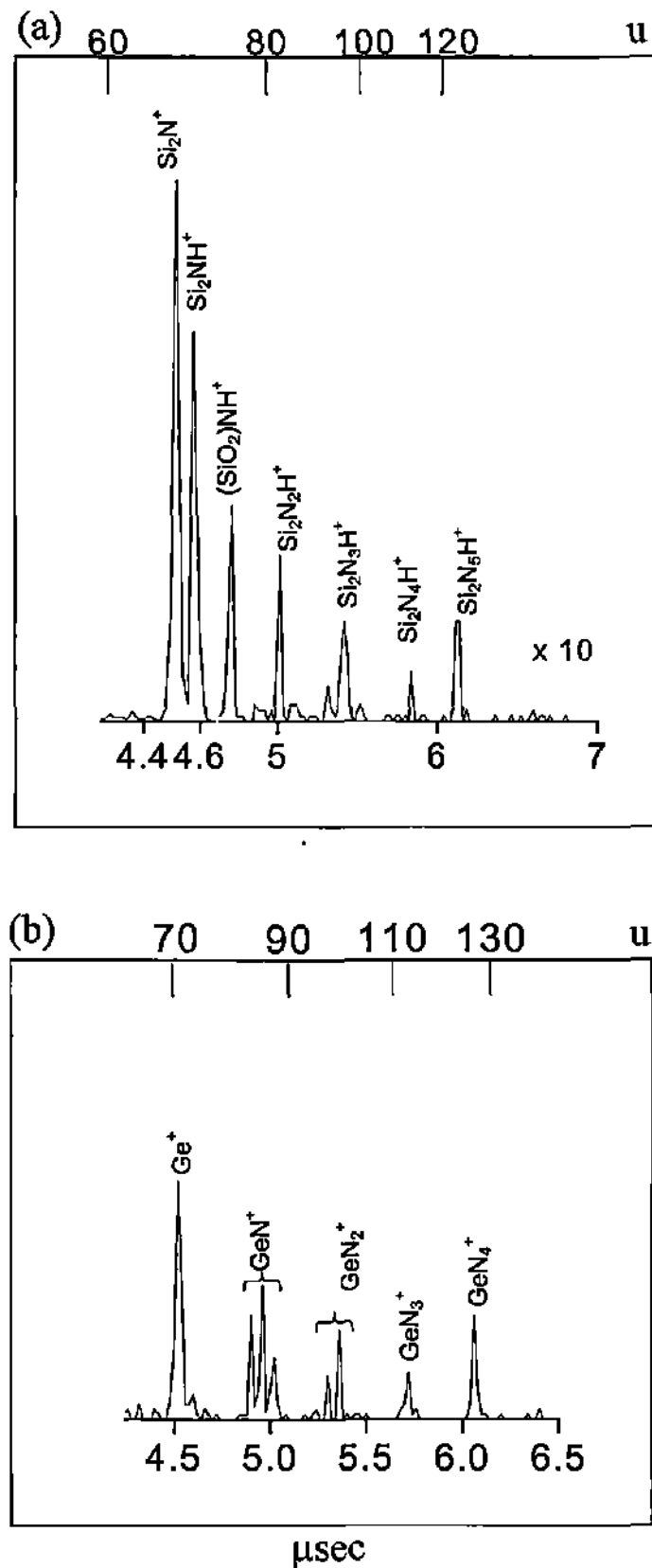
Fig. 6.5 Time-of-flight mass spectra of the cluster species obtained by laser ablating group 14 oxides in N_2-He mixture, (a) SiO_2 and (b) GeO_2. The H^+ attachment to some species comes from the ambient in the mass spectrum.

several low intensity mass peaks of GeN^+, GeN_2^+, GeN_3^+ and GeN_4^+. Various isotopic species put together, the intensity of GeN^+ is comparable to that of Ge^+.

Interaction of ammonia with SiO$_2$ and GeO$_2$

Figure 6.6 shows the mass spectra obtained when the ablation of SiO_2 and GeO_2 was carried out in the presence of NH_3. Reactive ablation of SiO_2 (Fig. 6.6a) shows similar species as in Fig. 6.5a with Si_2N^+ being the strongest peak (~ 32% of Si_2^+). Surprisingly, in the case of GeO_2 (Fig. 6.6b) we observe oxy-nitridic species of the different Ge isotopes, GeO_2N^+ at 116, 118 and 120 u respectively with nearly half the intensity of Ge^+. The GeO_2N^+ peaks may alternatively be also assigned to different isotopic oxynitride species ($GeON_2^+$).

Catenation is an important property of group 14 elements. The tendency to cluster with itself decreases down the group (C » Si > Ge). This may be related to their bond energies, Ge-Ge = 188 kJ/mol, Si-Si = 210-250 kJ/mol, C-C = 356 kJ/mol [19]. In the case of silicon, therefore, the formation of the dimer is favored, which in turn reacts with the nitrogen species to give rise to Si_2N_x type of species. Similar nitridic species are formed in the presence of NH_3 as well. On the other hand, Ge has a relatively lesser tendency to cluster with itself and as a result, monomeric Ge forms various oxynitridic species.

Interaction of N$_2$ and NH$_3$ with SiO$_2$ and GeO$_2$ in presence of carbon

Under similar conditions, SiO_2 and GeO_2 powders were also ablated in the presence of carbon (Fig. 6.7). The reactive ablation of SiO_2, even in the presence of carbon (Fig. 6.7a), gives similar products as in Fig. 6.5a and 6.6a, though the intensities of $Si_2N_2H^+$, $Si_2N_3H^+$ and $Si_2N_5H^+$ are, in this case, comparable to that of Si_2NH^+. However, we have observed that its reactivity with NH_3 is completely
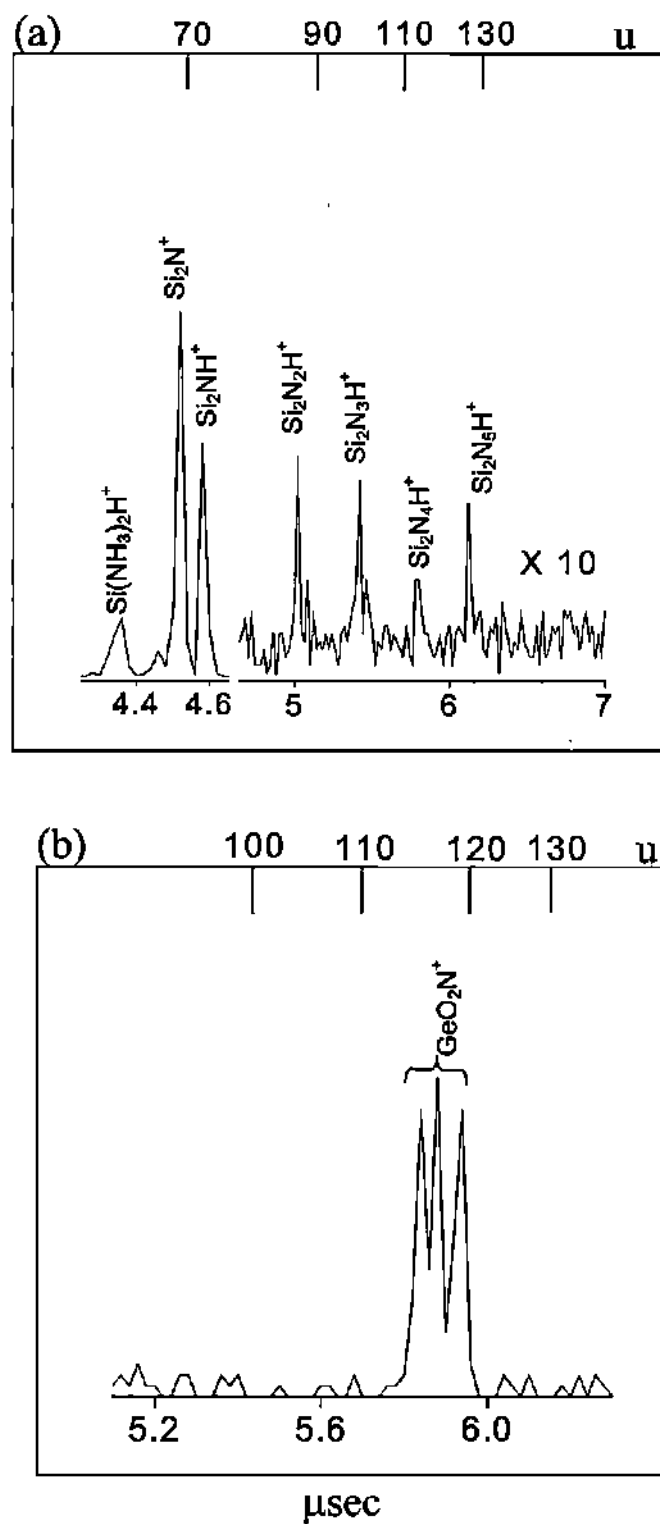
Fig. 6.6 Time-of-flight mass spectra of the cluster species obtained by laser ablating group 14 oxides in NH_3-He mixture, (a) SiO_2 and (b) GeO_2.

suppressed in presence of carbon (similar to the case of B_2O_3). In case of GeO_2, the mass spectrum shows peaks with small intensities assignable to $GeON^+$, GeC_2N^+, $GeON_2^+$, $GeC_2N_2^+$ and $Ge_2N_2^+$ (abundance ~ 3%). The presence of carbon during reactive ablation with N_2 does not seem to enhance the formation of GeN instead $GeC_xN_y^+$ or $GeON_y^+$ type species are formed along with carbon clusters. A similar
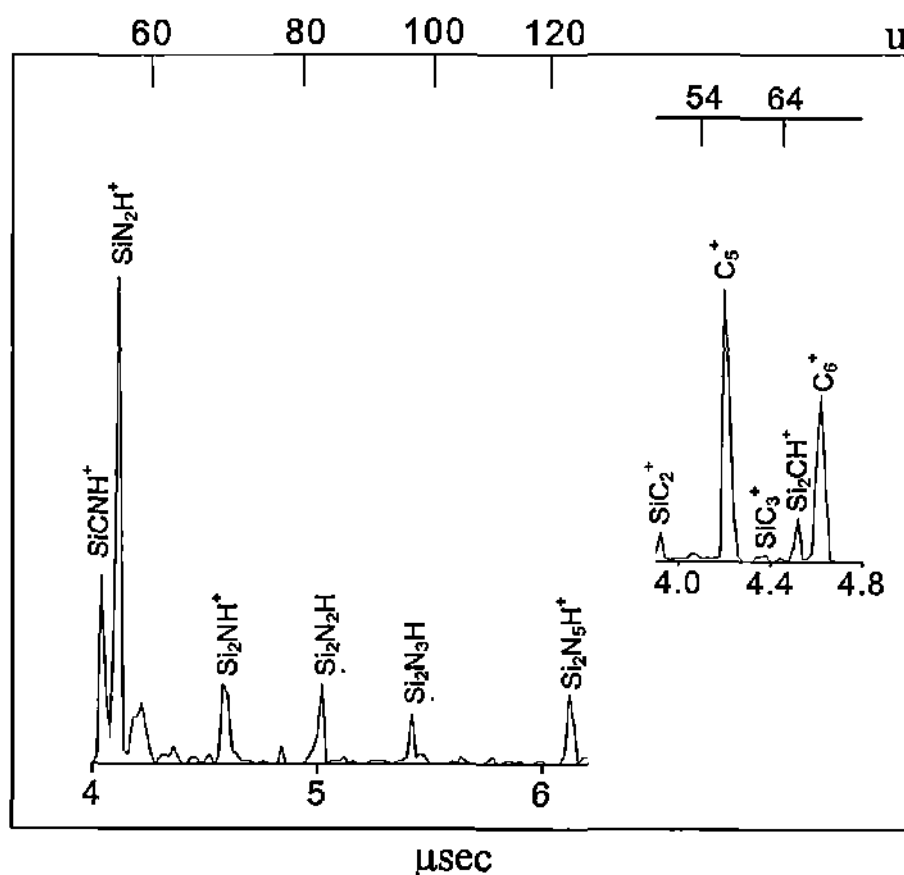

Fig. 6.7 Time-of-flight mass spectra of the cluster species obtained by the laser ablation of SiO_2 in the presence of carbon and N_2-He mixture.

trend was observed with NH_3 as well. It is interesting to note that in the absence of N_2 or NH_3 in He, carbidic species are observed in both cases, though with very small intensities. Laser ablation of SiC has been reported to produce $Si_nC_m^+$ clusters (n = 1-3 and m = 1-2) [20].

It is well known that Si-C bonds are strong (Si-C = 250-335 kJ/mol) and are readily formed in bulk phase to produce the hard material. Thus, carbon is able to

react effectively at such high temperatures, as shown by the prominent carbidic species of silicon and germanium. Carrying out the reactive ablation of SiO_2 with N_2, in the presence of carbon does not enhance its reactivity. With NH_3, the reactivity of SiO_2 gets completely suppressed. A similar behavior is observed with B_2O_3 (see above). In the case of the ablation of GeO_2 in the presence of N_2 and NH_3, the transient CN and ON species react with GeO fragment to give rise to $GeCN^+$ and $GeON^+$ species.

6.4 Conclusions

We have carried out laser ablation of the group 13 metal oxides, B_2O_3, Al_2O_3 and Ga_2O_3 and of the group 14 metal oxides, SiO_2 and GeO_2, in nitrogen as well as ammonia atmospheres in a pulsed supersonic jet. The resulting product species have been mass analyzed using a time-of-flight mass spectrometer. Another set of reactive ablations have been performed after mixing the oxides with carbon. Table 1 lists all the product species obtained under the different reaction conditions. B_2O_3 produces nitridic species in nitrogen when mixed with carbon, otherwise only molecular adducts are seen. With ammonia, however, it has limited reactivity. In contrast, Al_2O_3 and Ga_2O_3 exhibit rich reactivity patterns giving rise to nitridic as well as oxynitridic species. Interestingly, Ga_2O_3 forms molecular adducts with NH_3, while in the presence of carbon, it produces GaN^+ both in nitrogen and ammonia atmosphere. In the case of the group 14 oxides, Si tends to cluster into dimeric species, which react with ammonia and nitrogen giving protonated nitridic species while GeO_2 produces oxynitridic species along with nitridic species. It is noteworthy that the presence of carbon in the reaction mixture is essential to the

158

formation of nitridic species of both boron and gallium, a situation much similar to the synthesis of their nanostructures [3,6].

Table 2 gives the essential summary of the work where only the most abundant species are denoted.

Thus, the observation of the formation of nitrides or oxynitrides in the vapor phase is illustrated by the following vapor-solid reaction mechanism
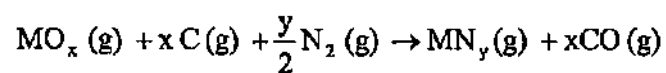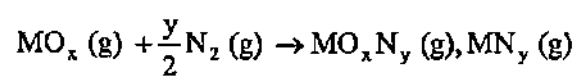
$$MO_x \, (g) + \frac{y}{2} N_2 \, (g) \rightarrow MO_x N_y \, (g), MN_y \, (g)$$

$$MO_x \, (g) + x \, C \, (g) + \frac{y}{2} N_2 \, (g) \rightarrow MN_y (g) + xCO \, (g)$$

Table 1.   Products formed during reactive ablation of the oxide powders [a]

Metal Oxides	N_2	$C + N_2$	NH_3	$C + NH_3$	C
B_2O_3	$\underline{(B_2O_3)N_2^+}$; $\underline{(B_2O_3)_2N_4^+}$	$\underline{BC^+}$, $\underline{(BC)_2^+}$, BN^+, BN_2^+, BN_3^+, $B_2N_4^+$	$\underline{B_3ON^+}$	—	$\underline{BC^+}$, $\underline{(BC)_2^+}$, $\underline{(BC)_3^+}$, $B_3C_4^+$, $B_5C_4^+$, $(BC)_6^+$
Al_2O_3	AlN_2^+, $\underline{AlON^+}$, $AlON_2^+$, $\underline{AlO_2N^+}$	AlC_2^+, $AlCN^+$, AlN_2^+, $\underline{AlON^+}$, Al_2NH^+, $AlON_2^+$	$\underline{AlON^+}$, $Al_2O_2N^+$	$\underline{AlON^+}$	—
Ga_2O_3	$\underline{GaN_2^+}$, $GaON_2^+$	$\underline{GaN^+}$, GaN_2^+	$\underline{Ga_1(NH_3)_nH^+}$ (n = 1-5) $\underline{Ga_2(NH_3)_nH^+}$ (n = 1-6)	$\underline{GaN^+}$	—
SiO_2	$\underline{Si_2N^+}$, Si_2NH^+, $Si_2N_2H^+$, $Si_2N_3H^+$, $Si_2N_4H^+$, $Si_2N_5H^+$	$\underline{SiN_2H^+}$, Si_2NH^+, $Si_2N_2H^+$, $Si_2N_3H^+$, $Si_2N_5H^+$	$\underline{Si_2N^+}$, Si_2NH^+, $Si_2N_2H^+$, $Si_2N_3H^+$, $Si_2N_4H^+$, $Si_2N_5H^+$	—	$\underline{SiC_2^+}$, SiC_3^+, $\underline{Si_2CH^+}$
GeO_2	$\underline{GeN^+}$, GeN_2^+; GeN_3^+, GeN_4^+	$GeON^+$, GeC_2N^+, $GeON_2^+$, $GeC_2N_2^+$, $(Ge)_2N_2^+$	$\underline{GeO_2N^+}$, $GeON_2^+$	$\underline{GeN^+}$, $\underline{GeC_2N^+}$, $GeON_2^+$	$\underline{GeC^+}$, GeC_2^+, GeC_3^+, $\underline{Ge_2C^+}$

[a] The most abundant species are underlined

Table 2   Most abundant species

Metal Oxides	N_2	NH_3	$C + N_2$
B_2O_3	BON	BON	BN
Al_2O_3	AlON	AlON	AlON
Ga_2O_3	GaN, GaON	Ga.NH$_3$	GaN
SiO_2	SiN	SiN	SiN
GeO_2	GeN	GeON	GeN,GeON

References

[1] M. Lu, A. Bonsetta and A. Bensaoula, *Appl. Phys. Lett.* 68, 622 (1996).

[2] S. J. Pearton, C. R. Abernathy, M. E. Overberg, G. T. Thaler, A. H. Onstine, B. P. Gila, F. Ren, B. Lou and J. Kim, *Materials Today* 24 (June 2002).

[3] F. L. Deepak, C. P. Vinod, K. Mukhopadhyay, A. Govindaraj and C. N. R. Rao, *Chem. Phys. Lett.* 353, 345 (2002).

[4] D. Golberg, Y. Bando, K. Karashima and T. Sato, *Chem. Phys. Lett.* 323, 185 (2000).

[5] Y. Zhang, J. Liu, R. He, Q. Zhang, X. Zhang and J. Zhu, *Chem. Mater.* 13, 3899 (2001).

[6] F. L. Deepak, A. Govindaraj and C. N. R. Rao, *J. Nanosci. and Nanotech.* 1, 303 (2001).

[7] W. Q. Han, S. S. Fan, Q. Q. Li and Y. D. Hu, *Science* 277, 1287 (1997).

[8] G. Gundiah, G. V. Madhav, A. Govindaraj, Md. Motin Seikh and C. N. R. Rao, *J. Mater. Chem.* 12, 1606 (2002).

[9] W. Han, S. Fan, Q. Li, B. Gu, X. Zhang and D. Yu, *Appl. Phys. Lett.* 71, 2271 (1997).

[10] D. E. Powers, S. G. Hansen, M. E. Geusic, A. C. Puiu, J. B. Hopkins, T. G. Deitz, M. A. Duncan, P. R. R. Langridge-Smith and R. E. Smalley, *J. Phys. Chem.* 86, 2556 (1982).

[11] L. Andrews, P. Hassanzadeh, T. R. Burkholder and J. M. L. Martin, *J. Chem. Phys.* 98, 922 (1993).

[12] L. Andrews, M. Zhou, G. V. Chertihin and W. D. Bare, *J. Phys. Chem. A* 104, 165 (2000).

[13] I. H. Lee and S. M. Park, *Bull. Korean Chem. Soc.* 21, 1065 (2000).

[14] S. J. Paukstis, J. L. Gole, D. A. Dixon and K. A. Peterson, *J. Phys. Chem. A* 106, 8435 (2002).

[15] J. M. L. Martin, P. R. Taylor, J. T. Yustein, T. R. Burkholder and L. Andrews, *J. Chem. Phys.* 99, 12 (1993).

[16] G. Leggieri, A. Luches, M. Martino, A. Perrone, R. Alexandrescu, A. Barborica, E. Gyorgy, I. N. Mihailescu, G. Majni and P. Mengucci, *Appl. Surf. Sci.* 96-98, 866 (1996).

[17] J. D. Lee 'Concise Inorganic Chemistry' Fifth edition, Chapman & Hill Ltd.: London (1996).

[18] M. Joseph, N. Sivakumar and P Manoravi, *Int. J. Mass Spectrom.* 176, 237 (1998).

[19] F. A. Cotton and G. Wilkinson, *'Advanced Inorganic Chemistry'* Wiley Eastern Limited : New Delhi (1993).

[20] T. Kimura, T. Nakamura, K. Ishikawa, F. Kokai and Y. Koga, *Chem. Phys. Lett.* 340, 296 (2001).

7. Preliminary investigations of the laser ablation of MoS_2 and MoS_3

SUMMARY

A preliminary study has been carried out on the products obtained by laser ablation of MoS_2 and MoS_3 by employing transmission electron microscopy. Laser ablation for MoS_2 was carried out in an atmosphere of jet-cooled helium as well as in a solvent medium. Inorganic fullerene-like structures of MoS_2 were obtained when the laser ablation of MoS_2 was carried out in a solvent medium such as CS_2. MoS_3 formed inorganic fullerene-like structures of MoS_2 when the ablation was performed in t-butyl disulphide medium. Laser ablation of other layered compounds such as WS_2 and h-BN has also been carried out in a solvent medium.

7.1 Introduction

Among several different physical and chemical methods available for the production of clusters or nanoparticles in gas-phase or in solution, the use of lasers to deposit nanocrystalline assembled films on substrates [1] or to ablate metal strips immersed in a solution having a capping agent [2] has drawn some attention, lately. The Laser plays a role in altering the size distribution of the clusters formed in the gas-phase as well as the sizes of the nanocrystalline sols. In the case of the gas-phase clusters, not only the laser fluence, but also the back-pressure of the carrier gas and the position, temperature and potential at which the substrate is kept, also play a vital role in the formation of the deposited nanocrystalline films. For the nanoparticles formed in solution, the laser power and the nature of the solvent medium are important. However, the mechanism of formation of nanoparticles by laser ablation in solution is yet to be well understood [3].

Graphite, which is a layered material, can form closed-cage structures such as fullerenes, nanotubes and onions on electron beam irradiation of graphite nanoparticles, has been known [4]. It was proposed that materials with quasi-two dimensional character have a large fraction of their atoms (in the plane perpendicular to the basal plane) with unsatisfied dangling bonds and thus are unstable in the planar structure. Hence, they form hollow-cage nanostructures that are devoid of dangling bonds [5]. Thus, it became of interest to find if other layered materials would also form similar closed-cage structures as graphite. Towards this end, several layered materials such as metal dichalcogenides (MX_2, $M = W$ or Mo and $X = S$ or Se) and hexagonal boron nitride (h-BN) have been investigated for the formation of nested inorganic fullerenes (IFs). Inorganic fullerenes of MoS_2 and

WS_2 find important application as solid lubricants, used to reduce the friction and wear of metal surfaces under heavy load.

Encapsulated polyhedral particles of boron nitride have been prepared by heating hexagonal-boron nitride in the presence of a metal catalyst such as tantalum in a nitrogen atmosphere [6]. Tenne and co-workers [7,8] prepared inorganic fullerenes of MoS_2 and WS_2 by heating thin metal films of Mo and W in an atmosphere of hydrogen sulphide. MoS_2 and WS_2 IFs have also been produced by heating the oxides of molybdenum (MoO_3) and tungsten (WO_3) in H_2S atmosphere [9]. Recently, encapsulated and hollow closed-cage structures of WS_2 and MoS_2 were prepared by laser ablation of the corresponding layered structures in an argon atmosphere in an electric furnace heated to different temperatures [10].

We have carried out a preliminary study of the laser ablation of MoS_2 in an atmosphere of pulsed jet-cooled helium as well as of MoS_2 and MoS_3 in a solvent medium supplying excess sulphur. Laser ablation of WS_2 and h-BN were also attempted in a solvent medium.

7.2 Experimental

MoS_2 and WS_2 were prepared by decomposing ammonium thiomolybdate and ammonium thiotungstate around 800 °C in flowing hydrogen [11]. Powder x-ray diffraction (XRD) patterns were recorded using a Siemens Seifert 3000 XRD, employing Cu $K\alpha$ radiation. The XRD of final product confirmed the formation of the hexagonal phase of MoS_2 and WS_2. Hexagonal-BN was commercially procured.

MoS_2 was mounted on a grooved rod as described in section 6.1 and placed in front of the mouth of the pulsed supersonic valve emitting short pulses (60-100 μs) of cooled helium. The gas-phase clusters, thus formed by the mixing of the

ablation products and jet-cooled helium, were deposited on glass substrates placed at ~3 cm from the ablation zone (before the skimmer) and at ~10 cm from the ablation zone (after the skimmer). The deposited films were examined by XRD to confirm the phase of the reactant material formed. A portion of the film was scraped and dispersed in methanol and sonicated for a minute. A drop of this suspension was placed on a holey carbon coated Cu grid and analyzed by Transmission electron microscopy (JEOL-3010 TEM), operating at 300 KV. Q-switched output of 532 nm of Nd-YAG laser was used for ablation with laser power varying in the range of 10-70 mJ/pulse.

For performing the laser ablation of MoS_2 in solution, MoS_2 powder was sonicated in the solvent in a 5 ml beaker. The solvents used were carbon disulphide (CS_2) and tert-butyl disulphide (TBS). The beaker, containing the powder and the solvent, was placed in the laser beam path (aperture ~ 5mm) such that the laser beam was scattered within the solution portion, inside the beaker (see schematic in Fig. 7.1).
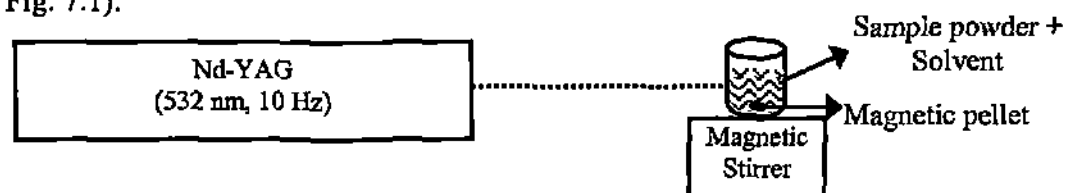

Fig. 7.1 A schematic of the set-up used for laser ablation in a solvent medium.

The solution was also continuously stirred using a magnetic stirrer to homogeneously expose the entire solution. The ablation was performed for a duration of about 30 minutes. The solvent was evaporated after the ablation and the ablation products were washed with methanol and a dispersion of the products in methanol was placed on the TEM grid for analysis. The same procedure was adopted for MoS_3 and WS_2 powders also.

Hexagonal-boron nitride was similarly laser ablated in a medium of aqueous ammonia. Another solvent medium consisting of liquor ammonia and dimethylamine was also used.

7.3 Results and discussion

Laser ablation under jet-cooled Helium

TEM images of MoS_2 nanoparticles obtained when MoS_2 is ablated using 532 nm Nd-YAG of ~ 70 mJ/pulse in an atmosphere of pulsed jet-cooled helium are shown in Fig. 7.2. The helium back-pressure was varied between 8 atms to 2 atms. Spherical nanoparticles were observed under TEM with size ranging from 20-110 nm in diameter when the ablation was carried out with helium back-pressure of 8 atmospheres (see Fig. 7.2a). Lower helium back-pressure (~2 atms) produced much smaller (10-25 nm) spherical nanoparticles (see Fig. 7.2b). Electron diffraction pattern obtained on the nanoparticles corresponded to the (103) (d= 2.27 Å) and (101) (d= 2.67 Å) plane of h-MoS_2. Thus, higher back-pressure of helium produces larger nanoparticles on account of higher cooling, as expected from the principle of supersonic expansion [12].
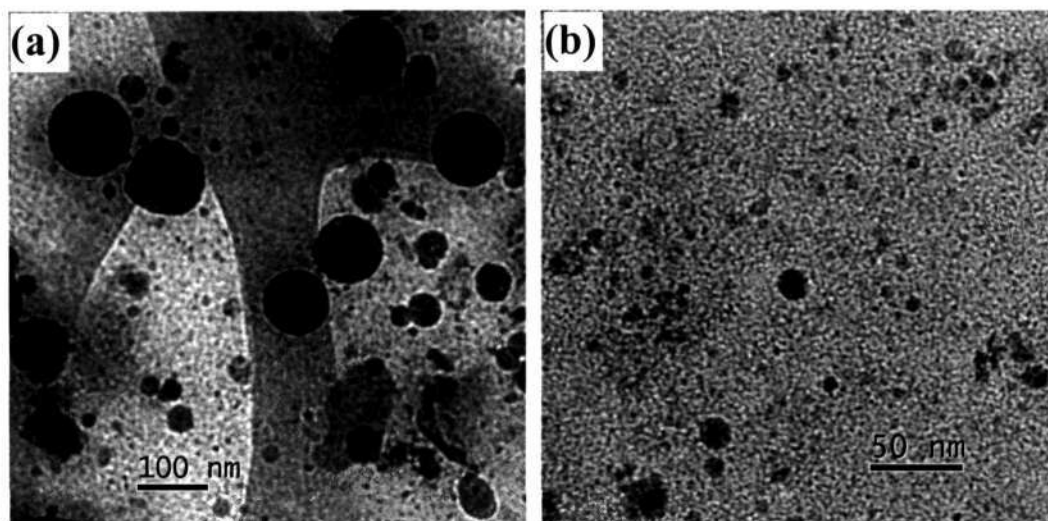

Fig. 7.2 TEM images of MoS_2 nanoparticles obtained with laser power of ~70 mJ/pulse and helium back-pressure of (a) 8 atms and (b) 2 atms.

We, then, studied the effect of the laser energy on the formation of the particles. High resolution TEM (HREM) images of nearly spherical MoS_2 nanoparticles obtained by laser ablation with a helium back-pressure of 2 atms using different laser power are shown in Fig. 7.3. At a low laser power of 12 mJ/pulse (see Fig. 7.3a), MoS_2 lattice fringes corresponding to (100) plane, spaced ~ 2.6 Å apart are seen inside the particle.
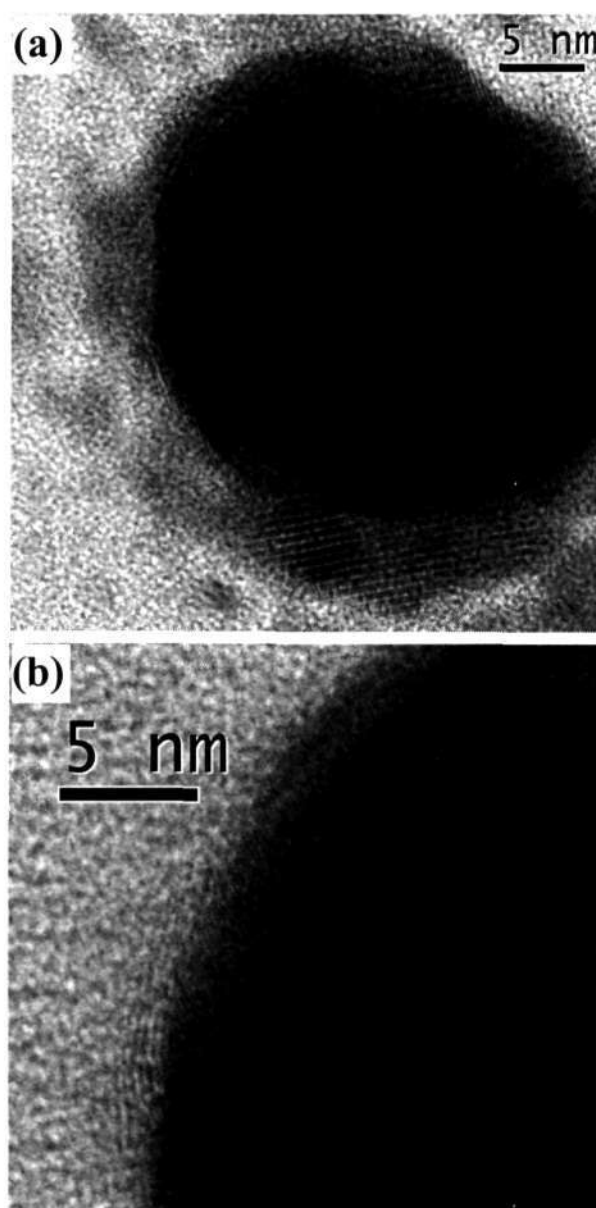

Fig. 7.3 HREM images of MoS_2 nanoparticles obtained using helium back pressure of 2 atms and laser power of (a) ~12 mJ/pulse and (b) ~70 mJ/pulse.

The image appears to have fringes at the periphery of the particle, suggesting a possible IF-structure. Thus, we observe lattice fringes with a spacing of 6.14 Å corresponding to (002) basal plane of MoS_2. On the other hand, with a higher laser power of ~70 mJ/pulse (helium back-pressure remaining the same), the MoS_2 nanoparticle tends to break as Mo and S as revealed by the HREM image in Fig. 7.3b. The inner portion of the nanoparticle reveals Mo lattice fringes spaced at ~ 2.1 Å corresponding to (110) plane of cubic-Mo while the circumference of the particles shows discontinuous lattice fringes of ~ 3.1 Å corresponding to (401) plane of orthorhombic-S.
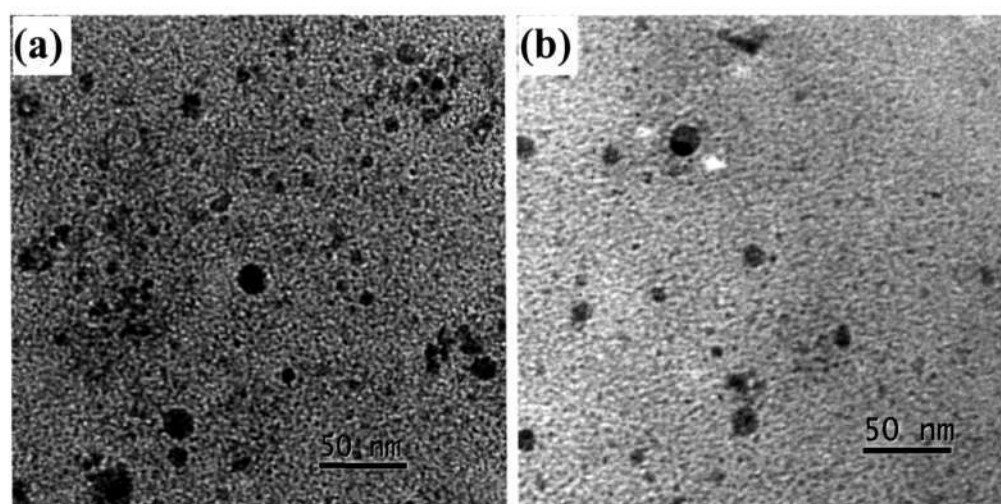

Fig. 7.4 TEM images of MoS_2 nanoparticles obtained using laser power of ~70 mJ/pulse and by keeping the substrate at different positions from the ablation zone (a) before the skimmer, ~3 cm and (b) after the skimmer, ~ 10 cm.

The placement of the substrate does not seem to influence the size distribution of the ablated products deposited. TEM images of MoS_2 nanoparticles obtained when the substrate was placed close to the sample cell (~ 3 cm, before the skimmer) and far from it (~ 10 cm, after the skimmer) are shown in Fig. 7.4a and b, respectively. There seems to be no effect on the size of the nanoparticles obtained in either case.

Laser ablation under solvent medium

Laser ablation of MoS_2 was carried out in a CS_2 medium where MoS_2 powder was dispersed. CS_2 was chosen since it provides easy liberation of sulphur on account of the covalent nature of the bonds in the molecule. Fig. 7.5 shows the TEM images of the MoS_2 nanoparticles obtained by carrying out laser ablation in CS_2 medium using different laser power settings. With a laser power of ~40mJ/pulse, quasi-spherical nanoparticle of MoS_2 of diameter ~ 35 nm are obtained as shown in Fig. 7.5a. The image reveals a few discontinuous concentric layers of MoS_2 around the inner core. As the laser power is increased to ~60 mJ/pulse, the number of concentric layers of MoS_2 in the image increases, with the interlayer spacing of 6.3 Å (see Fig. 7.5b). Such concentric layers seem to reduce with a further increase in the laser power (~ 70 mJ/pulse). From the above variation of the laser power, it seems that a power of ~ 60mJ/pulse is optimum for producing inorganic fullerene–like nanoparticles of MoS_2 by this method.

The solvent medium was changed to tert-butyl disulphide and the laser ablation was carried out at two different laser power settings. Fig. 7.6a and b show the TEM images of MoS_2 nanoparticles obtained at laser power of ~ 60 and 70 mJ/pulse, respectively. The size range of the particles increases to 20-80 nm from 10-40 nm with increase in laser power. The inset in Fig. 7.6a shows a HREM image of a quasi-spherical nanoparticle with two concentric layers of MoS_2 on its periphery.
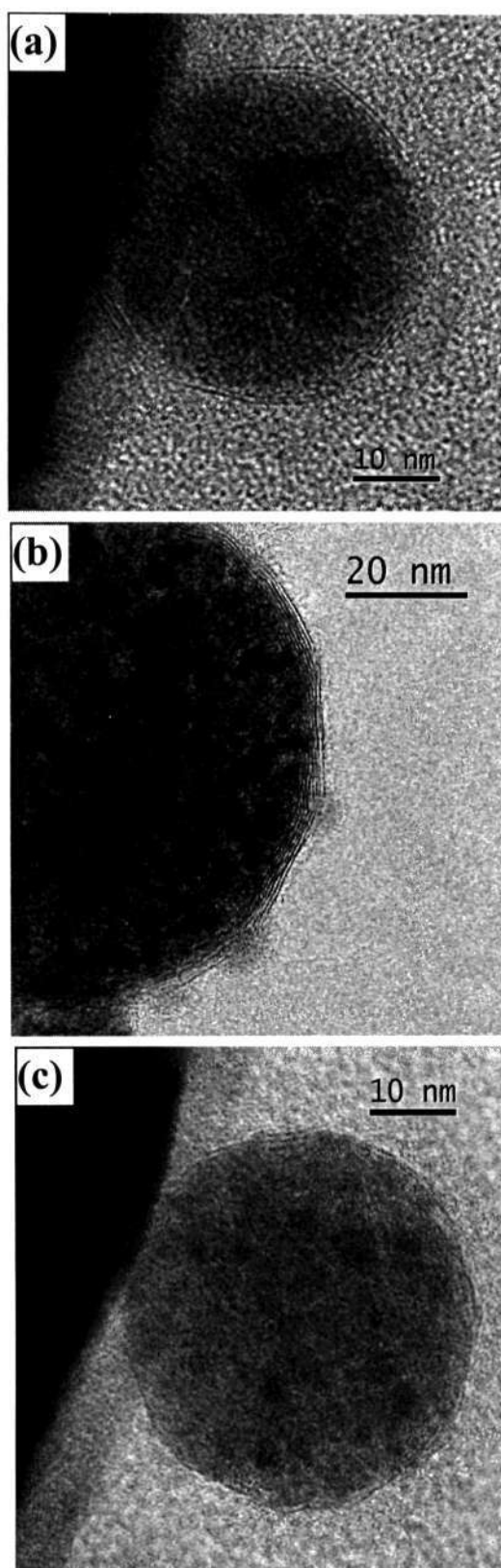
Fig. 7.5 HREM images of MoS₂ nanoparticles obtained laser ablation in CS₂ solvent using laser power of (a) ~40 mJ/pulse, (b) ~60 mJ/pulse and (c) ~70 mJ/pulse.
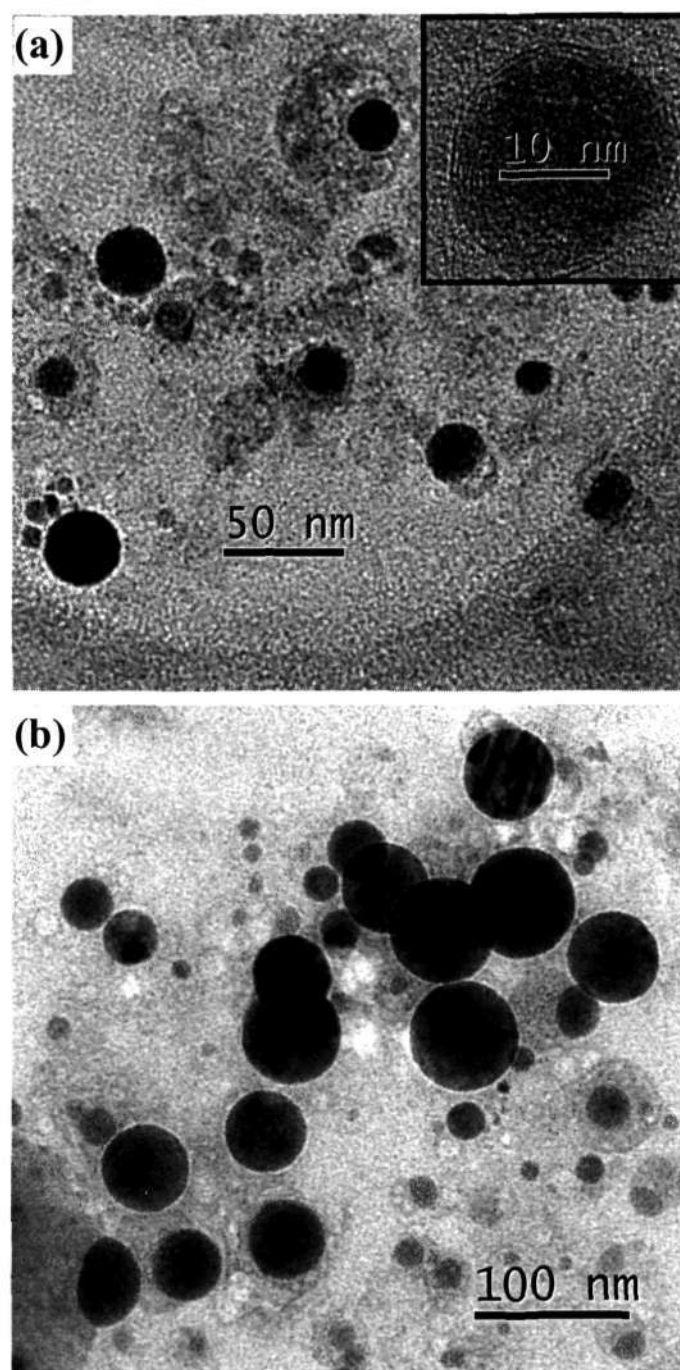
Fig. 7.6 TEM images of MoS_2 nanoparticles obtained by laser ablation of MoS_2 in tert-butyl disulphide solvent using laser power of (a) ~60 mJ/pulse and (b) ~70mJ/pulse. Inset in (a) shows HREM image of a nanoparticle.

We performed laser ablation of MoS_3, in solvent media of CS_2 and t-butyl disulphide at varying laser power settings. When MoS_3 was laser ablated in CS_2, we obtained nanoparticles with size range of 5-80 nm. Some nanoparticles revealed lattice fringes with spacing of ~ 2.8 Å corresponding to (100) plane of MoS_2. However, no concentric layers of MoS_2 were found. On the other hand, laser

174

ablation of MoS_3 in a medium of t-butyl disulphide gave many nanoparticles showing partial concentric layers of MoS_2 on the periphery of the particle, as shown in Fig. 7.7. Nanoparticles with diameter of ~30 nm showed concentric layers of MoS_2 with a spacing of 6.14 Å (see Fig. 7.7a) while those with larger diameters (60 nm) showed an expansion in the interlayer spacing (~ 6.32 Å) of the concentric layers surrounding the core of the nanoparticle (see Fig. 7.7b).
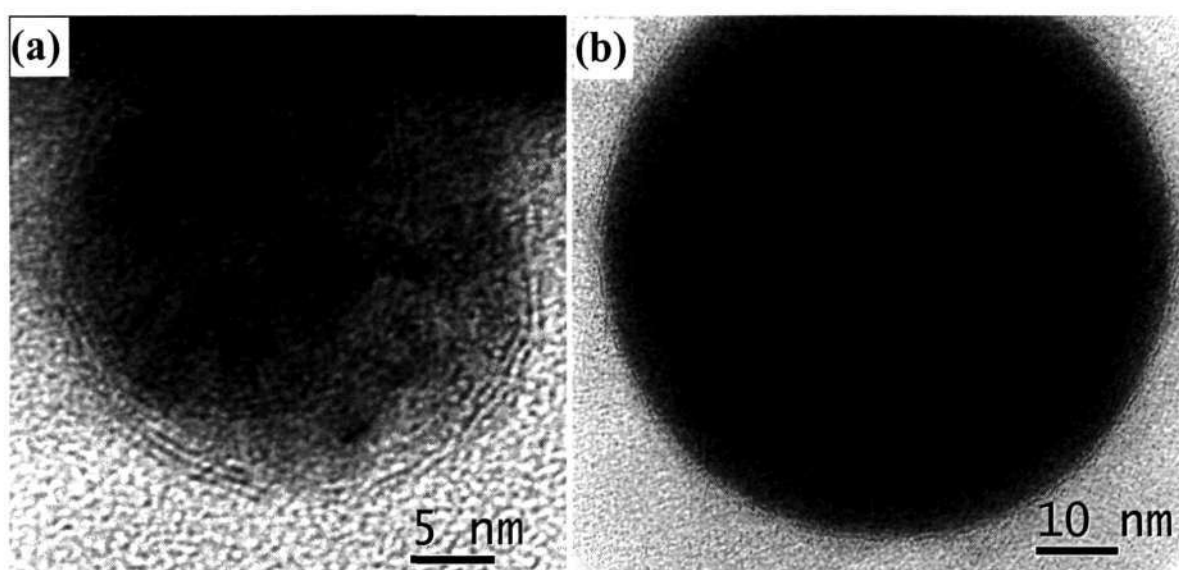

Fig. 7.7 Laser ablation of MoS_3 in t-butyl disulphide using laser power of ~60 mJ/pulse (a) nanoparticle of diameter ~ 26 nm (b) nanoparticle of diameter ~ 70 nm.

We carried out laser ablation of WS_2 in tert-butyl disulphide (TBS) medium using a laser power of ~60 mJ/pulse for 30 minutes. Subsequent to ablation, we evaporated TBS by heating for a couple of minutes to 200 °C. The nanoparticles were then dispersed in methanol by sonication and a drop placed on the TEM grid for analysis. We observed formation of a self-assembly of closely packed faceted particles of sizes around 10-20 nm (see Fig. 7.8a). A zoomed-up region of the assembly is shown in Fig. 7.8b, however no high-resolution image was obtained. The electron diffraction pattern of particles in Fig. 7.8b points that the particles are indeed WS_2.
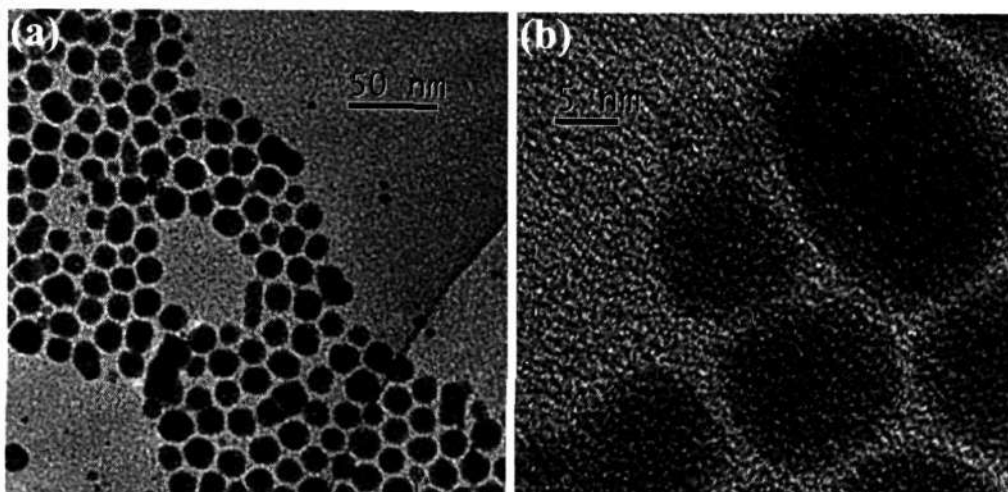
Fig. 7.8 TEM images of WS$_2$ nanoparticles obtained by laser ablation in tert-butyl disulphide solvent using laser power of ~60 mJ/pulse (a) self-assembly of closely packed faceted particles and (b) enlarged view of the same.

Figure 7.9 shows the TEM images of BN nanoparticles obtained when laser ablation of h-BN was carried out in liquour ammonia. Extremely small nanoparticles (3-5 nm) were obtained in the case of liquour ammonia being the solvent medium (Fig. 7.9a). The addition of dimethylamine to liquour ammonia helped in increasing the particle size to 7-10 nm (see Fig. 7.9b).
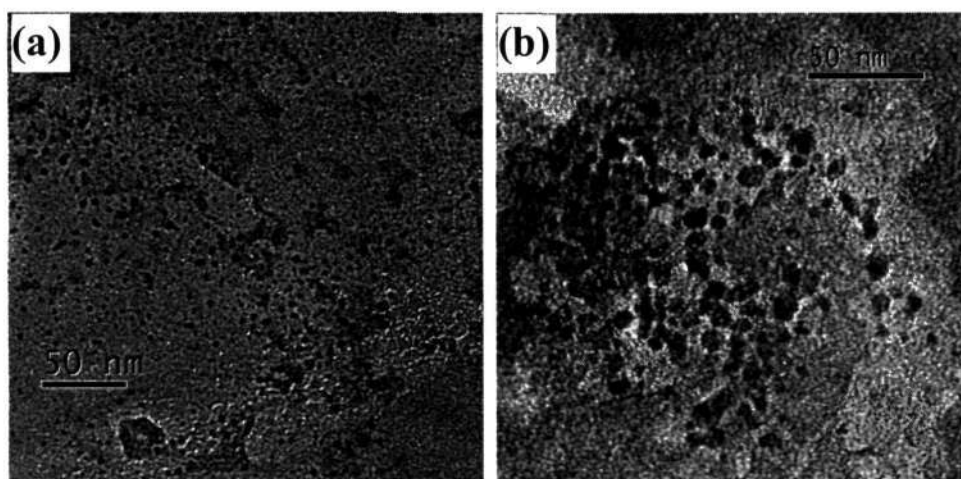

Fig. 7.9 TEM images of BN nanoparticles obtained by laser ablation using laser power of ~60 mJ/pulse in solvent medium of (a) liquour ammonia and (b) liquour ammonia + dimethylamine.

7.4 Conclusions

Laser ablation of MoS_2, MoS_3 and WS_2 has been investigated in an atmosphere of jet-cooled helium and in solvent media such as CS_2 and t-butyl disulphide. The present preliminary study has revealed that the formation of inorganic fullerene-like nanoparticles of MoS_2 and WS_2 is more likely in a solvent medium than in gas-phase, probably because of lower direct impact of the laser energy. A laser power of around 60 mJ/pulse (532 nm of Nd-YAG) appears to be optimal for the formation of fullerene structure showing concentric layers of MoS_2 around the core of the nanoparticle. MoS_3 also formed inorganic fullerene-like MoS_2 structures when the ablation was carried out in t-butyl disulphide medium. Laser ablation of h-BN in liquour ammonia yields nanoparticles and addition of dimethylamine increases the size of the nanoparticles.

References

[1] P. Milani, A. Podesta, P.Piseri, E. Barborini, C. Lenardi and C. Castelnovo, *Diamond and Related Materials* 10, 240 (2001).

[2] F. Mafuné, J-y. Kohno, Y. Takeda and T. Kondow, *J. Phys. Chem. B* 106, 7575 (2002).

[3] J. Zhang, J. Worley, S. Dénommée, C. Kingston, Z. J. Jakubek, Y. Deslandes, M. Post, B. Simard, N. Braidy and G. A. Botton, *J. Phys. Chem. B* 107, 6920 (2003).

[4] D. Ugarte, *Nature* 359, 707 (1992).

[5] R. Tenne, M. Homyonfer and Y. Feldman, *Chem. Mater.* 10, 3225 (1998).

[6] M. Terrones, W. K. Tsu, H. Terrones, J.P. Zhang, S. Ramos, J. P. Hare, R. Castillo, K. Prassides, A. K. Cheetam, H. W. Kroto and D. R. M. Walton, *Chem. Phys. Lett.* 259, 568 (1996).

[7] L. Margulis, G. Salitra, R. Tenne and M. Talianker, *Nature* 365, 113 (1993).

[8] R. Tenne, L. Margulis, M. Genut and G. Hodes, *Nature* 360, 444 (1992).

[9] Y. Feldman, E. Wasserman, D. J. Srolovitz and R. Tenne, *Science* 267, 222 (1995).

[10] R. Sen, A. Govindaraj, K. Suenaga, S. Suzuki, H. Kataura, S. Iijima and Y. Achiba, *Chem. Phys. Lett.* 340, 242 (2001).

[11] M. Nath, A. Govindaraj and C. N. R. Rao, *Adv. Mater.* 12, 283 (2000).

[12] U. Buck In 'Clusters of atoms and molecules I, Theory, Experiment, and Clusters of Atoms' Edited by H. Haberland, Springer-Verlag: Berlin, p. 209 (1994).

539.6
Po3